

A comparison of trace element concentrations in chromite from komatiites, picrites and layered intrusions: Implications for the formation of massive chromite layers.

Sarah-Jane Barnes*¹, Eduardo T Mansur^{1, 2} Wolfgang D Maier ³, Stephen A Prevec ⁴

¹Sciences de la Terre, Université du Québec à Chicoutimi, 555 boulevard de l’université, Québec G7H 2B1, Canada

²Geological Survey of Norway, P.O. Box 6315 Torgarden, NO-7491 Trondheim, Norway

³ School of Earth and Environmental Sciences, Cardiff University, Cardiff, United Kingdom

⁴ Department of Geology, Rhodes University, Makhanda, South Africa, 6140.

*Corresponding Author

Email for correspondence sjbarnes@uqac.ca

Keywords, Chromite, Trace elements, komatiite, picrite, Great Dyke, Stillwater, Bushveld,

Abstract :

By examining the minor and trace element contents of chromites from three intrusions; the Bushveld Complex (South Africa), the Stillwater Complex (USA) and the Great Dyke (Zimbabwe), and comparing these chromite compositions to those of magmas from which they could have formed (komatiites and picrites) we conclude that: a) the variations in Ti, V, Sc and Ga contents across stratigraphy and across individual layers do not support the model of magma mixing leading to chromite-only crystallization; b) the chromites from the lowest levels of the intrusions could have crystallized from komatiite liquids that were contaminated with continental crust; c) the Great Dyke chromites have the highest Cr# and lowest incompatible element contents and formed from a liquid closest to komatiite; d) all of the chromites, except those of the Dunite Succession of the Great Dyke have equilibrated with a liquid that had also crystallized pyroxene; e) the Great Dyke and Stillwater chromites show a narrower range in composition than the Bushveld chromites; f) Chromites from the western limb of the Bushveld Complex contain much higher V contents than all the other chromites. This requires either, that the fO_2 was lower in the western Bushveld or that the chromites equilibrated with a V-rich magma. We favor a model where chromite and silicate minerals crystallized in cotectic proportions (~2:98). The chromite, silicates and transporting liquid are emplaced into the magma chamber. During emplacement the chromite and silicate separated due to viscous particle flow to form a massive chromite layer overlain by silicates.

Introduction

The composition of chromite is of interest for both petrogenetic and economic reasons. On the petrogenetic side, chromite is one of first minerals to crystallize from primary magmas and one of the last to be consumed during partial melting of the mantle. Thus, variations in chromite compositions could potentially help inform us of the conditions during partial melting of the mantle and during crystallization of primary magmas. On the economic side, two important issues are worthy of consideration. First, the only economic source of Cr is chromite, either from massive chromite layers in ultramafic to mafic intrusions or as podiform chromites in ophiolites (Cawthorn et al. 2005; Mosier et al. 2012; Schulte et al. 2012). Most (> 70%) Cr is produced from mafic and ultramafic intrusions, principally the Bushveld Complex of South Africa, with minor production from the Great Dyke of Zimbabwe, the Kemi intrusion of Finland, and the Nuasahi and Sukinda intrusions of India (Fig. 1a). In terms of resources, however, the deposits are more evenly divided with the ophiolites (mainly Kempirsai, Kazakhstan) containing >40 % of the world's reserves (Fig. 1b). Another point of economic interest is that most of the chromite layers and podiform chromites are enriched in the platinum-group elements (PGE) Os, Ir, Ru, relative to the surrounding silicate rocks and some are also enriched in Rh, Pt and Pd (Barnes et al. 2016; Brough, et al. 2015; Mondal et al. 2019; Naldrett et al 2009; Scoon and Teigler 1994). Indeed, the world's largest PGE deposit is hosted in a massive chromite layer called the UG2 (Upper Group chromite layer 2) of the Bushveld Complex (McLaren and de Villiers 1982; Naldrett 2011). However, the PGE in massive chromites from layered intrusions are not found in the chromite (Pagé et al. 2012; Pagé et al. 2016)

The origin of the massive chromite layers in intrusions and podiform chromite in the ophiolites is not clear. A fundamental question is how a rock consisting of >50% chromite can be

formed from a mafic magma, because during crystallization the cotectic proportion of chromite to silicate minerals is approximately 1 to 2 % (Roeder et al. 2006). This leads to two problems: a) how can 1 to 2% chromite be concentrated to form a massive chromite layer? And 2) assuming equilibrium processes, at least 1000 times more magma than chromite is required. Furthermore, following chromite crystallization this magma should be Cr depleted and yet at the Bushveld Complex mass balance calculations show that insufficient Cr-depleted material is present (Cawthorn and Walraven 1998; Eales 2000). Campbell and Murck (1993) point out the same problem at the Stillwater Complex, however there and at the Great Dyke, parts of the upper portions of the complexes have been eroded and therefore it is not possible to say that there is insufficient Cr-depleted material present in these cases.

A number of models have been proposed. We can consider these in terms of their ability to saturate the magma in chromite by changing the intensive variables of temperature, pressure, oxygen fugacity (fO_2), and composition of the magma or in terms of physical processes.

1) Initially it was thought that as temperature dropped, olivine crystallized, resulting in the composition of the magma becoming more oxidized and iron-rich. The magma then would crystallize both olivine or pyroxene and chromite in cotectic proportions. The chromite then settled through the liquid and accumulated on the cumulate pile (Wagner 1923). This model is currently out of favor, because the chromite grains are generally quite small (0.05 to 0.2 mm) and therefore it is thought would not settle in spite of the large density contrast between silicate magma and oxide. However, Manoochchri and Schmidt (2014) demonstrated using centrifuge experiments that chromite does settle. Furthermore, recently a variation of the chromite settling model has been suggested in which chromite grains might form clusters by syneusis. Such clusters would then be large enough to settle (Vukmanovic, pers. com.).

- 2) Liu and Presnall (1990) showed that in the Mg-Ca-Al system spinel is less soluble at high pressure. This has led to models whereby a large increase in the amount of chromite crystallizing is brought about by a sudden increase in pressure in the magma chamber (Cawthorn 2005; Lipin 1993). However, Roeder and Reynolds (1991) found that chromite is, in fact, slightly more soluble at high pressure. Latypov et al. (2017, 2022) proposed that a rapid transfer of a superheated magma from depth would lower pressure in the magma and could bring chromite only onto the liquidus which they modelled using the MELTS program.
- 3) An increase in fO_2 would ensure that most of the Cr is converted to Cr^{3+} (the form of Cr in chromite) leading to chromite saturation (Ulmer 1969; Murck and Campbell 1986; Roeder and Reynolds 1991).
- 4) The dominant model for the past 40 years has been a sudden compositional change brought about by magma mixing – a model (based on Fe-free experiments; Irvine, 1977) whereby primitive magma mixed with fractionated resident magma temporarily leads to chromite-only crystallization. However, recent experimental work which included Fe shows that magma mixing will not bring about chromite-only saturation (Keltie 2018).
- 5) Based on silicate inclusions in chromite some authors have suggested that addition of SiO_2 from a partial melt of SiO_2 rich country rocks (in particular in the roof of intrusions) could lead to chromite-only saturation (Irvine 1975; Alapieti et al. 1989; Kinnaird et al. 2002; Spandler et al. 2005). However, this process requires so much SiO_2 to be added to the magma that olivine would not be on the liquidus, which is inconsistent with the presence of olivine in the chromite layers from the Stillwater Complex and the Great Dyke (Irvine, 1977) and in some of the Bushveld chromite layers (Gain 1985).

6) Veksler and Hou (2020) found that by adding 2 to 4% H₂O to a magma of a composition similar to the proposed composition of the Bushveld B1 magma (Barnes et al. 2010) would lead to a 250 °C interval of chromite-only crystallization. However, the addition of H₂O suppresses plagioclase crystallization, which is inconsistent with the presence of large amounts of plagioclase in the chromite layers of the Upper Critical Zone of the Bushveld. Furthermore, the chromite compositions found in the experiments are too rich in Fe compared with those of observed Bushveld chromite.

7) Leshner et al. (2019) proposed that partial melting of banded iron formation and release of magnetite to a komatiite magma could result in the magnetite being converted to chromite that then formed the chromite layers. Experimental work by Keltie (2018) found that magnetite dissolves in komatiite magma, thus raising the Fe content of the magma which leads to chromite saturation at lower Cr contents. If sufficient Fe is added, then chromite-only crystallization does occur.

Some models, particularly those looking at the formation of chromite in ophiolites, propose a compositional change brought about by reaction between preexisting silicate minerals and a new melt.

1) For podiform chromites it is proposed that orthopyroxene in harzburgites reacted with Si-undersaturated melt derived from deeper in the mantle to form olivine plus chromite (Arai 1997; González-Jiménez 2014).

2) Variations on this model have been proposed for chromite in layered intrusions, whereby picritic melts percolated down into the cumulate pile and reacted with the cumulate minerals to form thin chromite layers (O'Driscoll et al. 2009). Alternatively, fluids rising through the

cumulate pile could react with norite to dissolve orthopyroxene, releasing Cr and leaving an anorthositic residuum (Marsh et al. 2021). The Cr-rich liquid precipitated chromite at a level in the intrusions where conditions changed such that the Cr-rich liquid became saturated in only chromite (Nicholson and Mathez 1991; Marsh et al. 2021).

Some models suggest the chromite is collected by physical processes.

- 1) Density currents could transport chromite from the upper parts of the chamber to the top of the cumulate pile (Irvine 1979, 1980), but this still leaves the mass balance problem unresolved.
- 2) To circumvent the mass balance problem, so called “offstage” models have been proposed, whereby chromite and silicate minerals crystallized in cotectic proportions to form a slurry of chromite, silicates and liquid. This slurry was then injected into the magma chamber (Eales 2000; Jenkins and Mungall 2018; Mondal and Mathez 2007; Voordouw et al. 2013) or slumped from the walls into the magma chamber (Forien et al. 2015; Maier et al. 2013; Naldrett et al. 2012; Wilson and Prendergast 1989) and during transport the chromite and silicates were separated from each other by winnowing. The Cr-depleted liquid is thought to have slumped into the center of the intrusion (Forien et al. 2015; Maier et al. 2013) or have been forced up along the sides of the intrusion (Naldrett et al. 2012).

Previous studies of the major and minor element composition of chromite (Barnes and Roeder 2001; Kamenetsky et al. 2001) were constrained by two factors. First, the concentrations of only a few elements (Ti, Al, Cr, Fe and Mg) could be reliably determined due to the limitations of microprobe analysis. Secondly, chromite is generally an accessory mineral present at <2 modal %, and is consequently susceptible to post-crystallization re-equilibration with the

other phases present. This is particularly true for the 2+ ions (Barnes 1998; Roeder and Campbell 1985), such that the original composition of the chromite can be difficult to estimate.

The advent of laser-ablation inductively-coupled plasma mass spectrometry (LA-ICP-MS) provides the opportunity to quantify a wider range of elements down to the ppm and even ppb level for many minerals, including chromite. Consequently, there are now numerous studies of the compositions of chromite found in rocks representative of the mantle, conducted with the goal of understanding processes in the mantle (Gonzalez-Jimenez et al. 2014; Pagé and Barnes 2009; Zhou et al. 2014). Other uses include the application of V content of chromite from komatiites, to document the oxygen fugacity of the early Earth (Canil 2002; Nicklas et al. 2016). The PGE contents of chromites from volcanic rocks have been determined to investigate the use of PGE concentrations in chromite in exploration for Ni and PGE deposits (Arguin et al. 2016; Locemellis et al. 2011; Pagé et al. 2012; Pagé and Barnes 2016; Park et al. 2012, 2017). However, the trace element content of chromite from layered intrusions has not received much attention.

There are three large layered intrusions that contain PGE deposits; the Rustenburg Layered Suite of the Bushveld Complex (South Africa), the Stillwater Complex (Montana, USA) and the Great Dyke (Zimbabwe). All contain numerous massive chromite layers. This work will present results for the chromite compositions from these intrusions and compare the results with compositions of chromite from the Alexo komatiite (Ontario, Canada) and picrites from the Emeishan large igneous province (China), with the aims of determining: a) the type of magma from which the chromite crystallized and b) the process(es) whereby they formed.

Materials and Methods.

Terminology.

In many publications the term chromitite is used to refer to rocks with a high percentage of chromite. However, the use of the term is inconsistent, varying from rocks with >90% chromite to rocks with 30% chromite. In order to avoid confusion the term will not be used here. The terms massive chromite will be applied to rocks containing >66% chromite (the volume at which chromite grains in a rock should be in contact), semi-massive chromite for rocks containing 33% to 66% chromite (some chromite grains will be contact and but some silicate grains will be in contact), disseminated chromite for rocks containing 2 to 33%.

Materials

Stillwater Complex

The Stillwater Complex, Montana, U.S.A. (Fig. 2a) is a layered intrusion that was emplaced into the Archean Wyoming Craton over a three million year period, 2709 to 2012 Ma. (Wall et al. 2018). The host rocks consist of a meta-sedimentary sequence, which was intruded by a granitoid suite between 2730 and 2790 Ma (Wooden 1991). The complex has been divided into 5 series; the Basal, the Ultramafic, the Lower Banded, Middle Banded and Upper Banded (McCallum et al. 1980).

The lower part of the Ultramafic series, known as the Peridotite zone, consists of a series of cyclic units of harzburgites overlain by olivine orthopyroxenites and orthopyroxenites (Cooper 1997; Jackson 1961). Within the peridotites, zones consisting of layers of semi-massive to massive chromite are present. The chromite zones are labelled A to K from the base upwards (Fig. 2b). In most cases, each chromite zone contains a number of chromite-rich layers separated by chromite-bearing peridotite or pyroxenite (Fig. 3a). In many cases, but not all, the silicate

rocks associated with the chromite layers have a pegmatoidal texture. The zones vary in thickness from thin doublets of the E zone (5 to 10 cm, Fig. 3a) to the thick (4 m) G zone (Page 1971). The thickness of individual layers of chromite varies from 1 cm to 50 cm, with the basal layers of the G and H chromite zones (Fig. 3b) being the thickest (~30 to 50 cm, Page 1971) and the layers of the C, E, I and J chromite zones being amongst the thinnest (1-3cm). The upper part of the Ultramafic series consists of orthopyroxenite, which contains ~0.5 modal % chromite (Barnes et al. 2016), and is called the Bronzitite zone. McCallum (2002) reports that the zone is uniform except for a few thin layers of olivine +/- chromite. All of the zones, A to K were sampled along two traverses across the Mountain View and Benbow areas (Fig. 2a). In addition a rare example of massive chromite from the olivine-bearing zone 1 (OB1), just below the level of the PGE deposit (the JM reef) was provided by Dr. Zientek.

Most of the layers are massive in these two areas. Exceptions to this are layers C and E which are semi-massive (30 to 50 modal % chromite). In the semi-massive layers, where most of the chromite grains do not quite touch, the grains are euhedral and small (0.2-0.5 mm). In contrast, in the massive layers many of the chromite grains are larger (1-2 mm), anhedral, and have 120° triple junctions, suggesting that they grew post-cumulus (Fig. 3c). The interstitial minerals in most of the chromite layers are subhedral olivine and oikocrysts of orthopyroxene (Fig. 3d). Exceptions to this are the E and J chromite layers where the interstitial mineral is predominantly subhedral orthopyroxene (Fig. 3e). The igneous assemblage has been preserved in most of our samples, but some samples contain serpentine, chlorite, actinolite and epidote as a result of greenschist facies metamorphism at 1700 Ma (Page 1977).

The Bushveld Complex

216 The Rustenburg Layered Suite (RLS) of the Bushveld Complex (South Africa) (Fig 4)
217 was emplaced into the Archean Kaapvaal Craton over a 5 million year period, 2055-2060 Ma,
218 (Scoates et al. 2021). It is the world's largest known layered intrusion (400 km by 300 km in
219 area, and approximately 8 to 9 km thick; Eales and Cawthorn, 1996). The RLS is divided into
220 five zones (Hall, 1932): the basal Marginal Zone (0-800 m of norites), overlain by the Lower
221 Zone (800-1300 m of cyclic units of harzburgites and pyroxenites), the Critical Zone (1000 to
222 1800 m of cyclic units of chromite, pyroxenites, and norites), the Main Zone (3000 to 3400 m of
223 norites, gabbronorites and anorthosites), and the Upper Zone (2000 to 2800 m of magnetitites,
224 ferrogabbronorites anorthosites, and diorites) (Fig. 4).

225 Twelve to 14 chromite layers are found in the Critical Zone. (As in the case of the Stillwater
226 Complex these layers are more correctly referred to as zones because in many cases each "layer"
227 consists of more than one massive chromite layer, but to be consistent with published literature the
228 term layers will be used, with the understanding that more than one massive chromite layer can be
229 present. In most areas the Lower Critical Zone consists of a series of cyclic units of chromite layers
230 and pyroxenites with minor harzburgites (Cameron 1980; Engelbrecht 1985; Scoon and Teigler
231 1994, Naldrett et al. 2012, Kaufmann 2018). The massive chromite layers in the Lower Critical
232 Zone are referred to as Lower Group (LG) 1 to 7, overlain by the Middle Group (MG) 0 to 2. The
233 base of the Upper Critical Zone is marked by the appearance of plagioclase as a cumulus phase in
234 an anorthosite layer just above the MG2 chromite. In most areas, the Upper Critical Zone contains
235 four to five layers of chromite, namely Middle Group (MG3 to 4) and Upper Group (UG) 1 to 3.
236 These layers occur within units consisting of chromite, pyroxenite and norite. Some cyclic units
237 contain anorthosites at the top of unit. Some 30 to 300 meters above the UG2 Reef (depending on
238 location) is the Merensky Reef (and cyclic unit). The base of the Merensky unit is typically marked

by a narrow 1-5 cm chromite layer. Normal Reef generally has two chromite layers, although as many as four and as few as one (or none) occur in some sections. The common rock type between the layers is coarse-grained melanorite usually described as “pegmatoidal feldspathic pyroxenite”.

In the northern limb (or lobe) the stratigraphy is more complicated (Grobler et al. 2019; Maier et al. 2021). The Lower Zone and Lower Critical Zone are largely absent. Rocks considered equivalent to the Upper Critical Zone, containing numerous xenoliths, are found at the lower contact. The first chromite layer in this zone is believed to be equivalent to the UG2. The Lower Zone is expressed as intrusions within the country rocks and, in contrast, to the western and eastern limbs chromite layers occur in the Lower Zone (Hulbert and von Gruenewaldt 1985).

For the current study, samples from the Marginal Zone sills as well as the LG6, MG1 and MG3, UG1 and UG2 chromites were analyzed by LA-ICP-MS. The MG1 and MG3 samples are from the Waterval Mine in the western Bushveld (Arunachellan 2022). The UG1 and UG2 samples are from the Impala Mine, (western Bushveld) previously studied for variations in whole rock compositions (Maier and Barnes 2008). In addition, Langa et al. (2021) analyzed chromite from two cross sections of UG2, one from the northern limb and one from the western limb from the Waterval Mine. The samples from the western limb will be referred to as UG2-W and those from the north as UG2-N in the following text. Samples from the other layers were not available at the time of this study and so the data set is supplemented for the layers LG1 to 5, MG2 and MG4 by the microprobe data of Naldrett et al. (2012).

As in the case of the Stillwater chromite, crystals from the semi-massive chromites are fine grained (0.1 to 0.5 mm) and euhedral, whereas in the massive chromite the chromite grains are coarser (0.5 to 1 mm) and show triple junctions. The chromites from the massive chromites contain small (4 X 40 μm) ilmenite exsolutions. In the Lower Critical Zone the most common interstitial

mineral is orthopyroxene. Small amounts of interstitial plagioclase and clinopyroxene are also present. The orthopyroxene can take the form of oikocrysts enclosing the chromite grains or occurs as euhedral laths. In our sample set of the Upper Group chromites the dominant mineral is interstitial plagioclase with minor orthopyroxene. Both minerals commonly take the form of oikocrysts (Figs. 5a and b).

The Great Dyke

The Great Dyke of Zimbabwe is a 550 km-long layered intrusion (Fig. 6) of early Proterozoic age (2575.4 ± 0.7 Ma, Oberthür 2002; Oberthür 2011) emplaced into the granite-greenstone terrain of the Zimbabwean Craton (Worst, 1960). The stratigraphy as defined by Wilson and Prendergast (1989) consists of a lower 2 km of the intrusion made up of ultramafic rocks (the Ultramafic Sequence), and an upper 1.5 km of mafic rocks (the Mafic Sequence) (Fig. 6). In the thickest part of the intrusion, the Ultramafic Sequence is divided into 14 cyclic units. The lower part of the Ultramafic Sequence (the Dunite Succession) comprises a series of cyclic units consisting of massive chromite layers overlain by dunite. The upper part of the Ultramafic Sequence (the Pyroxenite or Bronzite Succession) consists of cyclic units of massive chromite layers overlain by harzburgites, which in turn is overlain by orthopyroxenite. Not all units contain a chromite layer. The chromite layers are labeled from the top of the Ultramafic Sequence downwards from C1 to C12, where the numeral refers to the number of the cyclic unit in which the chromite is present. Towards the top of the very last orthopyroxenites of the Ultramafic Sequence is a 1 to 2 m-thick zone of PGE enrichment, known as the Main Sulfide Zone. Chromite layers 12 to 5 are thin (<20 cm) and contain very little (<5%) interstitial material (Wilson 1982). Chromite layers 4 to 1 are thicker (1 to 2 m), but contain more (20%) interstitial

material (Wilson 1982). Chromite grains in the chromite layers are 0.5 to 3 mm in size and polyhedral, with triple junctions. The interstitial material in the Dunite Succession is olivine or serpentine after olivine, whereas in the Bronzite Succession the interstitial silicates are orthopyroxene and olivine. Only samples from layers C8, C6 and C1d were available for the current LA-ICP-MS study. These data are supplemented with major and minor element compositions from Wilson (1982) and Mason Apps (1998). Disseminated chromite is present in the MSZ, and major and minor element data are available from Chaumba and Musa (2020), but were not included in the current study.

Chromite from komatiites and picrites.

In order to assess the composition of chromite crystallized from magma types that could be important in forming the layered intrusions, the composition of chromite grains from the Alexo komatiites of the Abitibi Greenstone Belt, Canada (Barnes et al. 1983; Houlié, et al. 2012; Meric 2018) and picrites of the Emeishan large igneous province, China (Arguin et al. 2016; Barnes et al. 2022) are considered.

The samples from the Alexo komatiites are from a thin olivine spinifex-textured flow and from a thick clinopyroxene spinifex-textured flow (Barnes et al. 1983). These correspond to categories 1 and 4, of Barnes (1998), representing a thin differentiated flow and layered lava-lake, respectively. The distinction may be important because the chromite from a thin flow would have less time to re-equilibrate with trapped liquid. Fine (<0.2 mm) euhedral disseminated (<1% modal) chromite grains are present interstitially to the olivine and to the acicular pyroxene in devitrified glass. Also present in the spinifex-textured part of the flow are skeletal chromite. However, only the euhedral chromite was analyzed. The Alexo locality was chosen because the

308 degree of metamorphism is low (prehnite-pumpellyite facies, Jolly 1982) and thus changes in
309 composition due to metamorphism are, probably, limited (Barnes 1998).

310 Detailed descriptions and analyses of chromite from the Emeishan large igneous province
311 have been presented previously (Arguin et al. 2016; Barnes et al. 2022). Most authors suggest
312 that two distinct magma series are present, high-Ti and low-Ti (Xu et al. 2001). However,
313 Kamenetsky et al. (2012) propose that rather than two distinct series, there is a continual
314 gradation from low to high-Ti magmas, The picrite samples from the current study do form two
315 distinct groups - one (high-Ti) enriched in Ti, Hf, Nb, Sn and LREE relative to one (low-Ti)
316 depleted in these elements, but enriched in Al (Barnes et al. 2022). Therefore the terms high-Ti
317 and low-Ti picrite will be used in this work. Picrites from both magma series contain
318 disseminated chromite grains (0.1 to 0.2 mm in size). The grains occur in two habits, as
319 inclusions in olivine (inclusion chromite) and as interstitial grains in a fine grained matrix of
320 clinopyroxene, plagioclase and magnetite (matrix chromite). The inclusion chromites are
321 euhedral and compositionally unzoned (Fig. 2 of Barnes et al. 2022). The matrix chromites have
322 an overgrowth of titano-magnetite surrounding the chromite core (Fig. 3 of Barnes et al. 2022).
323 Barnes et al. (2022) found that the chromite compositions reflect the composition of the magma
324 series, with chromite from high-Ti picrites being enriched in Ti, V, Nb, Sn, Hf and Ta and
325 depleted in Al relative to chromite from low-Ti picrites.

326

327 **Methods**

328 Polished thin sections of each sample were made and then examined with a petrographic
329 microscope. Chromite grains were selected based on their appearance. Euhedral grains which
330 lack fractures were favored. Five to 10 grains from each sample were analyzed. Major elements,

Mg, Al, Fe, Cr and minor elements Si, Ti, Mn and Ni were determined on a CAMECA SX100 microprobe by wavelength dispersive spectrometry (beam size 5 μm , accelerating voltage 15 Kv, and current 20 nA) at the Université Laval, Québec City. The concentration of minor and trace elements were determined by LA-ICP-MS at LabMaTer Université du Québec à Chicoutimi using an Excimer 193 nm resolution M-50 laser ablation system (Australian Scientific Instrument) equipped with a double volume cell S-155 (Laurin Technic) and coupled with an Agilent 7900 mass spectrometer. The LA-ICP-MS tuning parameters were a laser frequency of 15 Hz, a power of 3 mJ/pulse, a dwell time of 7.5 ms, and a fluence of 5 J/cm². The beam size was 55 or 44 μm depending on the size of the grain. For the komatiite-hosted chromite grains (because of their small size), spots in the center of the grains were used, but for the other chromites, line scans from time to rim across the surface of grains were made with a raster speed of 5 to 10 $\mu\text{m/s}$, depending on grain size. In order to avoid edge effects and possible alteration at the rims only the central part of the spectra was used for the line scans. The gas blank was measured for 30 s before switching on the laser for around 60 s. The ablated material was carried into the ICP-MS by an Ar–He gas mix at a rate of 0.8–1 L/min for Ar and 350 mL/min for He, and 2mL/min of nitrogen was also added to the mixture. Data reduction was carried out using the Iolite package for Igor Pro software (Paton et al. 2011). Maps of the element distribution were made of some chromite grains using the same parameters. The maps were generated using the Iolite package, based on the time-resolved composition of each element.

The isotopes ²⁹Si, ³¹P, ³⁴S, ⁴⁴Ca, ⁷⁵As, ¹²¹Sb, ¹²⁵Te, and ²⁰⁹Bi were monitored in order to exclude inclusions of; silicate, apatite and platinum-group element minerals. Inclusions were rare and excluded from the analyses. The isotopes ²⁴Mg, ²⁷Al, ⁴⁵Sc, ⁴⁹Ti, ⁵¹V, ⁵²Cr, ⁵⁵Mn, ⁵⁷Fe, ⁵⁹Co, ⁶⁰Ni, ⁶³Cu, ⁶⁶Zn, ⁷¹Ga, ⁸⁹Y, ⁹³Nb, ⁹⁵Mo, ¹⁰¹Ru, ¹⁰³Rh, ¹⁰⁸Pd, ¹¹¹Cd, ¹¹⁵In, ¹¹⁸Sn, ¹⁷⁸Hf, ¹⁸¹Ta, ¹⁸⁵Re,

354 ^{189}Os , ^{193}Ir , ^{195}Pt , and ^{197}Au were used to determine the concentrations of these elements.
355 possibility of interference of $^{53}\text{Cr}^{40}\text{Ar}$ on ^{93}Nb was investigated. However, there appears to be no
356 correlation between Cr and Nb; for example Nb concentrations in the in-house reference
357 chromite AX37 and MIA (which contain the highest observed Cr concentrations) are amongst
358 the lowest Nb concentrations at 0.015 ppm, close to detection limit. Therefore, the Cr
359 interference on Nb was considered negligible. The concentrations of Sn are too low for ^{115}Sn to
360 produce a significant interference on ^{115}In and thus was not considered. Cadmium, Cu and Ni
361 concentrations are too low to produce interferences on Pd, Rh and Ru and thus the potential
362 interference from these elements was not considered.

363 External calibration was carried out using two reference materials. GSE-1g (supplied by
364 USGS), with a composition close to a basaltic glass and doped with ~400 ppm of most trace
365 elements, was used for minor and trace elements, except the PGE, Au and S. Laflamme Po727
366 (supplied by Memorial University), a pyrrhotite (FeS) doped with ~40 ppm of each PGE and
367 Au, was used for the PGE and Au. ^{57}Fe was used for internal calibration. Natural chromite from
368 in-house reference materials, AX 37 (a komatiite) and GProbe 6 (a basaltic glass), were used as
369 monitors. The results obtained for the monitors agree within analytical error with the working
370 values (Supplementary Material, Table S1). Representative chromite analyses are presented in
371 Table 1. The full list of chromite analyses is provided in Supplementary Material, Table S2.

372 The results from the microprobe were used for Mg, Al, Si, Cr and Fe. The results from
373 the LA-ICP-MS were used for all other elements. Comparison of Ti and Mn from the two
374 methods are within 5 relative percent of each other.

375

376 Results

Platinum-Group Elements, Re and Au.

The concentrations of the Or, Ir, Ru and Rh for most of the analyzed chromites have been previously discussed in Arguin et al. (2016), Barnes et al. (2016), Meric (2018), Pagé et al. (2012) and Pagé and Barnes (2016). These authors found that Os, Ir, Ru and Rh, are present in chromite from volcanic rocks and in the marginal sills of the Bushveld at the 100 to 400 ppb level for Ru and at the 10 to 30 ppb level for Os, Ir and Rh. However, chromite from intrusions contain abundances below detection limits of Os, Ir, Ru and Rh (<10 to 20 ppb). Chromite from the intrusions contain small (1 to 20 μm) inclusions of laurites, which host the Os, Ir and Ru, and malanite, which hosts Rh (Barnes et al. 2016; Prichard et al. 2017). In the current study we also determined Pt, Pd, Au and Re concentrations and found that chromites from all settings contain less than detection levels of these elements (< 10 to 20 ppb). These observations are in agreement with other studies of PGE in chromite (Kamenetsky 2015; Locmelis et al. 2011, Park et al. 2012; 2017). The PGE, Au and Re will not be discussed any further in this work.

Major Elements

Chromium is the most abundant element in chromite and is rapidly depleted as the parent magma evolves, therefore for an overview the element concentrations are presented on plots of Cr_2O_3 versus the element or oxide. A more traditional approach would be to use Cr#, but this is affected by plagioclase crystallization and by oxidation state of the magma. Chromium concentrations vary from 35 to 60 weight % (Fig. 7). Chromites from komatiites and the Great Dyke show the highest Cr_2O_3 concentrations, from 52 to 59 weight %. In addition, the chromite from the LG1 to LG4 layers and from the sills of the Bushveld Complex fall in this range. Chromite from the Stillwater Complex, the Emeishan picrites and most of the remaining

400 Bushveld chromites show a lower range, from 40 to 50 weight % Cr_2O_3 . An exception to this is
401 chromite from the UG2-N of the Bushveld where Cr_2O_3 concentrations are lower, at 35 to 42
402 weight %.

403 Magnesium shows a positive correlation with Cr_2O_3 (Fig. 7a). Chromites from
404 komatiites, the Great Dyke and the Bushveld Complex form a single broad trend from 15 weight
405 % MgO for the Cr_2O_3 -rich chromite to 4 weight % MgO for the UG2-N. The Stillwater Complex
406 and Emeishan chromites appear to be more MgO-rich at a given Cr_2O_3 than the other chromites.
407 All Fe is plotted as FeOT, although some Fe is present as Fe_2O_3 . Because most of the Fe in
408 chromite occupies the same site as Mg, FeOT shows an inverse behavior to MgO with the Great
409 Dyke and komatiite samples having the lowest FeOT contents at 15 weight % and the UG2-N
410 chromites having the highest FeOT content at up to 40 weight %. The Stillwater Complex
411 chromites plot off the general trend, with lower FeOT at a given Cr_2O_3 content, consistent with
412 their slightly higher MgO contents.

413 Aluminum oxide shows an inverse correlation with Cr_2O_3 , which is to be expected as
414 both elements occupy the same trivalent crystallographic site in chromite. Most chromites fall on
415 a general trend from a low of 10 weight % Al_2O_3 in the komatiite and Great Dyke through to a
416 high of 20 weight % Al_2O_3 in the Stillwater chromites. Exceptions to this trend are chromites
417 from the UG2-N and the Emeishan high-Ti picrites which are depleted in Al_2O_3 relative to Cr_2O_3
418 (Fig. 7c).

419

420 **Minor Elements**

421 Titanium oxide shows an inverse correlation with Cr_2O_3 , but more than one trend is
422 evident (Fig. 8a). The chromites from the Great Dyke, komatiites, low-Ti picrites, the Bushveld

sills, LG1 to LG4 and the Stillwater Complex define one trend (I), with fairly low TiO_2 contents at 0.2 to 0.5 weight % and relatively little change in TiO_2 with Cr_2O_3 . The chromites from the Emeishan high-Ti picrites a second, steeper, trend (II) ranging from 1.5 to 2.5 weight % TiO_2 . The chromites of the Bushveld Complex from LG5 to UG2-W and the chromites from the UG2-N show trends parallel to the Emeishan high-Ti picrite chromites, but contain lower Cr_2O_3 concentrations.

As is the case for TiO_2 , V shows a negative correlation with Cr_2O_3 , but more than one trend is evident (Fig. 8b). The chromites from the Great Dyke, komatiites, Bushveld sills, LG1 to LG4, Stillwater, the Emeishan high-Ti picrites and UG2-N form one trend, starting at 800 ppm and rising to 2000 ppm in the UG2-N. The chromites of the Bushveld above the LG4 are richer in V than the other chromites and form a second trend, starting at 1500 ppm and rising to 3600 ppm. The chromite from Emeishan low- TiO_2 picrites form a separate cluster with low V contents of <1000 ppm.

Manganese shows a negative correlation with Cr_2O_3 , ranging from low values of ~1000 ppm in the komatiites to a high of 2500 ppm in the UG2-N (Fig. 8c). The Mn values from the Great Dyke cover a much wider range. Manganese concentrations of chromites from our study and that of Mason-Apps (1982) are low and similar to the komatiites. However, most of Wilson's (1982) MnO concentrations for chromite, shown inside the circle on figure 8c, are much higher.

Overall, Zn shows a negative correlation with Cr_2O_3 , with a low of 300 ppm in the Great Dyke chromites through to a high of 1600 ppm in the UG2-N (Fig. 7d). A few samples plot at much higher values than indicated by the overall trend.

Cobalt concentrations range from 200 to 350 ppm for most of the chromites and fall on a single but very broad trend showing a negative correlation with Cr (Fig. 8e). Exceptions to this are the chromites from the Bushveld sills and the chromite from the C1 unit of the Great Dyke which all have higher Co concentrations, in the 350 to 500 ppm range

Nickel concentrations do not show a clear relationship with Cr_2O_3 (Fig. 8f). The concentration of Ni in chromite from massive chromites varies from 500 to 1500 ppm. The chromites from the Emeishan picrites are generally richer in Ni, at 1500 to 2000 ppm, whereas the Ni concentrations in chromites from the komatiites are similar to those of the chromites from the massive chromites.

Trace Elements

Gallium shows a negative correlation with Cr_2O_3 and has a single trend starting at a low of 24 ppm for the chromites from komatiite and the Bushveld sills through to a high for the UG-N chromites, at 60 to 70 ppm (Fig 9a). The chromite from the UG2-W and the UG1 do not fall on this trend. Gallium varies from 50 to 70 ppm in these chromites, but their Cr_2O_3 concentrations are almost constant at 42.5 to 44 weight %.

Scandium concentrations are generally low at <15 ppm and show no correlation with Cr_2O_3 (Fig. 9b). The chromites from Stillwater, the LG6, MG1, UG2-N and the sills of the Bushveld Complex, and Emeishan low-Ti picrites all contain very low Sc concentrations of <6 ppm. In contrast, chromites from the komatiites, the high-Ti picrites and from the MG3, UG1 and UG2-W of the Bushveld contain higher Sc, from 6 to 15 ppm.

For Sn, Hf, Nb and Ta, the data set is limited as the concentrations of these elements in chromite approach detection limits. Hafnium concentrations in the chromites from volcanic rocks

show a broad negative correlation with Cr_2O_3 , with concentrations ranging from 0.01 ppm in komatiites to 0.12 ppm in chromite from the Emeishan high-Ti picrites (Fig. 9c). The Hf concentrations in chromites from the intrusions do not show any clear relationship with Cr_2O_3 . The chromites from the Stillwater Complex tend to have low Hf contents from less than detection limit to 0.04 ppm. In contrast, the LG6 and MG1 chromites are relatively rich in Hf at 0.1 to 0.12 ppm. The chromites from the Great Dyke and from the MG3, UG1 and UG2-W show a wide range of values, from 0.04 to 0.12 ppm.

As in the case of Hf, Sn values do not show a correlation with Cr_2O_3 (Fig. 9d). The chromites from the komatiites, the picrites, the Stillwater Complex and most Bushveld localities cover the range 0.1 to 0.6 ppm. The chromites from the Great Dyke are richer in Sn at 1 to 3 ppm. The time-resolved analysis signals were inspected to establish whether the Great Dyke values are due to inclusions, but the patterns were found to be homogeneous and thus it is assumed that the Great Dyke chromites contain elevated Sn levels.

Tantalum concentrations in chromites from the high-Ti picrites show a negative correlation with Cr_2O_3 and cover the range 0.005 ppm to 0.025 ppm (Fig. 9e). The Ta concentrations for most of the intrusion chromites are close to, or less than, the detection level (0.005 ppm). Exceptions to this are the Great Dyke and MG1 chromites. In both cases, Ta levels exceed 0.01 ppm. As in the case of Ta, Nb concentrations in chromites from the picrites appear to define a negative correlation with Cr_2O_3 (Fig. 9f), covering the range 0.05 to 0.25 ppm. The Nb contents of most intrusion chromites are close to, or less than, the detection level of <0.05 ppm.

Copper concentrations for most chromites are in the 1 to 10 ppm range. An exception to this are some of the chromites from the Emeishan picrites, which contain up to 300 ppm Cu.

491 Park et al. (2017) report similarly high Cu concentrations in chromites from Emeishan picrites
492 and low Cu concentrations in chromites from komatiites. The Emeishan chromites show some
493 zonation with respect to Cu concentrations (Barnes et al. 2022).

494 A number of other elements, namely Ge, Y, Zr, Cd, In and W were measured. Their
495 concentrations are found either to be close to their detection limits or there are possible
496 interferences that still need to be resolved. These elements will not be considered any further.

497

498 **Discussion**

499 Barnes (1998) studied the composition of chromites by considering: a) the influence of
500 the composition of the magma from which chromite crystallized; b) the influence of post-
501 crystallization re-equilibration with the trapped liquid fraction; c) the influence of sub solidus re-
502 equilibration with the silicates during cooling; and d) the influence of metamorphism. More
503 recently, workers have come to appreciate that cumulate systems are rarely closed and thus, after
504 initial crystallization the chromite may have re-equilibrated with interstitial liquid that has
505 replaced or mixed with the liquid from which the chromite crystallized. Thus process b) should
506 more correctly be phrased as post-crystallization re-equilibration with liquid.

507

508 **Partition Coefficients**

509 In order to understand the influence of various processes on the composition of the
510 chromite an estimation of the partition coefficients of the elements between chromite and liquids
511 is helpful (Table 2). There are some results from experiments, and in addition, we have
512 previously estimated partition coefficients based on the composition of the chromite from the
513 Emeishan picrites and modelled Emeishan liquids (Barnes et al. 2022). For the current work, we

have also calculated partition coefficients based on chromite from komatiite. To calculate the partition coefficients between komatiite and chromite one needs to estimate the composition of the komatiite liquid at the time of chromite crystallization. Both experimental and empirical evidence suggest that chromite only begins to crystallize when the MgO content of a komatiite liquid falls to ~ 20 to 25 weight % (Barnes 1998; Keltie 2018). Thus, chromite would not be on the liquidus in the initial komatiite liquid at Alexo, which contained 30 weight % MgO based on the composition of the hyaloclastite flow top (Barnes et al. 1983). To estimate the composition of the komatiite liquid at the time of chromite crystallization the composition of the spinifex textured sample (AX19) with the lowest MgO content (22 weight %) was used to estimate the liquid composition. The composition of AX19 can be modelled as the product of ~ 30 % crystal fractionation from the initial komatiite liquid (Barnes et al. 1983). The partition coefficients estimated for the komatiite chromite are similar to those of the Emeishan chromite (Table 2).

The empirical partition coefficients calculated for the 3+, 4+ and 5+ ions are similar to those from experimental work. The 2+ ions show more variable behavior. In our data set the empirical partition coefficients for Mg, Co, and Ni are lower than those deduced from experimental work. The partition coefficients of Mn, Fe and Zn are within the range of experimental partition coefficients. However, in the Emeishan picrites, concentrations of these elements were found to be significantly lower in chromites included in olivine than in chromites found in the matrix, which suggests that the latter have been modified from their primary compositions (Barnes et al. 2022). Furthermore, the composition of chromite in equilibrium with the modelled Emeishan liquid as calculated by SPINMELTS 2 (Nikolaev et al. 2018) is richer in MgO and poorer in FeO than the observed chromite compositions, whereas the Cr₂O₃, TiO₂ and Al₂O₃ concentrations are similar to calculated values (Barnes et al. 2022). Therefore, in the

following section we will assume that the 3+, 4+ and 5+ ions are the most representative of igneous compositions and that the 2+ ions may have been modified due to post-cumulate processes.

Metamorphism

In the current study none of the samples have experienced metamorphism above lower greenschist facies. Hence, as documented by Barnes (1998), metamorphic effects should be minimal, although he reports mobilization of Mn, Co and Zn during low grade alteration. Enrichment of Mn and Zn was identified along cracks in the chromites of the UG2 (Fig. 10) possibly reflecting this type of alteration. These zones have been excluded from analyses. The Mn concentrations of chromites from the Great Dyke reported by Wilson (1982) (those within the circle on Fig. 8c) are much higher than those reported from the Great Dyke by Mason-Apps (1998) and in our own samples. Samples from within 300 m of the current weathering surface of the Great Dyke have undergone serpentinization (Wilson and Prendergast 1987) and thus it is possible that the high Mn values are the result of this alteration. No clear evidence of Co mobility due to metamorphism or low temperature alteration was observed in our sample set.

Post crystallization re-equilibration with liquid and sub solidus re-equilibration

The composition of chromite from volcanic rocks is subject to two competing effects. On the one hand, the rocks cool quickly, therefore the opportunity for diffusion of ions and re-equilibration of chromite with melt is limited. On the other hand, the ratio of silicate material to chromite is high and therefore each chromite grain is in contact with silicate material with which it could re-equilibrate during cooling. The effects of re-equilibration on the chromite from Emeishan picrites have been considered by comparing chromite compositions from chromite

included in olivine with those in the matrix (Barnes et al. 2022). Inclusion chromites are significantly richer in Mg and Co and poorer in Fe, Mn and Zn, whereas Al, Cr, Ti, Sc, V, Ga, Nb, Ta and Hf concentrations are similar in both types of chromite. These observations for the 2+ ions are in agreement with Barnes (1998), Roeder and Campbell (1985), and Scowen et al. (1991), who attribute the difference in concentrations to reaction between chromite and olivine. Barnes et al. (2022) showed that the 3+, 4+ and 5+ ions in chromite from Emeishan picrites do not appear to have re-equilibrated.

Barnes (1998) reported that in chromite from komatiites Mg#, and Ti, V, Mn, Co, Zn concentrations can be affected by reaction with trapped liquid. As outlined above, on the basis of a comparison of partition coefficients from experimental work and empirical partition coefficients calculated for the komatiite chromite from Alexo, the Mg, Fe, Co and Ni concentrations of chromite in the current study may be altered, but as in the case of the Emeishan study the 3+, 4+ and 5+ elements in the komatiite chromites do not appear to have been modified. The marginal sills of the Bushveld Complex contain <1 % chromite, and these chromites have similar compositions to the chromite from the Alexo komatiites in terms of 3+, 4+ and 5+ elements. The tendency of the 3+, 4+ and 5+ ions in the volcanic and sill rocks to maintain their initial concentrations may be because the chromite and liquid cooled relatively quickly and there was insufficient time for these elements to diffuse due to their slower diffusion rates (Coulthard et al. 2021)

The effects of re-equilibration on the chromite from within the intrusions require serious consideration. The chromite could have been in contact first with a fractionating liquid and subsequently with interstitial silicate minerals at high temperatures for a lengthy period. In addition, the exchange between chromite and interstitial silicate minerals may occur because the

583 equilibrium constant has changed with temperature or because this mineral was not present at the
584 time chromite initially crystallized.

585 The question of how much re-equilibration has occurred is often addressed by
586 considering the amount of chromite in the rock. The logic behind this approach is that the more
587 chromite is present, the less re-equilibration is possible. In the case of Stillwater, both the whole
588 rock compositions of the chromite layers and the composition of the chromite are available.
589 Therefore, the weight % chromite in each sample can be calculated and the possible influence of
590 re-equilibration with silicate material evaluated.

591 Considering first the 2+ ions, there is an increase in Mn, Co and Zn concentrations in
592 chromite from samples containing less than 40 weight % chromite (Figs. 11a to c). Nickel shows
593 no clear trend (Fig. 11d). In contrast with the observations of Barnes (1998) for chromites from
594 komatiites and Langa et al. (2020) for chromites from the UG2, where Mg# decreases as the
595 portion of chromite present decreases, the Mg# of the Stillwater chromites does not show a clear
596 trend (Fig. 11e). Chromite from samples with <40 modal % chromite from the C layers do have
597 lower Mg# than chromite from the massive chromite layers. However, chromites from samples
598 with <40 modal % chromite from the E, J, H and B layers have Mg# similar to the massive
599 chromites (Fig. 11e).

600 The concentrations of Sc, V and Sn (all elements with a charge >2+) are similar in
601 chromites from both massive and disseminated samples (Figs. 12a to c). For TiO₂ and Ga the
602 results are variable. Concentrations of these elements are not enriched in disseminated chromites
603 from zones E, H, B and J relative to chromites from massive chromites (Figs. 12d and e).
604 However, TiO₂ and Ga concentrations in chromites from the C chromites are higher than the

other chromites. The C chromite layers have a low concentration of chromite and also showed a low Mg#, thus enrichment could be due to sub solidus re-equilibration.

Niobium, Hf and Ta concentrations are uniform (not shown), but as they are close to detection levels no clear conclusion can be drawn. The Cr# is higher in the G layer than in the other layers, but there is no correlation with amount of chromite present (Fig. 12f). In summary, in rocks with >40 modal % chromite none of the elements appear to be disturbed. In rocks with <40 modal % chromite the 2+ ions Mn, Fe, Co and Zn are enriched in some of the chromite grains and MgO is depleted. The ions with >2+ charge do not appear to have re-equilibrated.

For most of the Bushveld chromite layers the exact amount of chromite in the samples has not been reported. However, Naldrett et al. (2012) describes their sample set as massive chromite, which implies that they contain at least 50 modal % chromite. Our MG1, MG3, UG1 and UG2 samples are all massive. In the case of our UG1 and UG2-W samples (where whole rock data is available) the weight % chromite present is calculated to be between 70 to 90 weight %, (depending on the sample) equivalent to 64 to 87 modal %. Langa et al. (2021) report that their UG2-W samples contain ~90 modal % chromite (except for 2 samples, which contain low concentrations). Langa et al. (2021) report that their UG2-N layer samples have a more variable chromite content (~2 to 90 modal %) and that the Mg# is constant and >0.4 in rocks containing >40 modal % chromite, but decreases in rocks with <40 modal % chromite.

In order to assess the potential for re-equilibration of the various elements, and because the amount of chromite present in each rock is not always reported, following Langa et al. (2021), we have used Mg# as proxy for re-equilibration. Plots of Mg# versus elements with a 2+ charge show that concentrations of Mn, Co and Zn are higher in chromite with Mg# < 0.4 (Fig. 13a to c). In contrast, Ni does not show clear trends (Fig. 13d).

628 The behaviors of elements with a charge $>2+$ (Ti, Sc, V, G) are more variable (Fig. 14).
629 Concentrations of TiO_2 , V, Ga and Sc in chromites from the UG2-N with $\text{Mg\#} < 0.4$ are higher
630 than those with $\text{Mg\#} > 0.4$. The relative increase is greatest for TiO_2 from ~ 1 weight % to 1.6
631 weight % and least for Ga from ~ 50 ppm to 70 ppm. These increases suggest that TiO_2 , V, Sc
632 and Ga have, as suggested by Langa et al. (2021), re-equilibrated in the rocks with <40 modal%
633 chromite (Figs. 14a to d).

634 In contrast, there is no correlation between Mg\# and Ti, V, Sc and Ga in the UG2-W and
635 the other massive chromite layers, which suggests that there has not been re-equilibration in of
636 these elements in the massive chromite layer. There is a notable difference in V content between
637 the UG2-N chromites and the LG5 to UG2-W chromites. The latter are all much richer in V than
638 the UG2-N and LG1 to LG4 chromites (Fig. 14b). As in the case of V, there is a difference in Sc
639 contents of chromite from different chromite layers. The UG2-W, UG1 and MG3 chromites all
640 cluster with relatively high Sc contents of 6 to 8 ppm, whereas chromites from the UG2-N, the
641 LG6 and the Bushveld sills contain relatively low Sc, at 2 to 6 ppm (Fig. 14c).

642 Niobium, Sn, Hf and Ta (not shown) show no correlation with Mg\# , but many samples
643 are close to detection limits. Therefore, no reliable conclusions can be made. In summary, the
644 UG2-N data show that in rocks with $<40\%$ modal chromite TiO_2 , V, Sc and Ga in chromite are
645 enriched, possibly due to post-crystallization re-equilibration.

646 The Great Dyke samples from our study are massive chromites from layers C8 and C6,
647 (>75 weight % chromite based on whole rock composition) plus a sample from layer C1 (30
648 weight % chromite) and disseminated (1 weight %) chromite from the C1 harzburgites. A plot of
649 Mg\# vs Cr\# shows a limited range of Cr\# for the chromites from layers C1 to C12 (0.70 to 0.80)
650 whereas the Mg\# varies more widely 0.44 to 0.68 (Fig. 15a). The greater variability of the Mg\#

suggests some re-equilibration may have taken place. If we further consider the change in Cr# and Mg# for chromite from layers where massive and disseminated chromite data are available (C1 and C6) we can see a decrease in both Cr# and Mg# in the disseminated chromite. The TiO₂ concentrations in chromites from massive chromite layers are fairly constant and do not vary with Mg# (Fig. 15b). However, the disseminated chromite from the C1 unit appears to be enriched in TiO₂, possibly due to re-equilibration. Nickel concentrations show no clear trends (Fig. 15c). Insufficient data are available to track changes in Zn and Co, except to observe that the disseminated chromites of the C1 layer are enriched in these elements.

In summary, in rocks from within the intrusions where chromite concentrations are <40 modal %, elements with a 2+ charge may have undergone re-equilibration and are therefore not a reliable guide to the melt composition at the time of chromite crystallization. In rocks with chromite concentrations <25 modal %, elements with a charge >2+ may have undergone re-equilibration.

Composition of the parent liquids to the chromites

Variations of TiO₂, V, Ga and Sc with stratigraphic height.

Apart from the major elements, Ti is the element for which most data are available. Given that TiO₂ is incompatible with most of the minerals present (olivine, orthopyroxene and plagioclase, Table 3), but only slightly incompatible with regard to chromite (Table 2), the TiO₂ content of the chromite should rise as the magma evolves. Also, the TiO₂ concentrations of the chromites should be sufficiently high to be reliably determined, thus making it an indicator of fractionation of the liquid.

673 In the case of the Stillwater chromites the TiO_2 contents of the A and B chromite layers
674 (Fig. 16a) are higher (0.6 to 0.7 weight %) than the TiO_2 contents of chromite from layers E and
675 above (0.4 to 0.56 weight %). The C chromite is also relatively enriched in TiO_2 at 0.8 to 1.4
676 weight %, but as mentioned above the chromite content of this layer is low and thus this result is
677 ambiguous. The relatively high TiO_2 in chromites from the lowest two chromite layers may be
678 the result of contamination of the magma with continental crustal rocks. Initial Os isotopes from
679 the lower chromite layers indicated more crustal contamination than in the layers above (Horan
680 et al. 2001). The variations in TiO_2 content with height are mirrored by V and Ga (Figs. 16b and
681 c) which are highest in the A to C chromites, lowest in the G chromite. The concentrations of
682 TiO_2 , V and Ga are higher in the H, I, J and K chromites than in the G chromites and the OB1
683 chromite contain intermediate concentrations. Scandium shows an inverse relationship with
684 stratigraphic height and follows Cr# (Figs. 16d and e), with the highest levels being found in the
685 G chromites and falling to lower levels in the J and K chromites, before rising slightly in the
686 OB1 chromite. The variations in TiO_2 , V and Ga contents of the chromite in layers E and above
687 are relatively small (varying by a factor of 1.4) suggesting that the TiO_2 , V and Ga contents of
688 the magma did not vary greatly during the formation of this section of the intrusion.

689 Chromites from massive layers of the Great Dyke have lower TiO_2 contents than
690 chromites and show a narrow range than those from either the Stillwater Complex or Bushveld
691 Complex at 0.25 to 0.45 vs 0.4 to 0.7 and 0.4 to 1.2 weight % TiO_2 respectively (Figs. 16 to 18).
692 Concentrations in chromites vary slightly in the C12 to C5 units at 0.25 to 0.35 weight % (Fig.
693 17a). Concentrations in chromite from the upper chromite layers C2 and C1 are slightly higher at
694 around 0.45 weight %. An exception to this is the concentration of TiO_2 in the disseminated
695 chromite from the C1 unit, which is higher at around 1 weight %, possibly due to re-

equilibration. Vanadium, Ga and Sc concentrations are only available from chromites C1, C6 and C8. Due to the limited dataset the variations with stratigraphic height will not be discussed here. As in the case of the Stillwater chromites, the TiO_2 content shows an inverse relationship with Cr#, with the highest Cr# in the lower parts of the intrusion and lower Cr# in the C1 and C2 chromites. Also, as in the case of the Stillwater chromites, the limited range in TiO_2 contents of the massive chromite indicates that the TiO_2 content of the magma did not vary greatly during the crystallization of the Ultramafic Sequence although it was slightly higher in the upper parts.

Both the TiO_2 and V contents of chromite from the Bushveld Complex show much wider ranges in concentrations than the Stillwater or Great Dyke chromites. TiO_2 and V concentrations in chromite increase by a factor of approximately three from the marginal sills to the UG2 chromite (Figs. 18a and b). The Cr# also covers a wider range (0.6 to 0.8) than at Stillwater (0.58 to 0.68) and Great Dyke (0.7 to 0.8) (Fig. 18c). For Ga and Sc the data set is more limited, but the concentrations in chromites of the UG2 are also approximately three times those of the sills (Table 1). These wider ranges in chromite compositions indicate that the Bushveld chromites equilibrated with magmas with a wider range of compositions than the Great Dyke and Stillwater chromites and that the magmas were progressively more evolved upwards in the stratigraphic section.

Variations of the elements across individual layers

As discussed in the introduction, many models for the formation of massive chromite layers propose that there is a sudden change in an intensive variable (pressure, compositional of the magma, $f\text{O}_2$), such that chromite became the dominant or sole mineral to crystallize. Brennan et al. (2022) in their investigation of the massive chromite layers from the Esker Intrusive

719 Complex (McFalls Lake greenstone belt of northwest Ontario, Canada) tested this model by
720 considering the behavior of V versus Ga. Their hypothesis is based on the observation that both
721 V and Ga partition into chromite, and thus if chromite is the dominant or sole mineral to
722 crystallize, then the concentrations of these two elements should decrease across a massive
723 chromite layer. However, because both elements are incompatible with the mafic silicates if
724 chromite crystallized in cotectic proportions (~2%) with olivine or orthopyroxene, then the bulk
725 partition coefficients for these elements would be much less than 1 (Table 3) and thus the
726 concentrations of V and Ga should increase across the massive chromite layer. In the case of the
727 Esker Complex they found that these elements increased across the massive chromite layer,
728 which they interpret to indicate that the layer could not have formed by chromite-only
729 crystallization, but instead formed by a combination of processes, beginning with cotectic
730 crystallization of chromite and olivine followed by separation of chromite and silicates to form
731 the chromite layer.

732 This hypothesis can be extended to other elements compatible with chromite. Thus, in
733 addition to V and Ga, concentrations of Mn, Co, Ni and Zn should decrease across massive
734 chromite layers if they formed by chromite-only crystallization, whereas concentrations of TiO_2
735 and Sc should increase. Cross-sections from the UG2-W at Waterval and from the UG2-W and
736 UG1 at Impala mine show variable trends. In the Waterval section, V, Ga, Mn, Co, Ni and Zn all
737 increase by approximately 20 relative % up-section (Figs. 19a to f) inconsistent with chromite-
738 only crystallization. In their study of the Waterval section, Naldrett et al. (2012) also observed
739 that V increased up-section. They nevertheless favored chromite-only crystallization and
740 suggested that the increase in V content in the upper parts of the section was due to an increase
741 in the partition coefficient of V into chromite. Although, they did not state this explicitly, such an

increase in partition coefficient would require a decrease in fO_2 . A change in fO_2 would not, however, change the partition coefficient for Ga and other elements and since the concentrations of a number of elements compatible with chromite increase up-section at Waterval, we do not think that the increase in V is due to a change in partition coefficient. In the case of the Impala UG2-W and UG-1 cross-sections there is very little systematic variation in the concentrations of V, Ga, Mn, Co, Ni or Zn (Figs. 19a to f) across the sections, which once again does not support chromite-only crystallization.

Influence of crystal fractionation on TiO_2 , V, Ga and Sc for all chromites

Below we consider the influence of crystal fractionation on TiO_2 , V, Ga and Sc during crystal fractionation for the whole data set. On plots of these elements against each other, vectors for the composition of chromite after 30 % cotectic crystal fractionation of chromite with olivine, orthopyroxene, clinopyroxene and plagioclase and chromite-only crystallization are shown (Fig. 20). In each case, the composition of an initial chromite was calculated using the bulk partition coefficients in Table 3. The composition of the liquid after 30 % crystal fractionation was calculated assuming 2 weight % chromite plus 98 weight % olivine or orthopyroxene or clinopyroxene or plagioclase, or 100 weight % chromite crystallization. Then the composition of chromite in equilibrium with this liquid was calculated using the partition coefficients in Table 2. For chromites from the layered intrusions, only the chromites from the massive chromites are shown due to the difficulty in assessing the influence of re-equilibration due changes in the liquid composition or exchange with the silicate minerals during cooling.

On the plot of TiO_2 versus Ga all of the chromites, except for those from the high-Ti picrite, plot on a single trend defined by cotectic crystallization of chromite plus olivine or

orthopyroxene or clinopyroxene (Fig. 20a). The chromite from the high Ti-picrites plot on a parallel trend to the other chromites, but are slightly richer in TiO_2 , implying a more TiO_2 -rich parent magma than in the case of the other rocks. It is noteworthy that, despite the presence of primocryst plagioclase in the Upper Critical Zone of the Bushveld Complex, the chromites from this portion of the Bushveld do not appear to follow the plagioclase plus chromite vector, implying that the chromite and plagioclase did not crystallize at the same time.

On a plot of TiO_2 versus V, most of the chromites plot along cotectic vectors for chromite plus olivine or pyroxene, with the komatiite and Great Dyke chromite having the lowest TiO_2 and V concentrations, Stillwater chromites plotting at intermediate levels of TiO_2 and V, and most Bushveld chromites having the highest TiO_2 and V contents (Fig. 20b). Finally, the chromites from the high-Ti picrite are richer in TiO_2 than the other chromites and plot along a shallower trend. It is notable that the V content of all chromites from the Bushveld above the LG4 layer are enriched in V relative to chromite from other intrusions and the volcanic chromite. This implies that either the V content of the magma was much higher (2 to 3 times) than the magma that formed the LG1 to 4 and the UG2-N (and the chromite from other settings) or the partition coefficient for V into chromite was higher.

The oxidation state of V in crustal magmas varies from 3+ to 5+ and hence is sensitive to $f\text{O}_2$. Vanadium 3+ has a much higher partition coefficient into chromite than V^{5+} (Canil et al. 2001, Brenan 2022). Assuming that the V content of the parent magma of the UG2-N and UG-2W are similar and at approximately 200 ppm (based on the composition of the marginal rocks, Barnes et al. 2010) and applying the equation of Canil (2002)

$$\Delta\text{NNO} = \{\log[(V_{\text{liq}}/V_{\text{chr}})*24.1-1]-0.82\}/0.28$$

The $f\text{O}_2$ can be estimated as approximately -2 ΔFMQ and -1 ΔFMQ for the UG2-W and N, respectively. Similar conclusions for the difference in oxidation state of the UG2-W and N have

also been drawn by Dyan (2021). Our estimates are somewhat lower than suggested by the $\text{Fe}^{3+}/\Sigma\text{Fe}$ ratio found by Langa et al. (2021), which suggests a range in $f\text{O}_2$ of between -1 ΔFMQ and 0. The difference in the estimations could be due to a number of factors including re-equilibration of Fe, or underestimation of V in the liquid. Alternatively, the equation of Canil et al. (2002) may not be directly applicable to the UG2 magma composition as the equation is based on a komatiitic magma, whereas the magma that formed the UG-2 was more evolved. Nonetheless, the point remains that $f\text{O}_2$ for the UG2-W appears to have been lower than $f\text{O}_2$ for the UG-2N and most other chromites.

On a plot of Sc versus Ga, the chromites from the komatiites and picrites form trends that are parallel to the olivine plus chromite vector, with the picritic chromite containing slightly more Ga than the komatiitic chromite (Fig. 20c). The Bushveld and Stillwater chromites are richer in Ga than the chromites from the volcanic rocks. This could reflect a higher Ga concentration in the parent magmas of the intrusions relative to the komatiites and picrites, which is consistent with the premise that parent magmas of the intrusions were contaminated with continental crust (Eales and Costin 2012; Horan et al. 2001; Jenkins and Mungall 2018; Maier et al. 2016), because the continental crust is enriched in Ga relative to Sc. It is also notable that the UG2-N chromites are depleted in Sc relative to the UG2-W and other chromites from the Critical Zone. This relative Sc-depletion of the UG2-N chromites could be explained by the crystallization of primocryst clinopyroxene which is a common phase in the northern limb. In contrast to the remainder of the Bushveld where clinopyroxene typically forms an intercumulus phase. The early appearance of cumulus augite in the northern limb is consistent with the generally pervasive contamination of the northern limb magmas by assimilation of footwall shale and carbonate. The two chromite layers from the Dunite Succession of the Great Dyke plot with

812 the komatiites and the chromite from the Stillwater intrusion. As in the case of the TiO_2 versus
813 Ga plot it is noteworthy that the Upper Critical Zone chromites do not plot along a chromite plus
814 plagioclase vector.

815 Turning to the plot proposed by Brenan et al (2022) of V versus Ga (Fig. 20d), most
816 chromites fall on a single trend of increasing V and Ga. Chromites from komatiites, low-Ti
817 picrites and the Bushveld marginal sills have the lowest concentrations of V and Ga, whereas
818 chromite from the UG2, both in the northern and western limb, have the highest concentrations
819 of Ga. As noted above, the Upper Critical Zone chromites are richer in V than other chromites
820 and on this plot cluster together at a higher level than the general trend.

821 Overall, on the plots of Ti, Sc, V and Ga, the samples do not appear to fall along
822 chromite-only crystallization vectors and thus do not support models that require only chromite
823 on the liquidus to form massive chromite.

824

825 *Multi-Element Plots*

826 For the data set as a whole, only MgO shows a positive correlation with Cr (Figs. 7 to 9).
827 The positive correlation between MgO and Cr_2O_3 in these massive chromites is in contrast to
828 chromites inclusions in olivine from volcanic settings (Kamenetsky et al. 2001), but is in
829 agreement with experimental work (Keltie 2018). We suggest that this difference arises because
830 the ratio of chromite to silicate component in massive chromites is much lower than in chromite
831 inclusions in olivine. Thus the massive chromites have undergone re-equilibration to a lesser
832 degree than the inclusion chromites. The positive correlation between MgO and Cr and the
833 negative correlation between the remaining elements and Cr indicates that the bulk partition

coefficient for MgO during crystal fractionation was greater than 1 but for the other elements was less than one.

This observation can be used to design a multi-element plot to compare the composition of the chromites. On this plot the elements have been normalized to chromite in komatiite sample AX37. This is the LabMaTer in-house standard that has been analyzed over 200 times and thus we are confident of the values, listed in Table 1. The elements are plotted in order of their bulk partition coefficient, assuming 2 weight % chromite and 98 weight % olivine (Table 3). From Ni to Zn the elements are controlled by olivine or pyroxene. If only olivine and chromite crystallize then V and Ga are controlled by chromite and Sc, Hf, TiO₂, and Sn should reflect the liquid compositions. If pyroxene has crystallized the concentrations of Sc and V could be lower. If plagioclase crystallized, Ga will be depleted. Contamination of komatiite magma with average continental crustal increases the Sn, Hf, and Ga concentrations.

Chromites from komatiite have approximately flat patterns ranging from 0.5 to 2 times the AX 37 standard (Fig. 21a). The chromites from the low-Ti picrites show similar patterns, but tend to have slightly higher Hf and Ti values (Fig. 21b). The chromites from the high-Ti picrite show similar trace element patterns to komatiites from Ga to Ni, at 1 to 2 times the komatiite. However, they are strongly enriched in Hf and Ti, at 3 to 10 times komatiite and slightly enriched in Sn at 2 to 3 times komatiite (Fig. 21c). As discussed by Barnes et al. (2022), the high-Ti picrite liquids are enriched in Ti, Hf and Sn, and the chromites reflect this.

The shape of the chromite patterns from all of the intrusions show an enrichment in Hf and, in some cases Sn, relative to the other elements, and all chromites except those from the Dunite Succession of the Great Dyke show strong negative Sc anomalies (Figs. 22 and 23). The concentrations of most elements from the massive chromite layers C8 and 6 from the Dunite

857 Succession of the Great Dyke are low, similar to komatiites, and the overall patterns are flat,
858 apart from enrichment in Hf and Sn (Fig 22a). Elements such as Zn and, in some cases Ni, have
859 even lower concentrations, down to 0.4 times komatiite. This pattern is consistent with the Great
860 Dyke chromites having formed from a komatiitic liquid that has experienced some contamination
861 with continental crust, which would have enriched the magma in Hf and Sn. The two chromites
862 from the C1 unit of the Bronzitite Succession are semi-massive and disseminated (Fig. 22a).
863 They have similar patterns to the chromites from the C8 and C6 chromite layers except that the
864 C1 chromites have negative Sc anomalies and are richer in most elements (except Ni). The
865 negative Sc anomalies could be the result of crystallization of pyroxene. The depletion in Ni
866 could be due to olivine crystallization. The higher levels of the other elements that have bulk
867 partition coefficients of less than 1 (Sn, Hf, Ti, Ga and V) may be the result of enrichment in the
868 magma by crystal fractionation. However, Zn, Mn and Co have bulk partition coefficients close
869 to 1 and would thus not be expected to be enriched. As discussed above these elements are
870 susceptible to enrichment by reaction with the silicates and the enrichment of these elements
871 could thus be due to sub solidus re-equilibration as these rocks contain only 30 weight %
872 chromite.

873 The chromites from the massive chromites of the Stillwater Complex, including the
874 massive chromite from the OB1 unit at the level of the JM Reef, exhibit essentially similar
875 patterns (Fig. 22b). From Zn to Ni they overlap with the komatiite patterns. There is a slight
876 enrichment from V through to Ti at 2 to 3 times komatiite, but with a large negative Sc anomaly.
877 Hafnium concentrations are variable from 1 to 4 times komatiite. In some chromites, Sn is
878 strongly enriched at up to 5 times komatiite levels. The negative Sc anomaly suggests that the
879 chromite has equilibrated with a liquid that crystallized pyroxene. Although it is commonly

thought that the interstitial mineral to the chromite at Stillwater is olivine, both olivine and orthopyroxene are present. The ratio of olivine to orthopyroxene in the chromite layers can be estimated using a plot of MgO versus Sc for the whole rock compositions (Fig. 24). This indicates that most of the chromite layers contain olivine and orthopyroxene in a ratio of ~1:1, consistent with the premise that pyroxene crystallization has controlled the Sc content the chromite. The chromite from the semi-massive C layer shows slightly higher concentrations of Ti, Ga, Mn, Co and Ni than the other layers. As discussed above, this enrichment could have occurred due to sub-solidus re-equilibration or could be due to equilibration with a more fractionated liquid.

The patterns of chromite from the marginal sills of the Bushveld Complex show Zn to Ni being present at approximately the level of komatiite chromite, a negative Sc anomaly and a strong enrichment in Sn, Hf and to a lesser extent Ti (Fig. 23a). The cumulate minerals in the marginal sills are olivine and orthopyroxene. The pyroxene probably controlled the Sc. Overall, the enrichment in Sn and Hf relative to the other elements suggests a strong crustal component in the liquid.

The Bushveld chromites from the LG1 to MG2 layers show similar shaped patterns to the chromites from the marginal sills, but are slightly enriched in Hf to V and depleted in Zn to Ni (Fig. 23a). The chromites from the MG3, MG4 and UG1 also show similar shaped patterns, except that they are more enriched in Ti to V (Fig. 23b). The overall enrichment in elements from Ti to V and depletion in elements from Zn to Ni relative to the chromites from the marginal sills and komatiite is consistent with equilibration with a more evolved magma.

If we consider only the massive chromites from the UG2-W and the UG2-N, the patterns are similar in shape and level to the UG1 chromites (Fig. 23c). However, the UG2-N chromites contain slightly less Sc, V, Co and Ni and more Zn and Ti.

Summary of the assessment of the composition of the liquids

Of the analyzed samples, the chromites of the Great Dyke from the Dunite Succession are the richest in Cr and have compositions closest to komatiite, apart from the enrichment in Sn and Hf. This supports the idea that the chromites have equilibrated with magma of komatiitic composition. The compositions of the chromites from the Bronze Succession are slightly poorer in Cr and richer in Ga, V and Ti, and have negative Sc anomalies. These characteristics suggest that the chromites equilibrated with a liquid that was enriched in elements incompatible with olivine, and that the liquid was sufficiently evolved to crystallize pyroxene. Overall, the compositions of the chromites are consistent with a komatiitic liquid that was slightly contaminated with continental crust.

Of all the chromites examined, the Stillwater chromites have the highest Al_2O_3 contents, except for a few of the chromites from the Bushveld UG1 layer. The multi-element patterns of the Stillwater chromites are similar to those from the Bronzite Succession of the Great Dyke, suggesting that the magma was more evolved than the initial magma of the Great Dyke. The chromites could have equilibrated with a komatiite magma contaminated with continental crust (as suggested for the Stillwater silicate rocks; Jenkins and Mungall 2018) but the negative Sc anomalies suggest that chromite composition has been influenced by the presence of orthopyroxene. Interpreting the relative timing of crystallization of the olivine, orthopyroxene and chromite depends on one's interpretation of how the orthopyroxene oikocrysts formed.

Jackson (1961) argued that they are the product of a peritectic reaction of fractionated liquid with olivine. On the other hand, orthopyroxene crystallization could have been delayed relative to olivine crystallization due to the differences in energy of nucleation. In this case, crystallization of orthopyroxene would have been rapid and would have engulfed the pre-existing olivine and chromite grains once the energy barrier was overcome. This topic is beyond the scope of the current work. However, the influence of orthopyroxene on the chromite composition seems reasonable as in most samples chromite is not included in olivine, but is either included in orthopyroxene or interstitial to both orthopyroxene and olivine (Fig. 3e).

Bushveld chromites cover a wider range of compositions than either the Great Dyke or Stillwater chromite. The chromites from the floor sills and the LG1 to LG4 chromite layers are similar in composition to chromite from komatiite magmas, but have negative Sc anomalies and enrichment in Sn and Hf. The initial magma at the Bushveld is thought to be a komatiite contaminated with a large amount of upper crust (Barnes et al. 2010, Eales and Costin 2012, Maier et al. 2016; Wilson 2012) and would be a suitable liquid to crystallize these chromites. At the level of the UG2 layer, the concentration of elements incompatible with olivine and orthopyroxene (Hf, Ti, Ga, Sc and V) has increased by factors two to three. If this change were simply brought about by crystal fractionation then 50 to 66 % crystal fractionation would be required and the liquid composition would not be appropriate to crystallize chromite. Therefore, other process(es) are needed to enrich these chromites in the incompatible elements. One possible model is outlined below.

Formation of a massive chromite layer

The various models that require chromite-only crystallization are not consistent with variations in Ga, V, Ti and Sc throughout the dataset and across individual massive chromite layers, namely the UG2 and UG1. This suggests that models invoking changes in intensive variables, such as pressure, composition and/or fO_2 to form massive chromite layers are not viable. The variations in these elements are consistent with crystallization of chromite and mafic minerals in cotectic proportions. This requires a mechanism to separate the chromite and most of the silicate minerals after crystallization.

We suggest a more elaborate model involving semi-consolidated cumulates containing cotectic proportions of chromite slumped towards the center of the intrusions. (This model does not preclude settling of chromite clusters at a particular stage.) The slumping model is consistent with the variation in thickness of the layers. For example, Wilson and Prendergast (1989) pointed out that in the Great Dyke the chromite layers are thin and disseminated at the margins of the intrusion but thicken and become more massive towards the center. Similar types of structures can be observed on the thin section scale at Stillwater (Fig. 3f). The slumping model is also consistent with complex structures observed in some layers observed both at Stillwater and the Bushveld. For example the UG1 layer at Dwars River of the Bushveld is famous for the complex structures associated with it. There is ample evidence for disruption of the layers, such as anorthosites clasts within the chromite layers (Fig. 5c) and chaotic layering beneath the layer (Fig. 5d) and the bifurcation of the chromite layers. These complex structures are not confined to Dwars River. Nex (2004) documents these features from six localities around the western and eastern limbs of the Bushveld and attributes them to liquefaction of the underlying unconsolidated anorthosites caused by major magma influx and associated seismicity. We suggest that the magma(s) in question is actually a chromite slurry which either slumped from

969 the side walls of the chamber or formed in a feeder chamber at depth and was then emplaced into
970 the chamber.

971 The reason for slumping could be the collapse of the floor of the chamber due to melting
972 and/or mobilization of the country rock at the base of the intrusion. Alternatively, it could be the
973 result of a fresh injection of magma accompanied by earthquakes. It should be noted that the
974 slumping was not necessarily a single event. There could have been repeated events, and as
975 shown by Forien et al.'s (2016) experimental work, this could result in younger surges injecting
976 into older cumulates, thereby thickening layers. Slumping could also explain the lack of variation
977 in chromite composition across the 1 m thick UG1 and 2 layers at Impala and the anomaly of
978 plagioclase oikocrysts enclosing chromites. Fractional crystallization of the B1 magma could
979 produce chromite of the observed Cr# and Mg# but plagioclase would not have been on the
980 liquidus at the point at which chromite crystallizes. In this model the layers formed by injection
981 of a chromite-orthopyroxene slurry into a semi-consolidated anorthosite. During transport the
982 chromite collected at the base of the slurry. There would be little compositional change across
983 the section because any variations due to crystal fractionation have been obscured by the mixing
984 of the grains during transport. A second process that should be considered is that in order for the
985 slurry to move it would needed to have contained at least 30% liquid. Furthermore, if the
986 underlying anorthosite still contained a liquid this interstitial anorthosite liquid would have been
987 more fractionated than the slurry liquid and not in equilibrium with the chromite. During
988 compaction the slurry liquid and anorthosites liquid could mix and pass through the chromite
989 slurry causing re-equilibration of the chromite to a broadly similar composition across the beds
990 and enriching the chromite in incompatible elements. This mixed liquid could also have
991 crystallized the plagioclase oikocrysts.

992 **Conclusions**

993 The concentrations of elements with a charge $>2+$ (Al, Sc, Ti, Cr, V, Ga, Nb, Sn, Hf and
994 Ta) in disseminated chromites from volcanic rocks (Alexo komatiite and Emeishan picrites) and
995 the marginal sills of the Bushveld Complex reflect the composition of the melts they crystallized
996 from. The elements with a $2+$ charge appear to have been disturbed after initial crystallization.
997 This could occur during equilibrium crystallization, whereby the chromite consistently re-
998 equilibrated with the fractionating magma. Alternatively, it could occur after solidification, due
999 to changes in the partition coefficients between the silicate minerals and chromite as the
1000 temperature fell. Both processes are aided by the high silicate to oxide ratio in the volcanic rocks
1001 and the fast diffusion coefficients for these elements.

1002 The variations in the concentrations of elements with $>2+$ charge in chromite from
1003 komatiite and picrite plot along olivine plus chromite crystallization trends and the multi-element
1004 patterns are similar, except that the high-Ti picrites are enriched in Sn, Hf and Ti, reflecting the
1005 composition of the magmas.

1006 Disseminated chromites from the intrusions show enrichment in Mn, Fe, Co, Zn and, to a
1007 lesser extent, Ti, V and Ga. As in the case of the volcanic rocks this can be attributed to re-
1008 equilibration of the initial chromite with a more fractionated liquid or due to post-solidification
1009 re-equilibration with the surrounding silicate minerals. The concentrations of these elements in
1010 chromite from massive chromites layers from the same settings are fairly constant suggesting
1011 that they have not re-equilibrated.

1012 With the exception of the chromite from the Dunite Succession of the Great Dyke the
1013 intrusion chromites all have negative Sc anomalies on multi-element plots, interpreted to be due
1014 to pyroxene crystallization. On the multi-element plots all of the intrusion chromites are enriched

in Hf and, in some cases, Sn relative to the other elements. This is attributed to contamination of a komatiitic parent magma with continental crust.

On plots of V, Ti, Ga and Sc the chromites from the intrusions follow vectors defined by chromite plus olivine or pyroxene in cotectic proportions. This is inconsistent with models of chromite-only crystallization. Furthermore, variations in the changes in concentrations of these elements across the individual layers of massive chromite (UG2 and UG1 layers) do not support the hypothesis of chromite-only crystallization. We favor the formation of the chromite layers by slumping of a slurry of chromite, pyroxene and/or olivine onto and into semi-consolidated cumulates during which the chromite is concentrated at the base of the slurries. After coming to rest the residual liquids from the slurry and the underlying cumulate may mix resulting in some re-equilibration of the chromite as the mixed liquid rises through the chromite layer.

Acknowledgements

SJB would like to thank Canadian Journal of Earth Science for the invitation to submit a review manuscript on a subject of her choice. Two reviewers (Dr. Chris Jenkins and Dr. Vadim Kamenetsky) are thanked for their reviews and the editor for handling the manuscript. This work was supported by a Natural Science and Engineering Discovery grant (*1884-2013*) and the Canada Research Chair grant (*215503*) to SJB. In addition, support for the komatiite chromite project was provided by the Geological Survey of Canada with a Targeted Geoscience Initiative 4 (TGI-4) grant. Northam Platinum is thanked for access to the MG1 and MG3 samples. The Stillwater samples were collected under the guidance of Dr. Mike Zientek of the United States Geological Survey and with the help of Dr. Philippe Pagé of IOS Services Géoscientifiques,

1037 Chicoutimi, both are warmly thanked. Mr. Dany Savard, Ms. Audrey Lavoie and Dr. Christopher
1038 Beckett-Brown are thanked for their support of laboratory work.

1039

1040 **Competing interests:** The authors declare there are no competing interests.

1041 **Roles of the authors**

1042 Sarah-Jane Barnes, -principal author, sample collection komatiites, Great Dyke, Bushveld LG6,
1043 marginal sills

1044 Eduardo Mansur LA-ICP-MS data collection except komatiites, editing and figure drafting

1045 Wolfgang Maier Sample collection Bushveld UG1, UG2, geological setting information, editing

1046 Steve Prevec Sample collection MG1 and MG3, geological setting information, editing and

1047 figure 4.

References.

- Arai, S. 1997. Origin of podiform chromitites. *Journal of Asian Earth Sciences* **15**(2-3): 303-310.
- Arguin, J.-P., Pagé, P., Barnes, S.-J., Yu, S.-Y., and Song, X.-Y. 2016. The effect of chromite crystallization on the distribution of osmium, iridium, ruthenium and rhodium in picritic magmas: an example from the Emeishan Large Igneous Province, Southwestern China. *Journal of Petrology* **57**(5): 1019-1048.
- Alapieti, T.T., Kujanpää, J., Lahtinen, J.J., and Papunen, H. 1989. The Kemi stratiform chromitite deposit, northern Finland. *Economic Geology* **84**(5): 1057-1077.
- Arunachellan, Y. (2022) Constraints on Cr-PGE Mineralisation: Geochemistry and Petrology of the Middle Group 1 and 3 Chromitites, Western Limb, Bushveld Complex, South Africa. Unpublished Masters thesis, Rhodes University, Makhanda, South Africa. 123 p.
- Barnes, S.-J., Gorton, M.P., and Naldrett, A.J. 1983. A comparative study of olivine and clinopyroxene spinifex flows from Alexo, Abitibi greenstone belt, Ontario, Canada. *Contributions to Mineralogy and Petrology* **83**(3-4): 293-308.
- Barnes, S.-J., Maier, W.D., and Curl, E.A. 2010. Composition of the Marginal Rocks of the Rustenburg Layered Series, Bushveld Complex, South Africa: Implications for the Formation of the Platinum-Group Element Deposits. *Economic Geology* **105**(8): 1491-1511.
- Barnes, S.-J., Pagé, P., Prichard, H.M., Zientek, M.L., and Fisher, P.C. 2016. Chalcophile and platinum-group element distribution in the ULtramafic series of the Stillwater Complex, MT, USA—implications for processes enriching chromite layers in Os, Ir, Ru, and Rh. *Mineralium Deposita* **51**(1): 25-47.
- Barnes, S.-J., Mansur, E.T., and Pagé, P. 2022. Differences in composition of chromites from low-Ti and high-Ti picrites of the Emeishan Large Igneous Province and comparison with chromites of the UG-2 platinum-deposit of the Bushveld complex. *Lithos* **412**: 106613.
- Barnes, S.J. 1998. Chromite in komatiites, 1. Magmatic Controls on Crystallization and Composition. *Journal of Petrology* **39**(10): 1689-1720.
- Barnes, S.J. 2000. Chromite in komatiites, II. Modification during greenschist to mid-amphibolite facies metamorphism. *Journal of Petrology* **41**(3): 387-409.
- Barnes, S.J., and Roeder, P.L. 2001. The range of spinel compositions in terrestrial mafic and ultramafic rocks. *Journal of Petrology* **42**(12): 2279-2302.
- Bédard, J.H. 2005. Partitioning coefficients between olivine and silicate melts. *Lithos* **83**(3-4): 394-419.
- Bédard, J.H. 2006. Trace element partitioning in plagioclase feldspar. *Geochimica Cosmochimica Acta* **70**(14): 3717-3742. doi: 10.1016/j.g
- Bédard, J.H. 2007. Trace element partitioning coefficients between silicate melts and orthopyroxene: Parameterizations of D variations. *Chemical Geology* **244**(1-2): 263-303.
- Bédard, J.H. 2014. Parameterizations of calcic clinopyroxene—Melt trace element partition coefficients. *Geochemistry, Geophysics, Geosystems* **15**(2): 303-336.

- 1090 Brenan, J.M., Finnigan, C.F., McDonough, W.F., and Homolova, V. 2012. Experimental
1091 constraints on the partitioning of Ru, Rh, Ir, Pt and Pd between chromite and silicate
1092 melt: the importance of ferric iron. *Chemical Geology* **302**: 16-32.
- 1093 Brenan, J.M., Woods, K., Mungall, J.E., and Weston, R. 2022 Origin of chromitites in the Esker
1094 Intrusion Complex, Ring of Fire Intrusive Suite, as revealed by chromite trace element
1095 chemistry and simple crystallization models. *Geological Survey of Canada Open File*
1096 8755 p. 1-19.
- 1097 Brough, C., Prichard, H.M., Neary, C., Fisher, P.C., and McDonald, I. 2015. Geochemical
1098 variations within podiform chromitite deposits in the Shetland Ophiolite: Implications for
1099 petrogenesis and PGE concentration. *Economic Geology* **110**(1): 187-208.
- 1100 Campbell, I.H., and Murck, B.W. 1993. Petrology of the G and H chromitite zones in the
1101 Mountain View area of the Stillwater Complex, Montana. *Journal of Petrology* **34**: 291-
1102 316.
- 1103 Cameron, E. 1980. Evolution of the Lower Critical Zone, central sector, eastern Bushveld
1104 Complex, and its chromite deposits. *Economic Geology* **75**(6): 845-871.
- 1105 Canil, D. 2002. Vanadium in peridotites, mantle redox and tectonic environments: Archean to
1106 present. *Earth and Planetary Science Letters* **195**(1): 75-90.
- 1107 Cawthorn, R.G., 2005. Pressure fluctuations and the formation of the PGE-rich Merensky and
1108 chromitite reefs, Bushveld Complex. *Mineralium Deposita* **40**(2): 231-235.
- 1109 Cawthorn, R.G., and Walraven, F. 1998. Emplacement and crystallization time for the Bushveld
1110 Complex. *Journal of Petrology* **39**(9): 1669-1687.
- 1111 Cawthorn, R.G., Barnes, S.J., Ballhaus, C., and Malitch, K. 2005. Platinum Group Element,
1112 Chromium, and Vanadium Deposits in Mafic and Ultramafic Rocks. *In* *Economic*
1113 *Geology 100th Anniversary Volume. Editors J.W. Hedenquist, J.F.H. Thompson, R.J.*
1114 *Goldfarb and J.P. Richards. Society Economic Geologist. p. 215-249.*
- 1115 Chaumba, J.B., and Musa, C.T. 2020. Geochemistry of the chromitite stringer at the contact of
1116 the mafic sequence and the ultramafic sequence in the Unki Mine area, Shurugwi
1117 Subchamber of the Great Dyke, Zimbabwe. *The Canadian Mineralogist* **58**(3): 313-333.
- 1118 Cooper, R.W. 1997. Magmatic unconformities and stratigraphic relations in the Peridotite zone,
1119 Stillwater Complex, Montana. *Canadian Journal of Earth Sciences* **34**(4): 407-425.
- 1120 Coulthard, D.A., Zellmer, G.F., Tomiya, A., Jégo, S., and Brahm, R. 2021. Petrogenetic
1121 implications of chromite-seeded boninite crystallization experiments: Providing a basis
1122 for chromite-melt diffusion chronometry in an oxybarometric context. *Geochimica*
1123 *Cosmochimica Acta* **297**: 179-202.
- 1124 Dyan, S. 2021 Constraining the role of carbonate assimilation on spinel stability in oxide ores of
1125 the Flatreef, Bushveld Complex, South Africa, Unpub Masters thesis Rhodes University,
1126 Makhanda, South Africa, 183 pp.
- 1127 Eales, H.V. 2000. Implications of the chromium budget of the Western Limb of the Bushveld
1128 Complex. *South African Journal of Geology* **103**(2): 141-150.
- 1129 Eales, H.V., and Cawthorn, R.G. 1996. The Bushveld Complex. *In* *Layered Intrusions. Editor*
1130 *R.G. Cawthorn. Elsevier, Amsterdam. pp. 181-229.*
- 1131

- Eales, H.V., and Costin, G. 2012. Crustally contaminated komatiite: primary source of the chromitites and Marginal, Lower, and Critical Zone magmas in a staging chamber beneath the Bushveld Complex. *Economic Geology* **107**(4): 645-665.
- Engelbrecht, J.P. 1985. The chromites of the Bushveld Complex in the Nietverdiend area. *Economic Geology* **80**(4): 896-910.
- Forien, M., Tremblay, J., Barnes, S.-J., Burgisser, A., and Page, P. 2015. The role of viscous particle segregation in forming chromite layers from slumped crystal slurries: insights from analogue experiments. *Journal of Petrology* **56**(12): 2425-2444.
- Gain, S.B. 1985. The geologic setting of the platiniferous UG2 chromitite layer on Maandagshoek, Eastern Bushveld Complex. *Economic Geology* **80**: 925-943.
- González-Jiménez, J.M., Griffin, W.L., Proenza, J.A., Gervilla, F., O'Reilly, S.Y., Akbulut, M., Pearson, N.J., and Arai, S. 2014. Chromitites in ophiolites: How, where, when, why? Part II. The crystallization of chromitites. *Lithos* **189**: 140-158.
- Grobler, D. F., Brits, J., Maier, W.D., and Crossingham, A. 2019. Litho-and chemostratigraphy of the Flatreef PGE deposit, northern Bushveld Complex. *Mineralium Deposita* **54**(1): 3-28.
- Hall, A.L. 1932. The Bushveld Igneous Complex in the central Transvaal. Geological Society, South Africa. p. 544.
- Horan, M.F., Morgan, J.W., Walker, R.J., and Cooper, R.W. 2001. Re–Os isotopic constraints on magma mixing in the Peridotite zone of the Stillwater complex, Montana, USA. *Contributions to Mineralogy and Petrology* **141**(4): 446-457.
- Horn, I.H., and Jenner, G. A. 1994. Compositional dependencies of the partition coefficients for Zr, Nb, Ta, Hf and selected transition elements between spinel and melt. *Geochim. Cosmochim. Acta* **51**: 1071-1081.
- Houlé, M.G., Leshner, C.M., and Davis, P.C. 2012. Thermomechanical erosion at the Alexo Mine, Abitibi greenstone belt, Ontario: implications for the genesis of komatiite-associated Ni–Cu–(PGE) mineralization. *Mineralium Deposita* **47**(1): 105-128.
- Hulbert, L., and von Gruenewaldt, G. 1985. Textural and compositional features of chromite in the lower and critical zones of the Bushveld Complex south of Potgietersrus. *Economic Geology* **80**(4): 872-895.
- Irvine, T.N. 1975. Crystallization sequences in the Muskox Intrusion and other layered complexes-origin of chromitite layers and similar deposits of other magmatic ores. *Geochimica Cosmochimica Acta* **39**: 991-1020.
- Irvine, T.N. 1977. Origin of chromitite layers in the Muskox intrusion and other stratiform intrusions II.: a new interpretation. *Geology* **5**: 273-277.
- Irvine, T.N. 1979. Rocks whose composition is determined by crystal accumulation and sorting. *In The Evolution of the Igneous rocks: Fiftieth Anniversary perspectives. Editor H.S. Yoder.* Princeton University Press, Princeton. pp. 245-306.
- Irvine, T.N. 1980. Magmatic density currents and cumulus processes. *American Journal of Science* **280**: 1-58.
- Jackson, E.D. 1961. Primary Textures and Mineral Associations in the Ultramafic Zone of the Stillwater Complex, Montana: US Geol. Survey Prof. Paper 358, 106 p.

- Jenkins, M.C., and Mungall, J.E. 2018. Genesis of the Peridotite zone, Stillwater Complex, Montana, USA. *Journal of Petrology* **59**(11): 2157-2189.
- Jolly, W.T. 1982. Progressive metamorphism of komatiites and related Archean lavas of the Abitibi area, Canada. *In* Komatiites. *Editors* Arndt, N. T., and Nisbet, E.G., Geoge Allen and Unwin, London, U.K. p. 247-266.
- Junge, M., Oberthür, T., and Melcher, F. 2014. Cryptic variation of chromite chemistry, platinum group element and platinum group mineral distribution in the UG-2 chromitite_ An example from the Karee mine, western Bushveld Complex, South Africa. *Economic Geology* **109**: 795-810.
- Kamenetsky, V.S., Crawford, A.J., and Meffre, S. 2001. Factors controlling chemistry of magmatic spinel: an empirical study of associated olivine, Cr-spinel and melt inclusions from primitive rocks. *Journal of Petrology* **42**: 655-671.
- Kamenetsky, V.S., Park, J.-W., Mungall, J.E., Pushkarev, E.V., Ivanov, A.V., Kamenetsky, M.B., and Yaxley, G.M. 2015. Crystallization of platinum-group minerals from silicate melts: Evidence from Cr-spinel-hosted inclusions in volcanic rocks. *Geology* **43**: 903-906.
- Kaufmann, F.E., Vukmanovic, Z., Holness, M.B., and Hecht, L. 2018. Orthopyroxene oikocrysts in the MG1 chromitite layer of the Bushveld Complex: implications for cumulate formation and recrystallisation. *Contributions to Mineralogy and Petrology* **173**: 1-20.
- Keltie, E., E. 2018. An experimental study of the role of contamination in the formation of chromitites in the Ring of Fire intrusive suite. Unpublished masters thesis., Dalhousie University, Halifax 133 p
- Kinnaird, J.A., Kruger, F.J., Nex, P.A.M., and Cawthorn, R.G. 2002. Chromitite formation—a key to understanding processes of platinum enrichment. *Applied Earth Science* **111**: 23-35.
- Langa, M.M., Jugo, P.J., Leybourne, M.I., Grobler, D.F., Adetunji, J., and Skogby, H. 2021. Chromite chemistry of a massive chromitite seam in the northern limb of the Bushveld Igneous Complex, South Africa: correlation with the UG-2 in the eastern and western limbs and evidence of variable assimilation of footwall rocks. *Mineralium Deposita* **56**(1): 31-44.
- Latypov, R., Chistyakova, S., and Mukherjee, R. 2017. A novel hypothesis for origin of massive chromitites in the Bushveld Igneous Complex. *Journal of Petrology* **58**(10): 1899-1940.
- Latypov, R., Chistyakova, S., Barnes, S.J., Godel, B., Delaney, G.W., Cleary, P.W., Radermacher, V.J., Campbell, I., and Jakata, K. 2022. Chromitite layers indicate the existence of large, long-lived, and entirely molten magma chambers. *Scientific Reports* **12**(1): 1-15.
- Leshner, C.M., Carson, H., and Houlé, M. 2019. Genesis of chromite deposits by dynamic upgrading of Fe±Ti oxide xenocrysts. *Geology* **47**(3): 207-210.
- Lipin, B.R. 1993. Pressure increases, the formation of chromite seams, and the development of the ULtramafic series in the Stillwater Complex, Montana. *Journal of Petrology* **34**: 955-976.

- 1215 Liu, T.-C., and Presnall, D.C. 1990. Liquidus phase relationships on the join anorthite-forsterite-
 1216 quartz at 20 kbar with applications to basalt petrogenesis and igneous sapphirine.
 1217 Contributions to Mineralogy and Petrology **104**(6): 735-742.
- 1218 Locmelis, M., Pearson, N.J., Barnes, S.J., and Fiorentini, M.L. 2011. Ruthenium in komatiitic
 1219 chromite. *Geochimica Cosmochimica Acta* **75**(13): 3645-3661.
- 1220 McCallum, I.S. 2002. The Stillwater Complex: A review of the geology. In 9th International
 1221 Platinum Symposium Geology and Guide Stillwater Complex, Montana, USA, Billings.
 1222 pp.A1-A25.
- 1223 McCallum, I.S., Raedeke, L.D., and Mathez, E.A. 1980. Investigations of the Stillwater
 1224 Complex: Part I. Stratigraphy and structure of the Banded zone. *American Journal*
 1225 *Science* **280**: 59-87.
- 1226 McLaren, C.H., and De Villiers, J.P. 1982. The platinum-group chemistry and mineralogy of the
 1227 UG-2 chromitite layer of the Bushveld Complex. *Economic Geology* **77**(6): 1348-1366.
- 1228 Maier, W.D, and Barnes, S.-J. 2008. Platinum-group elements in the UG1 and UG2 chromitites,
 1229 and the Bastard reef, at Impala platinum mine, western Bushveld Complex, South Africa:
 1230 Evidence for late magmatic cumulate instability and reef constitution. *South African*
 1231 *Journal of Geology* **111**(2-3): 159-176.
- 1232 Maier, W.D., Barnes, S.-J., and Groves, D. 2013. The Bushveld Complex, South Africa:
 1233 formation of platinum–palladium, chrome-and vanadium-rich layers via hydrodynamic
 1234 sorting of a mobilized cumulate slurry in a large, relatively slowly cooling, subsiding
 1235 magma chamber. *Mineralium Deposita* **48**(1): 1-56.
- 1236 Maier, W.D., Barnes, S.-J., and Karykowski, B. 2016. A chilled margin of komatiite and Mg-rich
 1237 basaltic andesite in the western Bushveld Complex, South Africa. *Contributions to*
 1238 *Mineralogy and Petrology* **171**(6): 1-22.
- 1239 Maier, W.D., Yudovskaya, M., and Jugo, P. 2021. Introduction to the special issue on the
 1240 Flatreef PGE-Ni-Cu deposit, northern limb of the Bushveld Igneous Complex.
 1241 *Mineralium Deposita* **56**(1): 1-10.
- 1242 Manoochchri, S., and Schmidt, M.W. 2014. Settling and compaction of chromite cumulates
 1243 employing a centrifuging piston cylinder and application to layered mafic intrusions.
 1244 *Contributions to Mineralogy and Petrology* **168**(6): #1091.
- 1245 Marsh, J.S., Pasiecznyk, M.J., and Boudreau, A.E. 2021. Formation of chromitite seams and
 1246 associated anorthosites in layered intrusion by reactive volatile-rich fluid infiltration.
 1247 *Journal of Petrology* **62**(2):1-23.
- 1248 Mason-Apps, A.D. 1998. The petrology and geochemistry of the lower pyroxenite succession of
 1249 the Great Dyke in the Mutorashanga area, Unpublished masters thesis Rhodes University
 1250 199p.
- 1251 Meric, J. 2018. Le ruthénium (Ru), iridium (Ir), osmium (Os) et rhodium (Rh) et les éléments
 1252 traces dans des chromites de komatiites issues de la zone Alexo et de la zone
 1253 Hart,(Abitibi, Ontario): un outil diagnostique pour l’exploration de systèmes fertiles.
 1254 Unpublished masters thesis Université du Québec à Chicoutimi. 202 p.
- 1255 Mondal, S.K., and Mathez, E.A. 2007. Origin of the UG2 chromitite layer, Bushveld Complex.
 1256 *Journal of Petrology* **48**(3): 495-510.

- 1257 Mondal, S.K., Khatun, S., Prichard, H.M., Satyanarayanan, M., and Kumar, G.R. 2019.
 1258 Platinum-group element geochemistry of boninite-derived Mesoarchean chromitites and
 1259 ultramafic-mafic cumulate rocks from the Sukinda Massif (Orissa, India). *Ore Geology*
 1260 *Reviews* **104**: 722-744.
- 1261 Mosier, D.L., Singer, D.A., Moring, B.C., and Galloway, J.P., 2012, Podiform chromite
 1262 deposits—database and grade and tonnage models: U.S. Geological Survey Scientific
 1263 Investigations Report 2012-5157, 45 p.
- 1264 Murck, B.W., and Campbell, I.H. 1986. The effects of temperature, oxygen fugacity and melt
 1265 composition on the behaviour of chromium in basic and ultrabasic melts. *Geochimica*
 1266 *Cosmochimica acta* **50**(9): 1871-1887.
- 1267 Naldrett, A.J., Kinnaid, J., Wilson, A., Yudovskaya, M., McQuade, S., Chunnett, G., and
 1268 Stanley, C. 2009. Chromite composition and PGE content of Bushveld chromitites: Part
 1269 1—the Lower and Middle Groups. *Applied Earth Science: Transactions of the Institutions*
 1270 *of Mining and Metallurgy: Section B* **118**(3-4): 131-161.
- 1271 Naldrett, A.J. 2011. Fundamentals of magmatic sulfide deposit. *In* *Magmatic Ni-Cu and PGE*
 1272 *deposits: Geology, Geochemistry, and Genesis. Editors C. Li and E.M. Ripley. Society of*
 1273 *Economic Geologists Lillteton. pp. 1-50.*
- 1274 Naldrett, A.J., Wilson, A., Kinnaid, J., Yudovskaya, M., and Chunnett, G. 2012. The origin of
 1275 chromitites and related PGE mineralization in the Bushveld Complex: new mineralogical
 1276 and petrological constraints. *Mineralium Deposita* **47**(3): 209-232.
- 1277 Nex, P.A.M. 2004. Formation of bifurcating chromitite layers of the UG1 in the Bushveld
 1278 Igneous Complex, an analogy with sand volcanoes. *Journal of the Geological Society*
 1279 **161**(6): 903-909.
- 1280 Nicholson, D.M., and Mathez, E.A. 1991. Petrogenesis of the Merensky Reef in the Rustenburg
 1281 section of the Bushveld Complex. *Contributions to Mineralogy and Petrology* **107**: 293-
 1282 309.
- 1283 Nicklas, R.W., Puchtel, I.S., and Ash, R.D. 2016. High-precision determination of the oxidation
 1284 state of komatiite lavas using vanadium liquid-mineral partitioning. *Chemical Geology*
 1285 **433**: 36-45. doi: <https://doi.org/10.1016/j.chemgeo.2016.04.011>.
- 1286 Nikolaev, G.S., Ariskin, A.A., and Barmina, G.S. 2018. SPINMELT-2.0: Simulation of spinel–
 1287 melt equilibrium in basaltic systems under pressures up to 15 kbar: II. Description of the
 1288 program package, the topology of the Cr-spinel–melt model system, and petrological
 1289 implications. *Geochemistry International* **56**(2): 125-135.
- 1290 Oberthür, T. 2002. Platinum-group element mineralization of the Great Dyke, Zimbabwe. . *Dans*
 1291 *The Geology, Geochemistry, Mineralogy and Mineral Beneficiation of Platinum-Group*
 1292 *Elements. Editor L.J. Cabri. Canadian Institute of Mining, Metallurgy and Petroleum,*
 1293 *Special Vol 54. pp. 483-506.*
- 1294 Oberthür, T. 2011. Platinum-group element mineralization of the main sulfide zone, Great Dyke,
 1295 Zimbabwe. *Reviews in Economic Geology* **17**(12): 329-349.
- 1296 O'Driscoll, B., Donaldson, C.H., Daly, J.S., and Emeleus, C.H. 2009. The roles of melt
 1297 infiltration and cumulate assimilation in the formation of anorthosite and a Cr-spinel
 1298 seam in the Rum Eastern Layered Intrusion, NW Scotland. *Lithos* **111**(1-2): 6-20.
- 1299 Page, N.J. 1977. Stillwater Complex, Montana; rock succession, metamorphism and structure of
 1300 the complex and adjacent rocks. *US Geological Survey Professional Paper* 999: 79 p.

- 1301 Pagé, P., and Barnes, S.-J. 2009. Using trace elements in chromites to constrain the origin of
 1302 podiform chromitites in the Thetford Mines ophiolite, Québec, Canada. *Economic*
 1303 *Geology* **104**(7): 997-1018.
- 1304 Pagé, P., and Barnes, S.-J. 2016. The influence of chromite on osmium, iridium, ruthenium and
 1305 rhodium distribution during early magmatic processes. *Chemical Geology* **420**: 51-68.
- 1306 Pagé, P., Barnes, S.-J., Bédard, J.H., and Zientek, M.L. 2012. In situ determination of Os, Ir, and
 1307 Ru in chromites formed from komatiite, tholeiite and boninite magmas: implications for
 1308 chromite control of Os, Ir and Ru during partial melting and crystal fractionation.
 1309 *Chemical Geology* **302-303**: 3-15.
- 1310 Park J-W, Campbell I.H., and Eggins S.M. 2012. Enrichment of Rh, Ru, Ir and Os in Cr spinels
 1311 from oxidized magmas: evidence from the Ambae volcano, Vanuatu. . *Geochimica*
 1312 *Cosmochimica Acta* **78**: 28-50.
- 1313 Park, J.-W., Kamenetsky, V., Campbell, I., Park, G., Hanski, E., and Pushkarev, E. 2017.
 1314 Empirical constraints on partitioning of platinum group elements between Cr-spinel and
 1315 primitive terrestrial magmas. *Geochimica Cosmochimica Acta* **216**: 393-416.
- 1316 Paton, C., Hellstrom, J., Paul, B., Woodhead, J., and Hergt, J. 2011. Iolite: Freeware for the
 1317 visualisation and processing of mass spectrometric data. *Journal of Analytical Atomic*
 1318 *Spectrometry* **26**(12): 2508-2518.
- 1319 Prevec, S.A. 2019. The Bushveld Complex, South Africa: New Insights and Paradigms.
 1320 *Geoscience Canada*. **45**: 117-135.
- 1321 Prevec, S.A., Largatzis, S.A., Brownscombe, W., and Salge, T. 2021. PGE distribution in
 1322 Merensky wide-reef facies of the Bushveld Complex, South Africa: Evidence for
 1323 localized hydromagmatic control. *The Canadian Mineralogist* **59**(6): 1305-1338.
- 1324 Prichard, H.M., Barnes, S.-J., Fisher, P.C., Pagé, P. and Zientek, M.L. 2017. Laurite and
 1325 associated PGM in the Stillwater chromitites: implications for processes of formation,
 1326 and comparisons with laurite in the Bushveld and ophiolitic chromitites. *The Canadian*
 1327 *Mineralogist* **55**(1): 121-144.
- 1328 Righter, K., Campbell, A.J., Humayun, M., and Hervig, R.L. 2004. Partitioning of Ru, Rh, Pd, e,
 1329 Ir and Au between Cr-bearing spinel, olivine, pyroxene and silicate melts. *Geochimica*
 1330 *and Cosmochimica Acta* **68**: 867-880.
- 1331 Roeder, P.L., and Campbell, I.H. 1985. The effect of postcumulus reactions on composition of
 1332 chrome-spinels from the Jimberlana intrusion. *Journal of Petrology* **26**(3): 763-786.
- 1333 Roeder, P.L. and Reynolds, I. 1991 Crystallization of chromite and chromium solubility in
 1334 basaltic melts. *Journal of Petrology* **32**(5): 909-934.
- 1335 Roeder, P.L., Gofton, E., and Thornber, C. 2006. Cotectic proportions of olivine and spinel in
 1336 olivine-tholeiitic basalt and evaluation of pre-eruptive processes. *Journal of Petrology*
 1337 **47**(5): 883-900.
- 1338 Scoates, J.S., Wall, C.J., Friedman, R.M., Weis, D., Mathez, E.A., and Van Tongeren, J.A. 2021.
 1339 Dating the Bushveld Complex: Timing of Crystallization, Duration of Magmatism, and
 1340 Cooling of the World's Largest Layered Intrusion and Related Rocks. *Journal of*
 1341 *Petrology* **62**(2): <https://doi.org/10.1093/petrology/egaa107>

- 1342 Scoon, R.N., and Teigler, B. 1994. Platinum-group element mineralization in the critical zone of
1343 the western Bushveld Complex; I, Sulfide poor-chromitites below the UG-2. *Economic*
1344 *Geology* **89**(5): 1094-1121.
- 1345 Scowen, P.A.H., Roeder, P.L., and Helz, R.T. 1991. Reequilibration of chromite within Kilauea
1346 Iki lava lake, Hawaii. *Contributions to Mineralogy and Petrology* **107**(1): 8-20.
- 1347 Schulte, R.F., Taylor, R.D., Piatak, N.M., and Seal, R.R., II, 2012, Stratiform chromite deposit
1348 model, chap. E of *Mineral deposit models for resource assessment*: U.S. Geological
1349 Survey Scientific Investigations Report 2010–5070–E, 131 p.
- 1350 Spandler, C., Mavrogenes, J., and Arculus, R. 2005. Origin of chromitites in layered intrusions:
1351 Evidence from chromite-hosted melt inclusions from the Stillwater Complex. *Geology*
1352 **33**(11): 893-896.
- 1353 Todd, S.G., Keith, D.W., Le Roy, L.W., Schissel, D.J., Mann, E.L., and Irvine, T.N. 1982. The
1354 JM platinum-palladium reef of the Stillwater Complex, Montana; I, Stratigraphy and
1355 petrology. *Economic Geology* **77**(6): 1454-1480.
- 1356 Ulmer, G.C. 1969. Experimental Investigations of Chromite Spinel. *In* *Magmatic Ore Deposits*.
1357 *Editor* H.D.B. Wilson. Society of Economic Geologists, Monograph 4, pp 114–131
- 1358 U.S. Geological Survey, 2021, Mineral commodity summaries 2021: U.S. Geological Survey,
1359 200 p., <https://doi.org/10.3133/mcs2021>
- 1360 Veksler, I.V., and Hou, T. 2020. Experimental study on the effects of H₂O upon crystallization
1361 in the Lower and Critical Zones of the Bushveld Complex with an emphasis on
1362 chromitite formation. *Contributions to Mineralogy and Petrology* **175**(9): 1-17.
- 1363 Voordouw, R.J., Gutzmer, J., and Beukes, N.J. 2010. Zoning of platinum group mineral
1364 assemblages in the UG2 chromitite determined through in situ SEM-EDS-based image
1365 analysis. *Mineralium Deposita* **45**(2): 147-159.
- 1366 Wagner, P.A. 1923. The chromite of the Bushveld igneous complex. *South African Journal of*
1367 *Science* **20**(1): 223.
- 1368 Wall, C.J., Scoates, J.S., Weis, D., Friedman, R.M., Amini, M., and Meurer, W.P. 2018. The
1369 Stillwater Complex: integrating zircon geochronological and geochemical constraints on
1370 the age, emplacement history and crystallization of a large, open-system layered
1371 intrusion. *Journal of Petrology* **59**(1): 153-190.
- 1372 Wijbrans, C.,H., Klemme, S., Berndt, J., and Vollmer, C. 2015. Experimental determination of
1373 trace element partition coefficients between spinel and silicate melt: the influence of
1374 chemical composition and oxygen fugacity. *Contributions to Mineralogy and Petrology*
1375 **169**(4): 1-33.
- 1376 Wilson, A.,H. 1982. The geology of the Great ‘Dyke’, Zimbabwe: the ultramafic rocks. *Journal*
1377 *of Petrology* **23**(2): 240-292.
- 1378 Wilson, A.,H., and Prendergast, M.D. 1987. The Great Dyke of Zimbabwe--an overview.
1379 *Guidebook for the 5th Magmatic Sulphides Field Conference* (Harare: Geological Society
1380 of Zimbabwe), 94p.
- 1381 Wilson, A.H., and Prendergast, M.D. 1989. The Great Dyke of Zimbabwe: I-tectonic setting,
1382 stratigraphy, petrology, structure, emplacement and crystallization. *Editor* M. Jones *In*
1383 *Magmatic sulphides; the Zimbabwe volume*. pp. 1-20

- Wilson, A.H. 2012. A Chill Sequence to the Bushveld Complex: Insight into the First Stage of Emplacement and Implications for the Parental Magmas. *Journal of Petrology* **53**(6): 1123-1168. doi: 10.1093/petrology/egs011.
- Wooden, J.L., Czamanske, G.K., and Zientek, M.L. 1991. A lead isotopic study of the Stillwater Complex, Montana: constraints on crustal contamination and source regions. *Contributions to Mineralogy and Petrology* **107**(1): 80-93. doi: 10.1007/BF00311186.
- Worst, B.G. 1960. The Great Dyke of Southern Rhodesia. Government printer.
- Xu, Y., Chung, S.-L., Jahn, B.-m., and Wu, G. 2001. Petrologic and geochemical constraints on the petrogenesis of Permian–Triassic Emeishan flood basalts in southwestern China. *Lithos* **58**(3-4): 145-168.
- Zhou, M.-F., Robinson, P.T., Su, B.-X., Gao, J.-F., Li, J.-W., Yang, J.-S., and Malpas, J. 2014. Compositions of chromite, associated minerals, and parental magmas of podiform chromite deposits: The role of slab contamination of asthenospheric melts in suprasubduction zone environments. *Gondwana Research* **26**(1): 262-283.
- Zientek, M.L., Cooper, R.W., Corson, S.R., and Geraghty, E.P. 2002. Platinum-group element mineralization in the Stillwater Complex, Montana. *In* *Geology, Geochemistry, Mineralogy and Mineral Beneficiation of Platinum Group Element*. Editor L.J. Cabri. Canadian Institute of Mining, Metallurgy and Petroleum, Special Publication vol **54**. pp. 459-481.
- Zientek, M.L. 2012. Magmatic ore deposits in layered intrusions - Descriptive model for reef-type PGE and contact-type Cu-Ni-PGE deposits. Open File Report 2012-10 U.S. Geological Survey 48p.

Figure Captions

Fig. 1 Chrome resources and production 2021 data from U.S. Geological Survey, 2021, Mineral commodity summaries 2021.

Fig. 2 a) Map of the Stillwater Complex showing the principal units and the location of the traverses sampled. Modified after Todd et al. (1982) and Zientek et al. (2002). Dashed line J-M reef. b) Stratigraphic section through the Stillwater Complex, S = two minor sulfide occurrences

Fig 3 Stillwater chromites: a) E zone with chromite doublet showing narrow layers, host rock type pyroxenite; b) G chromite showing thick bottom layer overlain by a number of thin layers, host rock type peridotite; c) Reflected light photomicrograph of chromites showing large chromite grains with triple junctions and smaller euhedral chromite grains; d) Transmitted light photomicrograph of a chromite-rich peridotite (B layer) showing chromite and olivine inclusions in orthopyroxene oikocrysts e) Transmitted light photomicrograph of E chromite layers in pyroxenite. Note the slumping of the bottom layer.

Fig. 4 a) Map of the Bushveld Complex and b) Stratigraphic section through the Bushveld Complex modified after Prevec (2019).

- 1422 Fig. 5 a) Transmitted light photomicrograph of the UG2 chromite (Bushveld) showing chromite
 1423 grains with interstitial plagioclase. b) Transmitted light photomicrograph of UG2 chromite in
 1424 orthopyroxene oikocrysts. c) UG1 chromite layer at Dwars River showing anorthosites base with
 1425 sharp contact with a thick chromite layer containing anorthosites fragments overlain by
 1426 alternating anorthosites and chromite layers, which are in turn overlain by a pyroxenite of the
 1427 next unit. d) Example of the disrupted layering below the UG1.
- 1428 Fig. 6 a) Map of the Great Dyke after Oberthür, (2011) b) Stratigraphic cross section of Great
 1429 Dyke modified after Wilson and Prendergast (1989).
- 1430 Fig 7 Plots of Cr_2O_3 ; versus a) MgO , b) FeOT and c) Al_2O_3 concentrations in chromite.
- 1431 Fig 8 Plots of Cr_2O_3 versus; a) TiO_2 , b) V, c) Mn, d) Zn, e) Co and f) Ni concentrations in
 1432 chromite. Legend as on Fig. 7
- 1433 Fig. 9 Plots of Cr_2O_3 versus; a) Ga, b) Sc, c) Hf, d) Sn, e) Ta and f) Nb concentrations in
 1434 chromite. Legend as on Fig. 7.
- 1435 Fig 10 Oxide and element distributions in a UG2-W chromite grain (sample BC16). Note most
 1436 elements do not show zonation. Manganese and Zn are enriched along cracks in the chromite. Ti-
 1437 rich laths reflect the presence of small ilmenite exsolutions in the chromite. Scale bar 0.5 mm.
- 1438 Fig. 11 Plots of weight % chromite in whole rock vs a) Mn, b) Co, c) Zn, d) Ni and e) Mg\# in
 1439 chromite from Stillwater. Note that for rocks containing <40 weight% chromite Mn, Co and Zn
 1440 higher than for the massive chromite.
- 1441 Fig. 12 Plots of weight % chromite in whole rock versus; a) V, b) Sc, c) Sn, d) TiO_2 , e) Ga, and f)
 1442 Cr\# for chromites from Stillwater. Note that for most chromites the concentrations are similar,
 1443 exceptions to this are TiO_2 and Ga concentrations, which are higher the C chromite.
- 1444 Fig. 13 Plots of Mg\# chromite versus a) Mn, b) Co, c) Zn and d) Ni concentrations in chromites
 1445 from the Bushveld Complex. Note that chromites with $\text{Mg\#} < 0.4$ are enriched in Mn, Co and Zn
 1446 relative to chromites with $\text{Mg\#} > 0.4$ from the same chromite layer.
- 1447 Fig. 14 Plots of Mg\# in chromite versus a) TiO_2 , b) V, c) Sc and d) Ga concentrations in
 1448 chromites from the Bushveld Complex.
- 1449 Fig. 15 Plots of Mg\# in chromite versus a) Cr\# , b) TiO_2 and c) Ni for chromites from the Great
 1450 Dyke.
- 1451 Fig. 16 Variations in; a) TiO_2 , b) V, c) Ga, d) Sc and e) Cr\# of chromites in the chromites layers
 1452 of the Stillwater Complex. Note TiO_2 , V and Ga show the same variations with height and Sc
 1453 and Cr\# show the opposite trends. The chromites are spaced out evenly across the 2.5 km section
 1454 and not at their true stratigraphic height.
- 1455 Fig. 17 Variations in TiO_2 and Cr\# of chromites in the chromites layers of the Great Dyke. The
 1456 chromites are spaced out evenly across the 2 km section and not at their true stratigraphic height.

- 1457 Fig. 18 Variations in a) TiO_2 , b) V, and c) Cr# of chromites in the chromites layers of the
1458 Bushveld Complex. The chromites are spaced out evenly across the 2.5 km section and not at
1459 their true stratigraphic height.
- 1460 Fig. 19 Variations in; a) V, b) Ga, c) Mn, d) Co e) Ni and f) Zn across the UG2 at Waterval Mine
1461 and Impala and the UG1 at Impala. Note the elements do not decrease as they would if chromite
1462 only crystallized.
- 1463 Fig. 20 Plots of TiO_2 versus, a) Ga, b) V and Ga vs c) Sc and d) Ga to illustrate the effects of
1464 olivine, orthopyroxene, clinopyroxene and chromite crystallization. Legend as on Fig. 7.
- 1465 Fig 21 Chromite compositions normalized to komatiite chromite; a) Alexo chromites, b)
1466 Emeishan chromites from Lo-Ti picrites, c) Emeishan chromites from Hi-Ti picrites.
- 1467 Fig 22 Chromite compositions normalized to komatiite chromite; a) Great Dyke chromites, b)
1468 Stillwater chromites
- 1469 Fig 23 Chromite compositions normalized to komatiite chromite; a) Bushveld Complex sills and
1470 Lower Critical Zone chromites, b) MG3, MG4 and UG1 chromites c) UG2-W and UG2-N
1471 chromites.
- 1472 Fig. 24 Plot of MgO versus Sc for whole rock compositions of the ultramafic series of the
1473 Stillwater Complex. Illustrating that most of the chromite-rich rocks contain olivine and
1474 orthopyroxene in the ratio of approximately 1:1.
- 1475

Table 1. Representative analyses of chromites

Locality		Alexo		Emeishan			Bushveld				Great Dyke		Stillwater	
Rock type		cpx spin	B-zone	Lo-Ti	Hi-Ti	sill	LG6	MG3	UG1	UG2	C8	C1d	A	G1
Sample		AX 43	AX 37	BC 06	JC 03	DI 326	BC 13	27B	1184.4	1154.8	GD 3	GD 5	ST 7A	ST 11G1
Microprobe Analyses														
MgO	wt %	13.27	13.74	14.34	10.62	7.50	9.12	8.01	8.95	9.11	13.66	9.17	9.70	10.78
Al2O3	wt %	15.62	13.48	16.55	14.77	11.20	13.94	16.78	17.41	17.14	12.31	14.66	18.74	15.42
SiO2	wt %	0.09	0.12	0.23	0.08	0.22	0.08	0.02	0.01	0.02	0.23	0.16	0.02	0.02
FeOT	wt %	19.14	16.48	20.82	28.21	27.18	26.90	29.02	27.42	27.76	14.69	25.32	28.74	26.04
Cr2O3	wt %	51.32	54.08	47.56	44.75	53.25	47.90	43.25	44.42	43.82	58.96	50.05	40.18	46.01
FeO	wt %	14.45	12.72	13.18	19.29	22.17	20.42	22.30	21.51	21.16	13.26	20.62	20.24	18.16
Fe2O3	wt %	5.22	4.18	8.49	9.91	5.57	7.20	7.47	6.57	7.33	1.59	5.22	9.45	8.76
Mg#		0.62	0.66	0.66	0.50	0.38	0.44	0.39	0.43	0.43	0.65	0.44	0.46	0.51
Cr#		0.69	0.73	0.66	0.67	0.76	0.70	0.63	0.63	0.63	0.76	0.70	0.59	0.67
Fe3+/(FeT)		0.25	0.23	0.37	0.32	0.18	0.24	0.23	0.22	0.24	0.10	0.19	0.30	0.30
LA-ICP-MS Analyses														
Sc	ppm	7.97	7.00	7.18	10.20	1.83	4.98	6.43	7.89	8.26	4.70	5.64	4.63	5.00
Ti	ppm	2176	1501	3227	8255	970	4252	3996	4974	5103	1638	3090	4356	3410 ,
V	ppm	1145	790	583	1175	922	2240	2413	2956	2904	766	1731	2066	1273
Mn	ppm	1318	1395	1516	2099	2512	2358	1871	1872	1769	1133	2256	1761	1550
Co	ppm	221	240	233	251	395	397	289	329	330	230	478	287	281
Ni	ppm	1029	1176	1675	1312	600	1125	1000	1182	1262	1239	751	1188	1158
Cu	ppm	4.22	6.60	33.40	70.34	27.93	1.18	3.96	1.83	1.16	2.50	1.26	1.46	2.33
Zn	ppm	771	608	403	630	952	802	753	717	708	322	869	731	556
Ga	ppm	33.6	28.0	36.0	43.0	20.7	54.2	57.8	65.3	55.5	35.6	50.7	50.3	46.1
Nb	ppm	nd	0.170	0.039	0.084	0.028	0.055	0.016	0.108	0.138	0.056	0.102	0.027	0.020
Sn	ppm	0.275	0.100	0.108	0.298	0.238	0.158	0.247	0.097	0.117	0.909	0.241	0.229	0.221
Hf	ppm	0.016	0.020	0.028	0.071	0.024	0.125	0.046	0.060	0.086	0.087	0.113	0.068	0.021
Ta	ppm	0.002	0.003	0.019	0.008	0.003	0.065	0.006	0.001	0.006	0.024	0.031	0.006	0.006

cpx spin = clinopyroxene spinifex layer, Lo-Ti=Low-Ti picrite, Hi-Ti=high-Ti picrite, FeOT=Total Fe expressed as FeO
FeO, Fe2O3, Mg#, Cr#, Fe3+/(FeT) calculated using Barnes and Roedder (2001) , nd=not determined.

Table 2. Estimation of partition coefficients between calculated liquids and chromite

n	High-Ti Picrite		Low Ti-picrites		ol spin flow		Literature Values		
	ave	σ	ave	σ	ave	σ	Min	Max	Ref
	20		16		6				
Al	1.09	0.17	1.24	0.18	1.56	0.07	0.94	2.70	1,2,3,4
Cd	<0.5		<0.5		nd				
Co	2.71	0.44	2.63	0.21	2.32	0.31	3.30	5.10	2,4,5
Cr	388	124	325	132	107	9	128	270	1,2,3,4
Cu	0.74	0.86	0.66	0.55	0.17	0.02	0.17	0.25	2
Fe	2.69	0.38	2.31	0.40	1.66	0.31	1.25	4.75	1,2,3,4
Ga	3.21	0.74	2.54	0.70	3.20	0.43	2.40	3.80	2,5,6
Hf	0.024	0.013	0.016	0.004	0.022	0.009	0.004	0.008	2
In	0.49	0.14	0.36	0.09	0.62	0.27			
Mg	0.80	0.13	0.84	0.26	0.53	0.10	1.00	2.09	1,2,3,4
Mn	1.45	0.32	1.50	0.39	0.71	0.12	0.70	1.53	1,2,3,4,5
Nb	0.010	0.015	0.005	0.002	nd	nd	0.001	0.002	2
Ni	4.96	2.18	2.77	1.21	1.36	0.27	5.00	18.60	1,2,5
Sc	0.24	0.08	0.16	0.08	0.18	0.04	0.13	0.30	2,4,5
Sn	0.20	0.15	0.13	0.04	0.63	0.08			
Ta	0.009	0.011	0.005	0.004	0.083	0.069	0.001	0.002	2
Ti	0.83	0.17	0.54	0.09	0.60	0.05	0.14	0.78	1,2,3,4,5
V	4.35	0.65	2.92	0.87	4.39	0.60	1.00	10.00	2,4,5,6
Y	0.001	0.000	0.001	0.001	0.003	0.005			
Zn	5.71	1.72	6.47	2.23	8.85	2.36	6.90	10.10	5

n=number of samples, nd = not determined

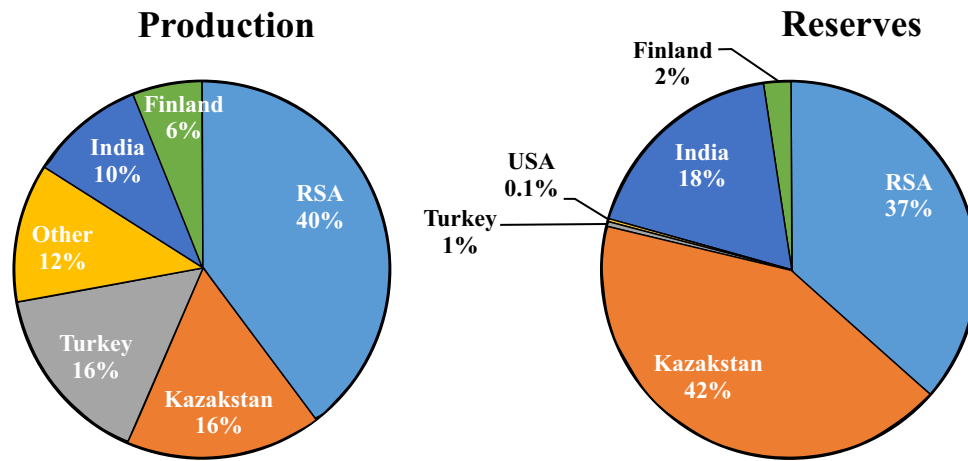
1 Righer et al. (2004), 2 Wijbrans et al. (2015), 3 Brenan et al. (2012)

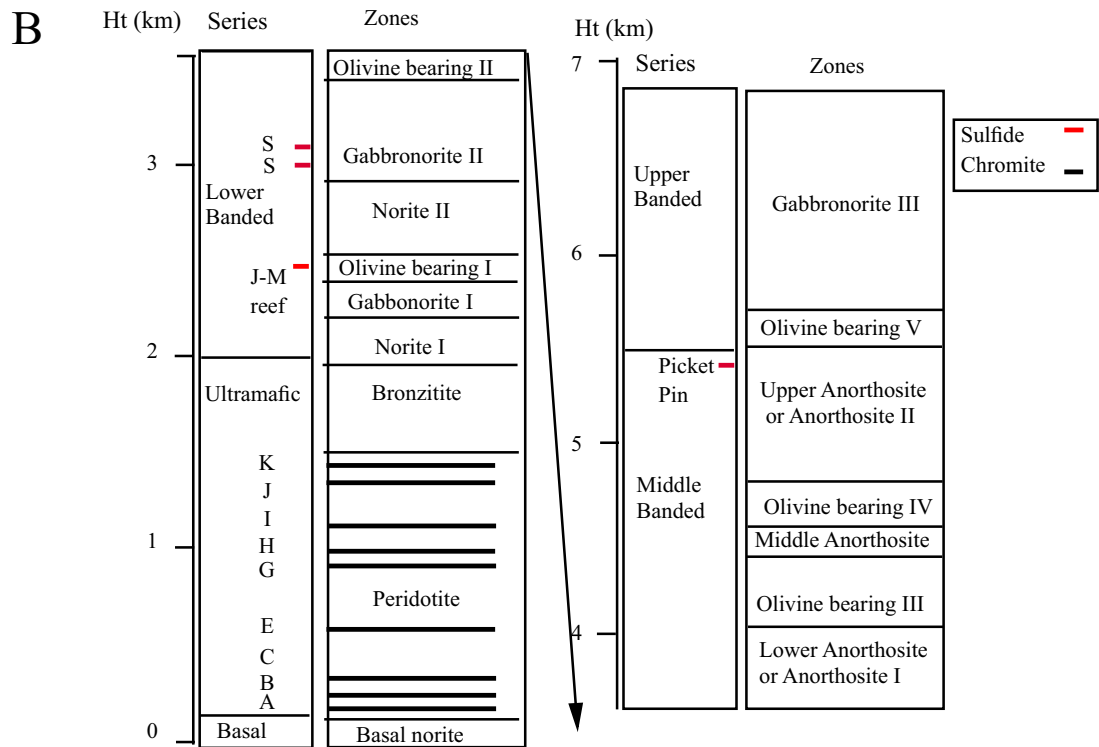
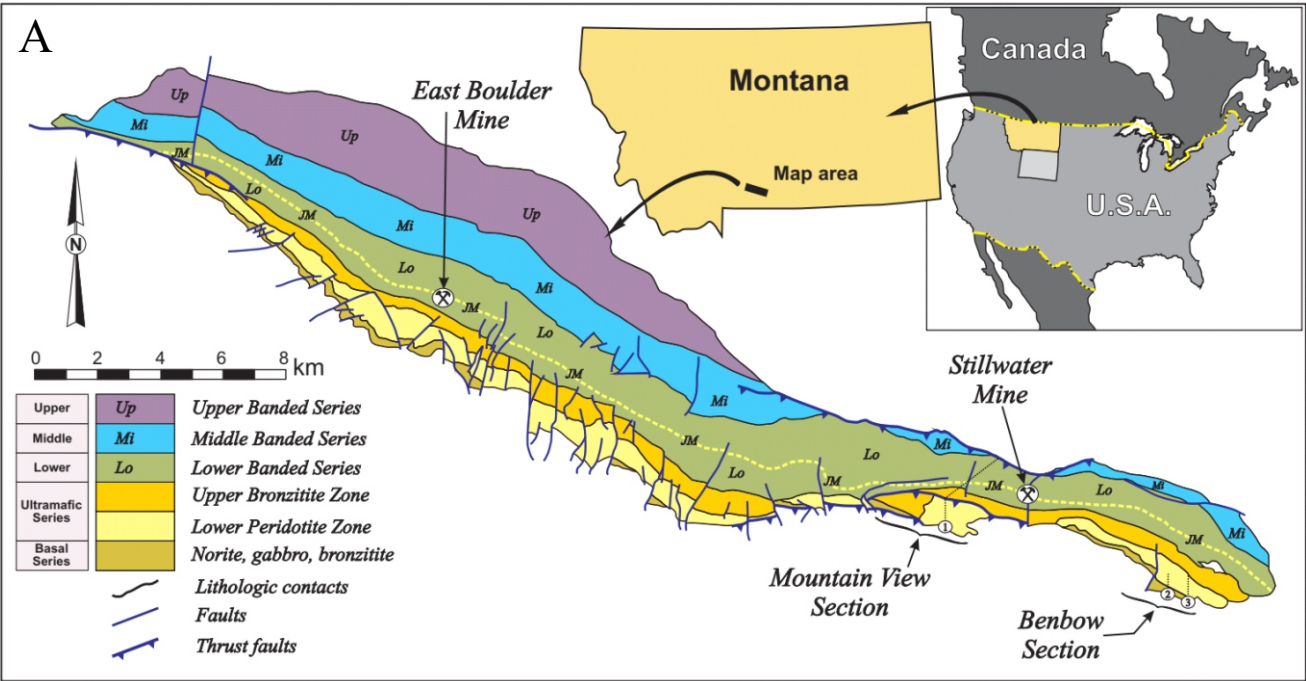
4 Horn and Jenner (1994), 5 Page et al. (2009), 6 Brenan et al. (2021)

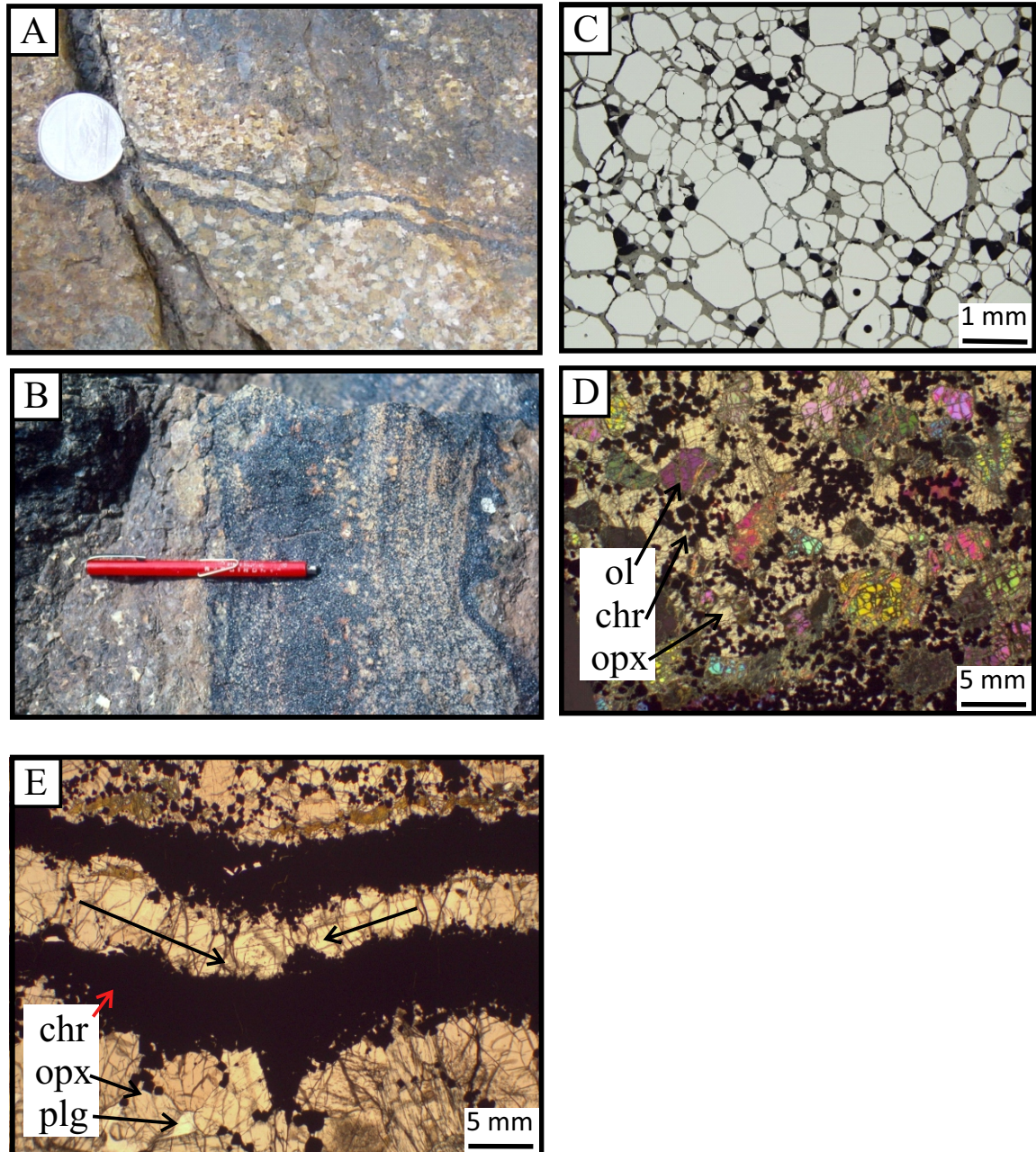
Table 3. Calculation of bulk partition coefficients

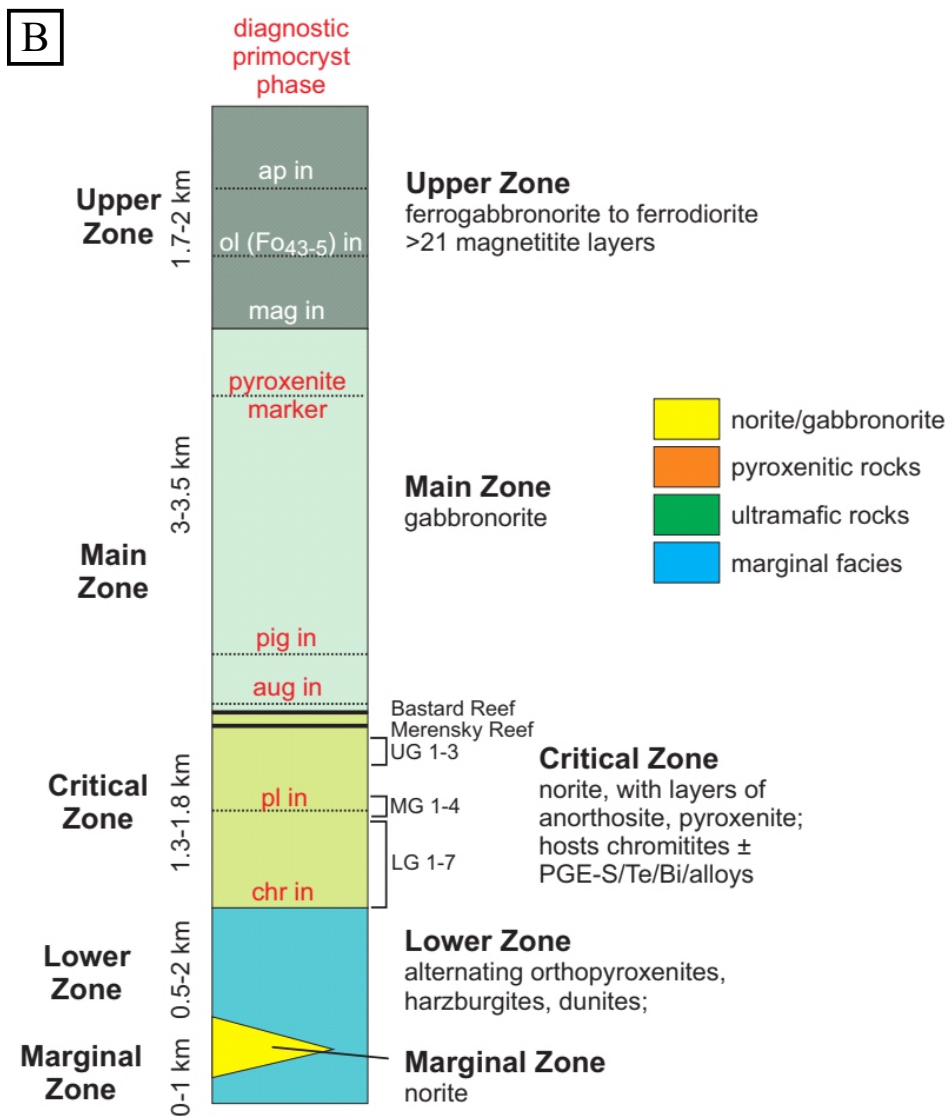
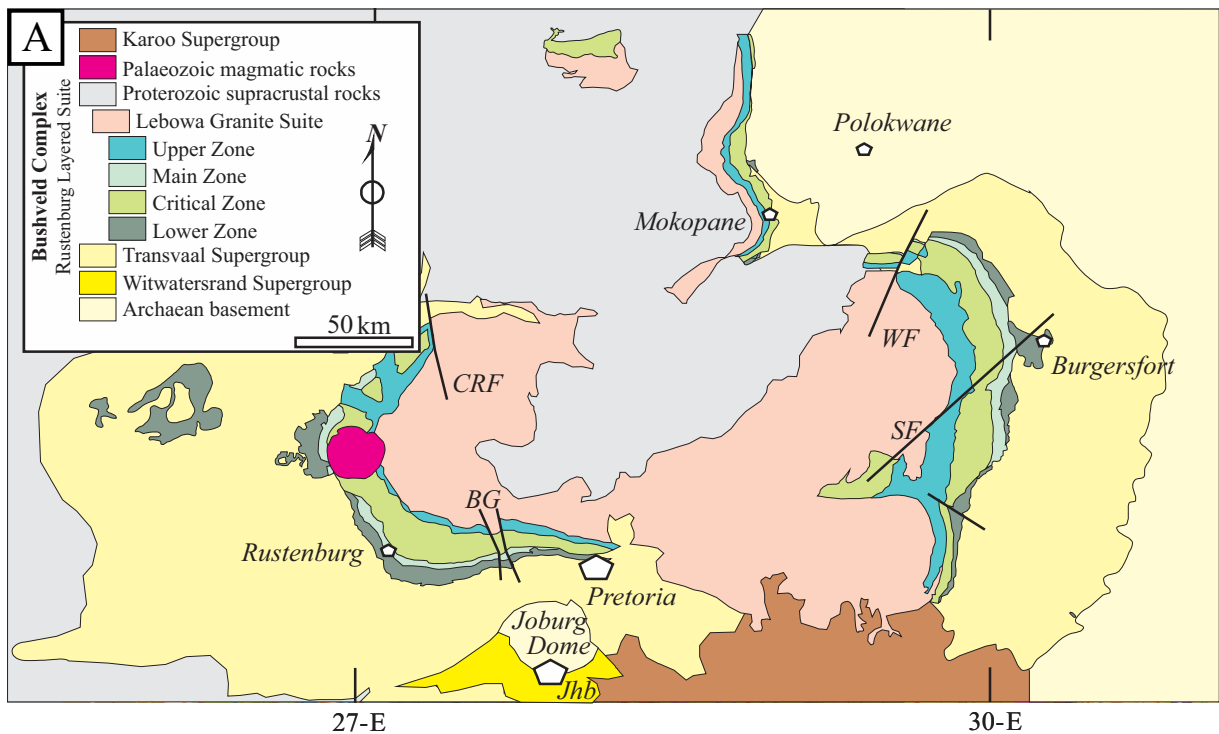
Ref	Partition coefficient used					Bulk D assuming				
	Chr	Ol	Opx	Cpx	Plag	Chr	Ol+chr	Opx+chr	Cpx+chr	Plag+chr
	1,5	2	3	4		100%	98+2%	98+2%	98+2%	98+2%
Ni	5.00	3.3	0.69	2	0.08	5.000	3.334	0.776	2.060	0.178
Co	3.00	1.6	1	1.2	0.09	3.000	1.628	1.040	1.236	0.148
Mn	1.42	1	1.5	1		1.416	1.008	1.498	1.008	0.028
Zn	6.00	0.70	0.60	0.79		6.000	0.806	0.708	0.894	0.120
V	4.30	0.02	0.15	3.1	0.02	4.300	0.106	0.233	3.124	0.106
Sc	0.20	0.12	0.44	3.9	0.02	0.200	0.122	0.435	3.826	0.024
Ga	3.00	0.04	0.17	0.35	1	3.000	0.099	0.227	0.403	1.040
Ti	0.65	0.01	0.11	0.34	0.07	0.650	0.023	0.121	0.346	0.082
Ta	0.01	0.01	0.004	0.01	0.07	0.007	0.010	0.004	0.010	0.069
Hf	0.02	0.005	0.037	0.33	0.01	0.021	0.005	0.037	0.324	0.010
Cu	0.20					0.200	0.004	0.004	0.004	0.004
Sn	0.18					0.176	0.004	0.004	0.004	0.004
Nb	0.01		0.03	0.008	0.03	0.006	0.000	0.030	0.008	0.030

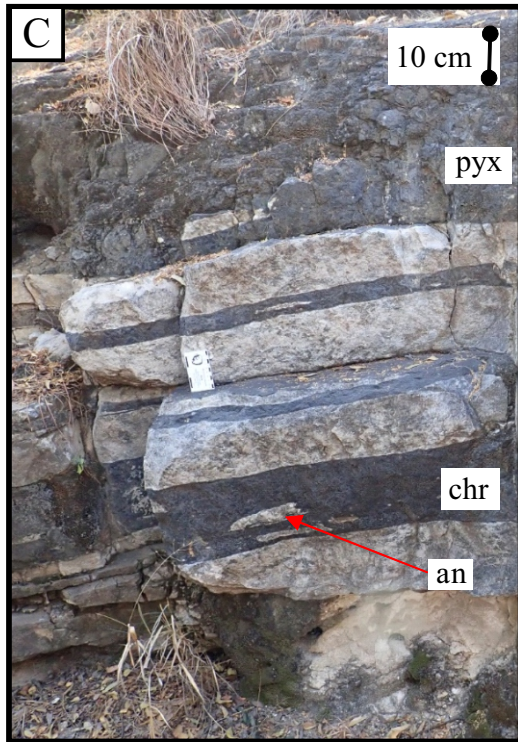
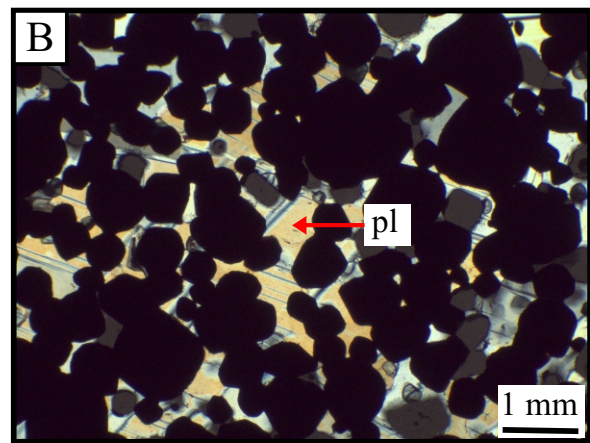
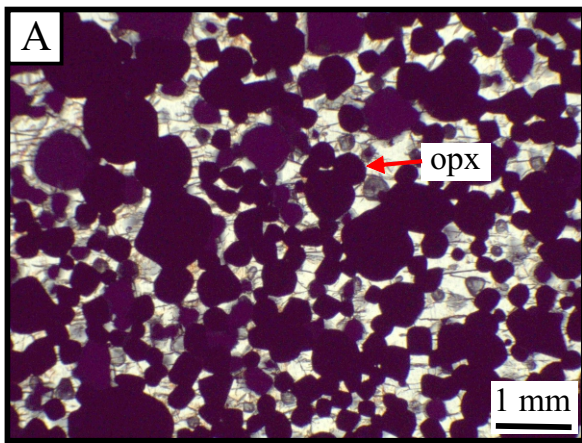
1 Bédard (2005), 2 Bédard (2007) 3 Bédard (2014) 4 Bédard (2006) 5 Brenan et al. (2021)

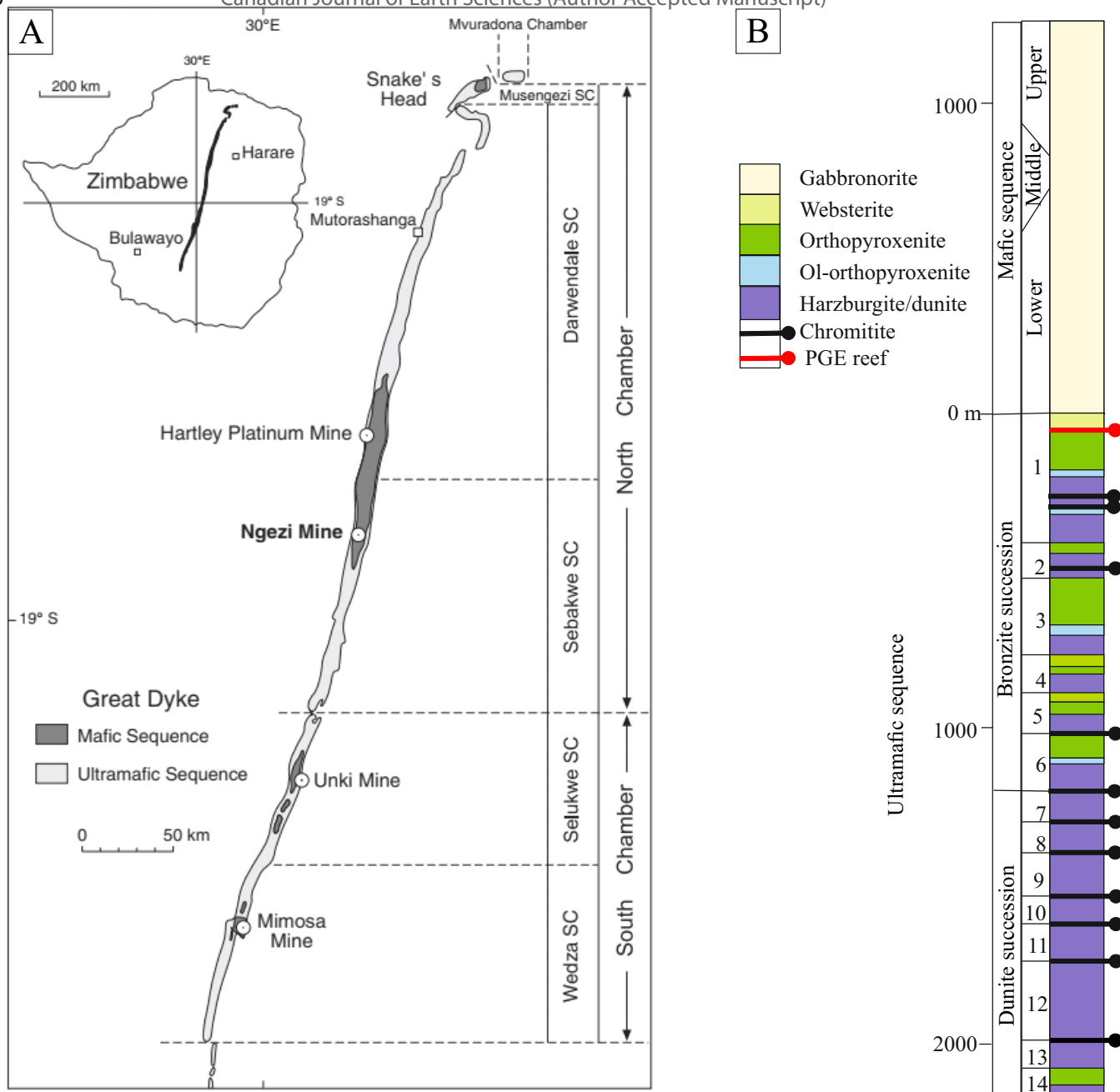


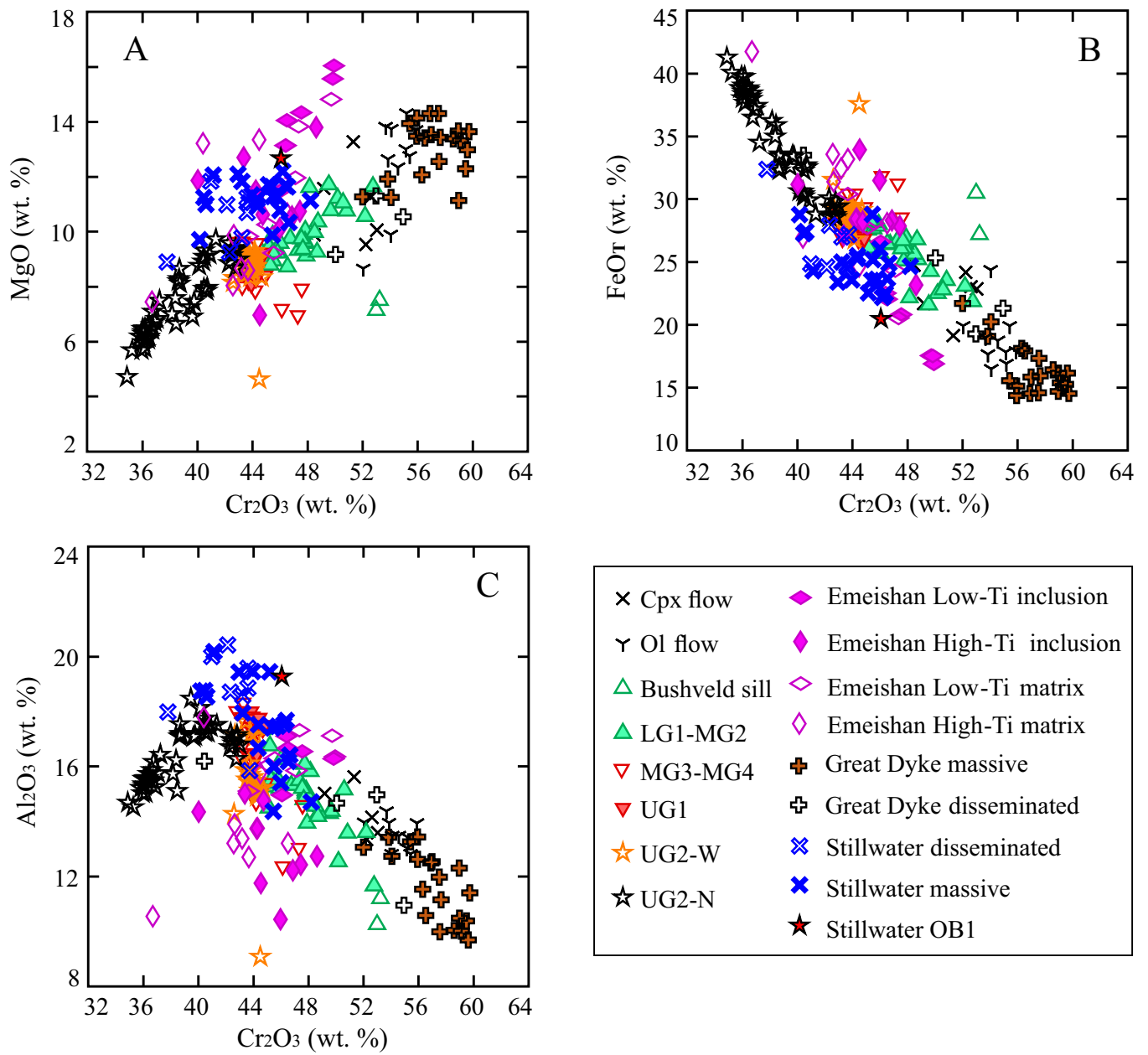


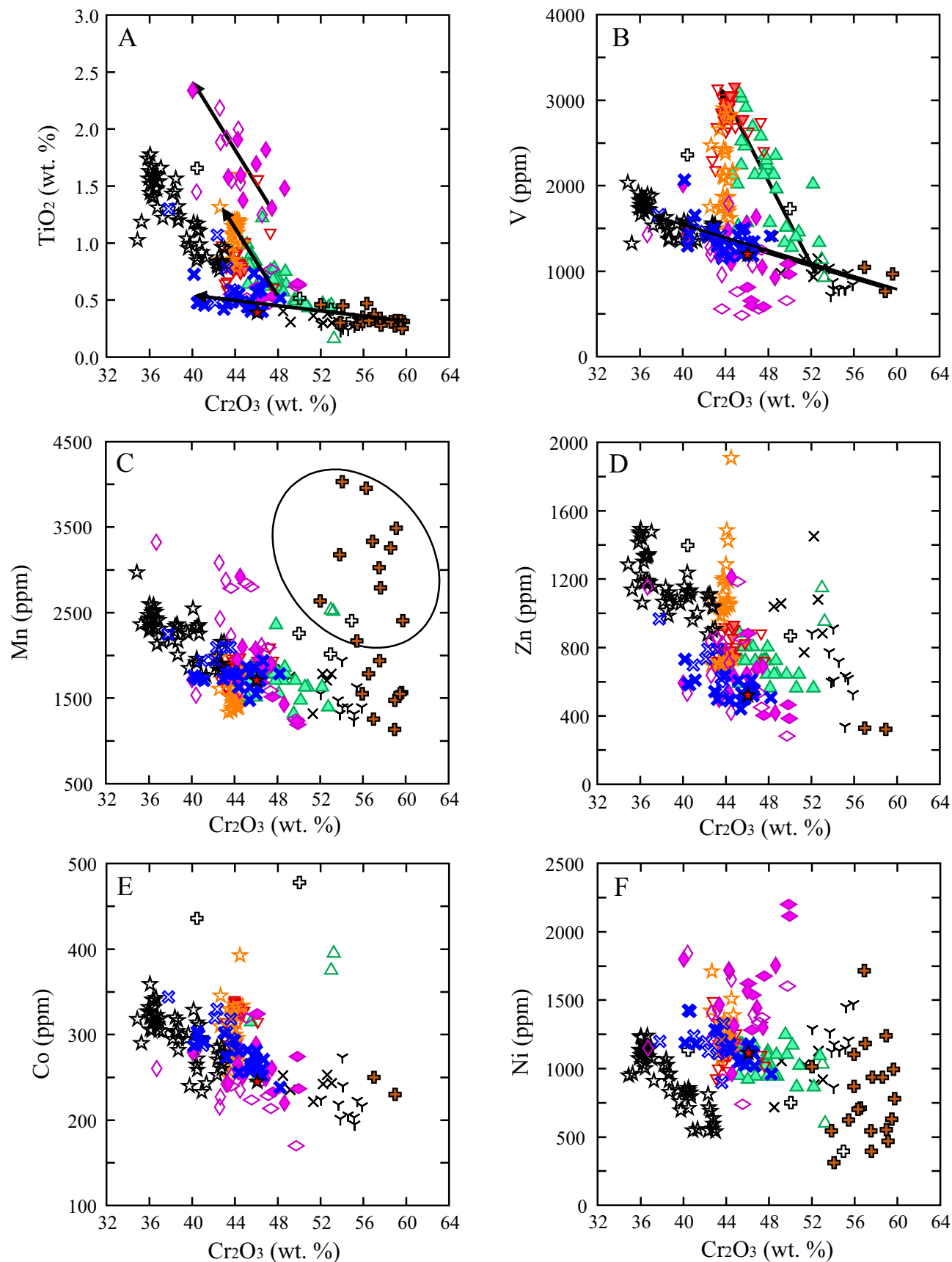


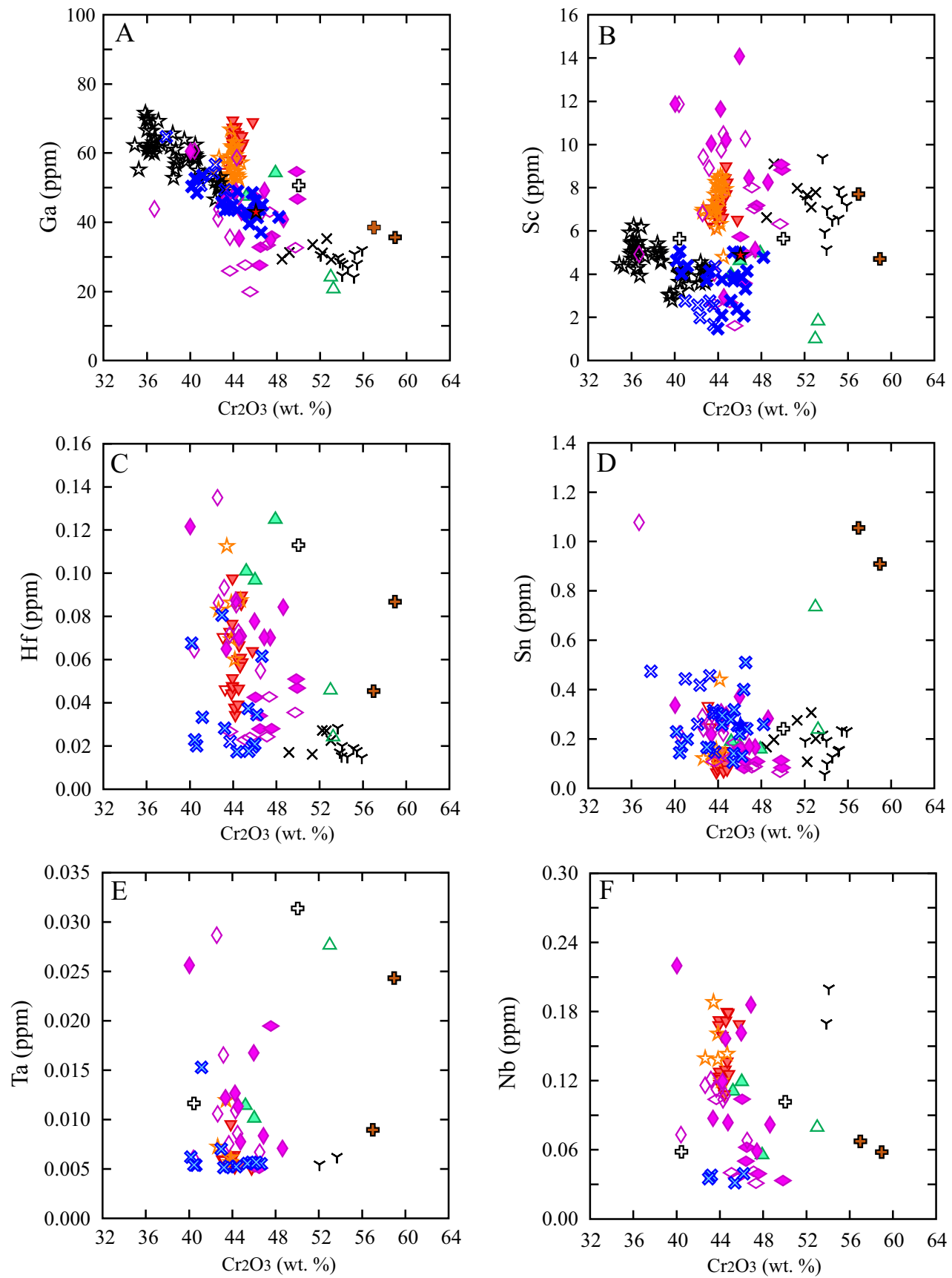


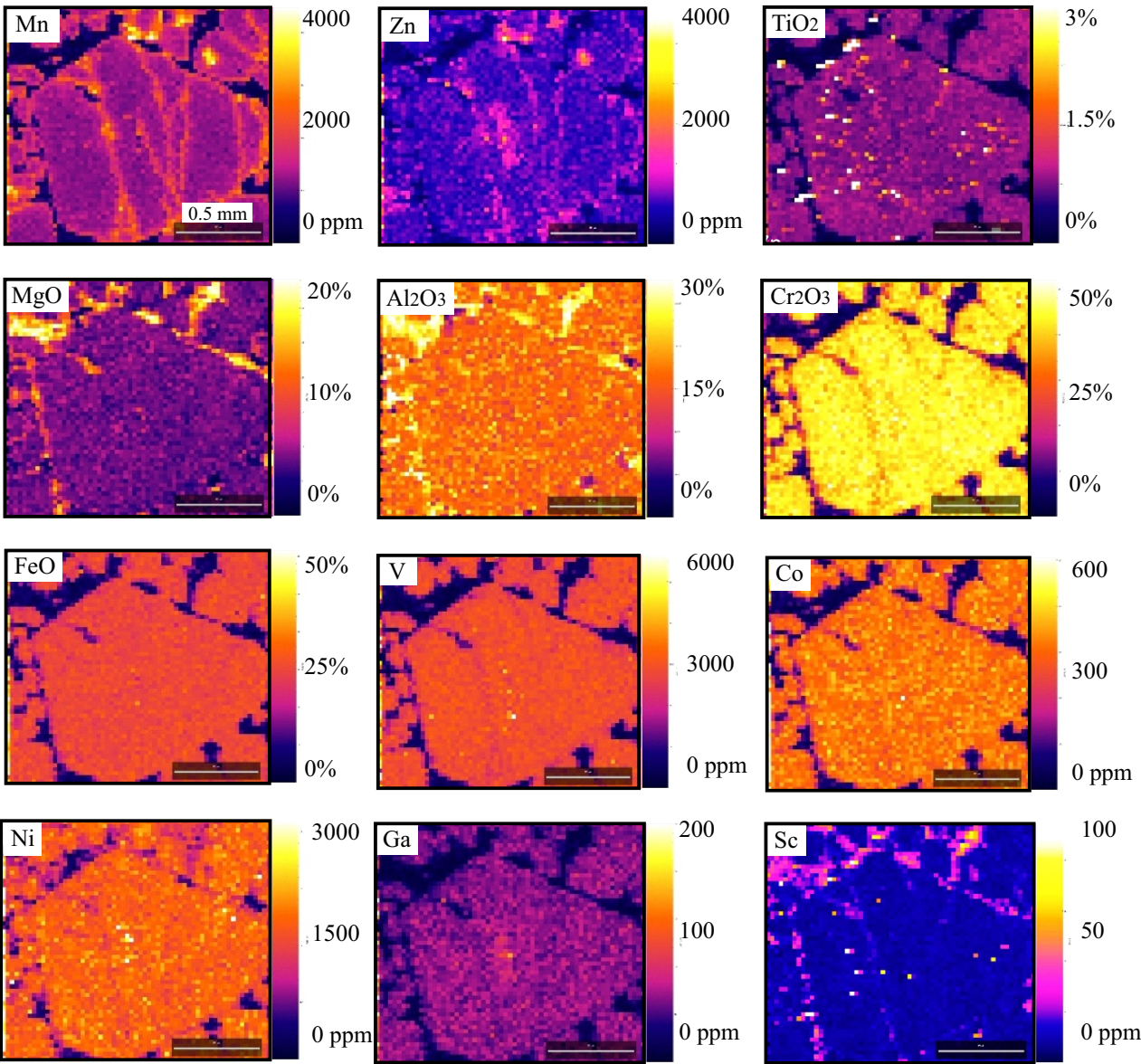


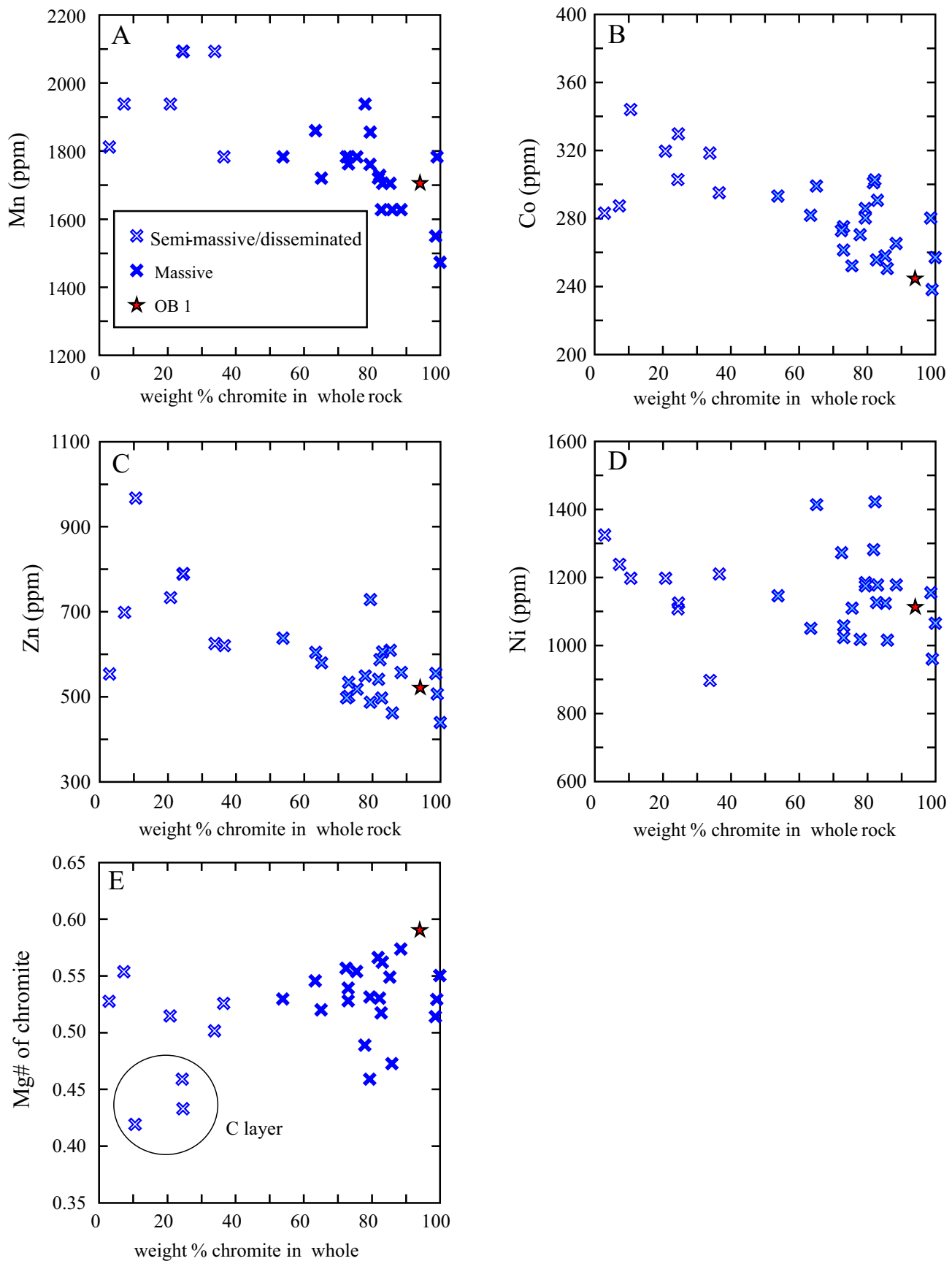


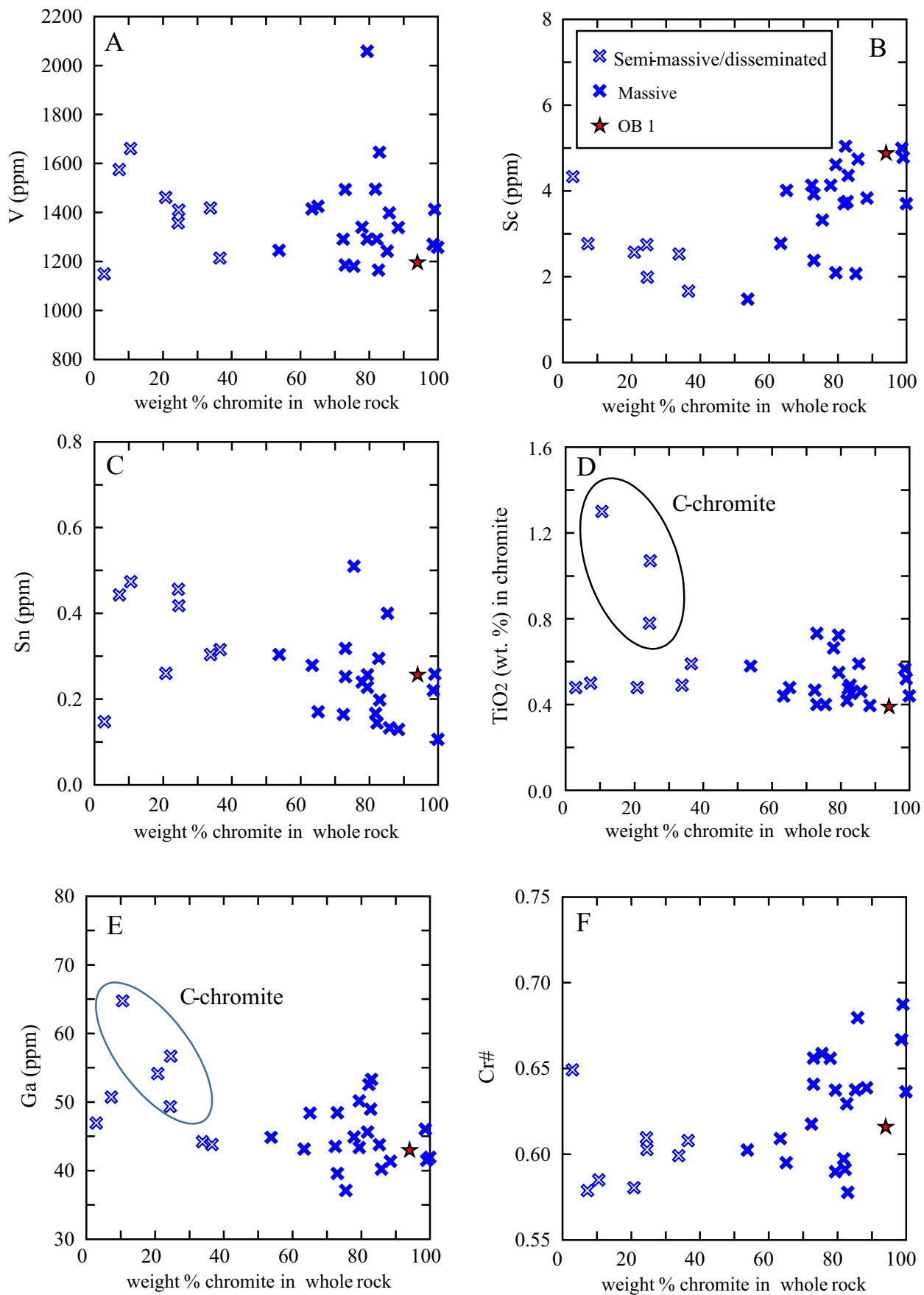


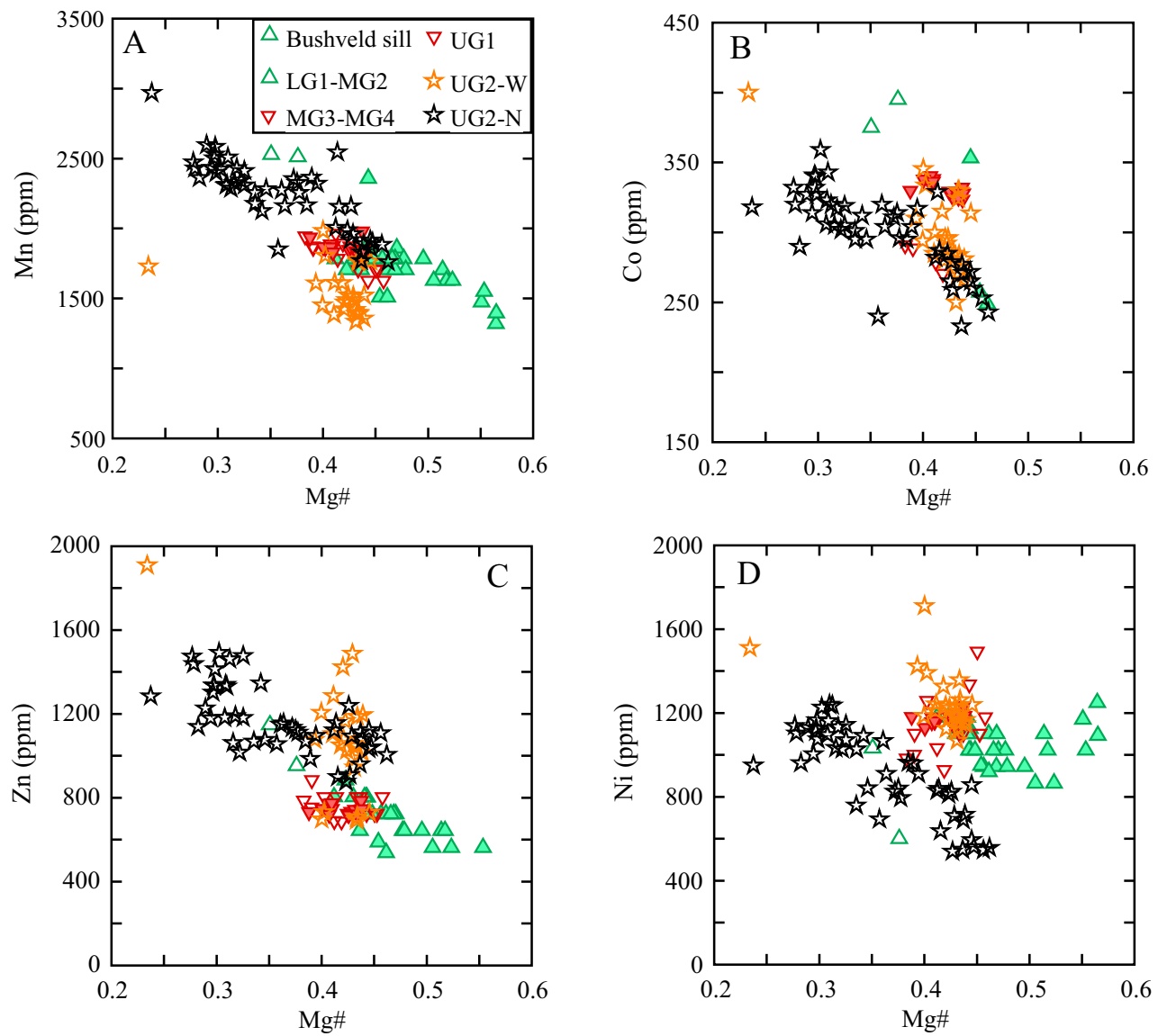


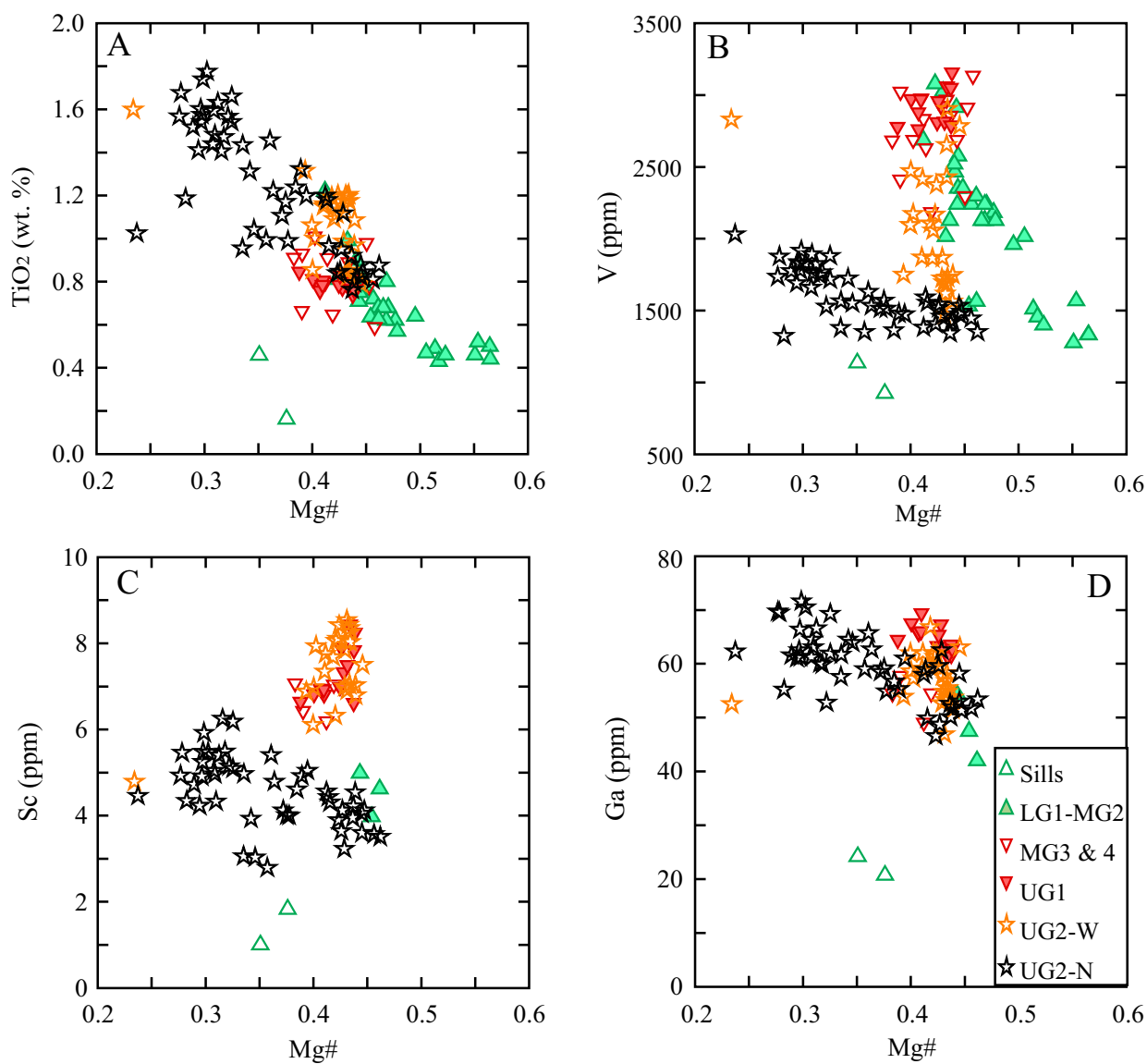


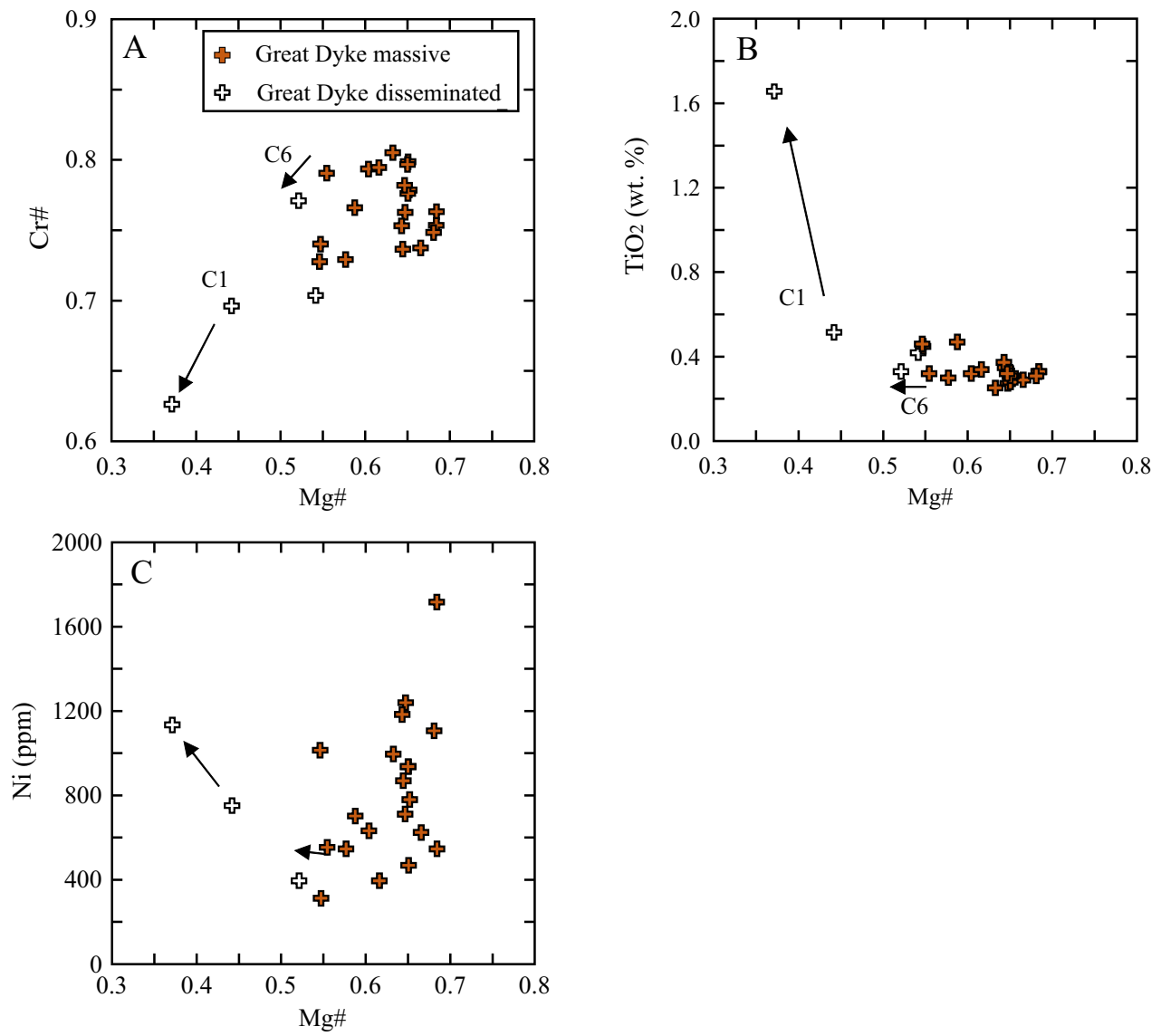


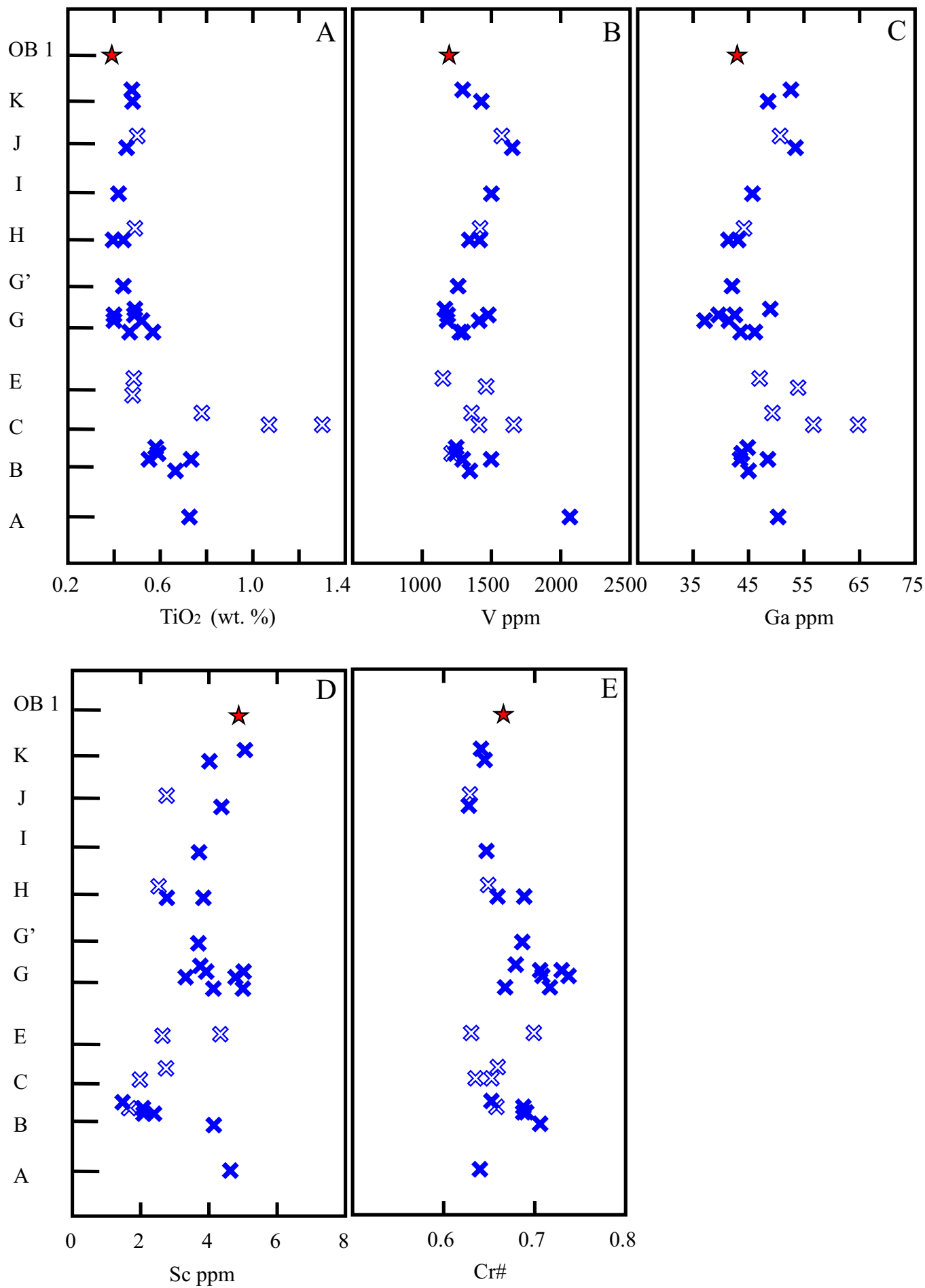


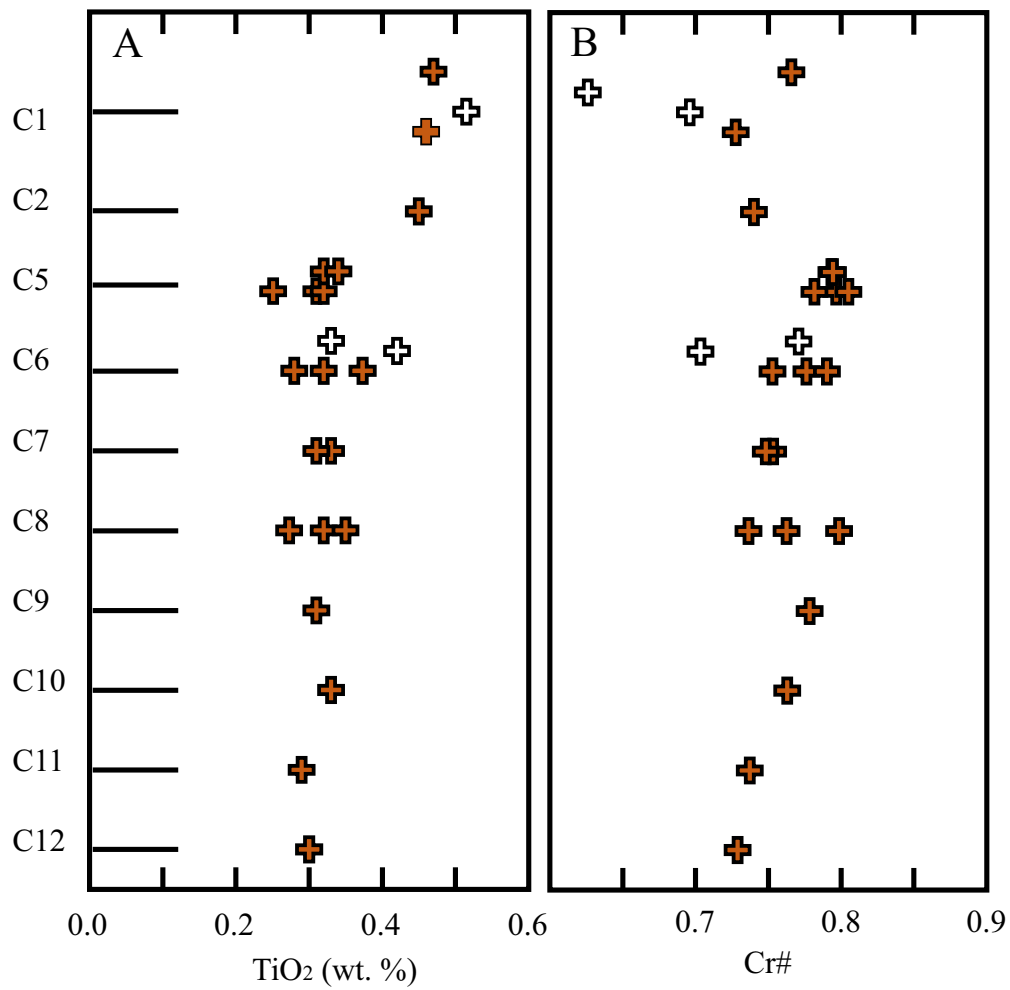


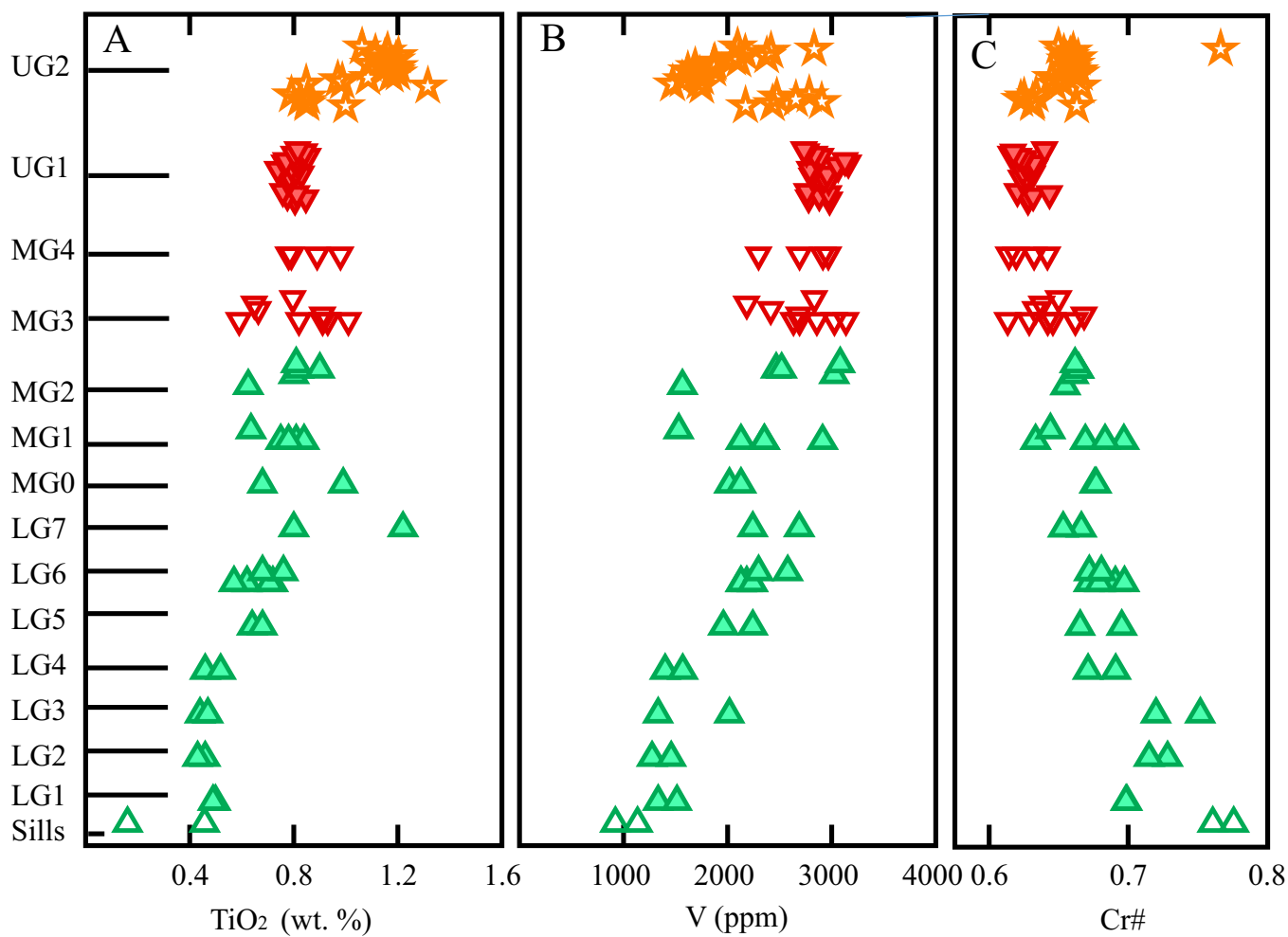


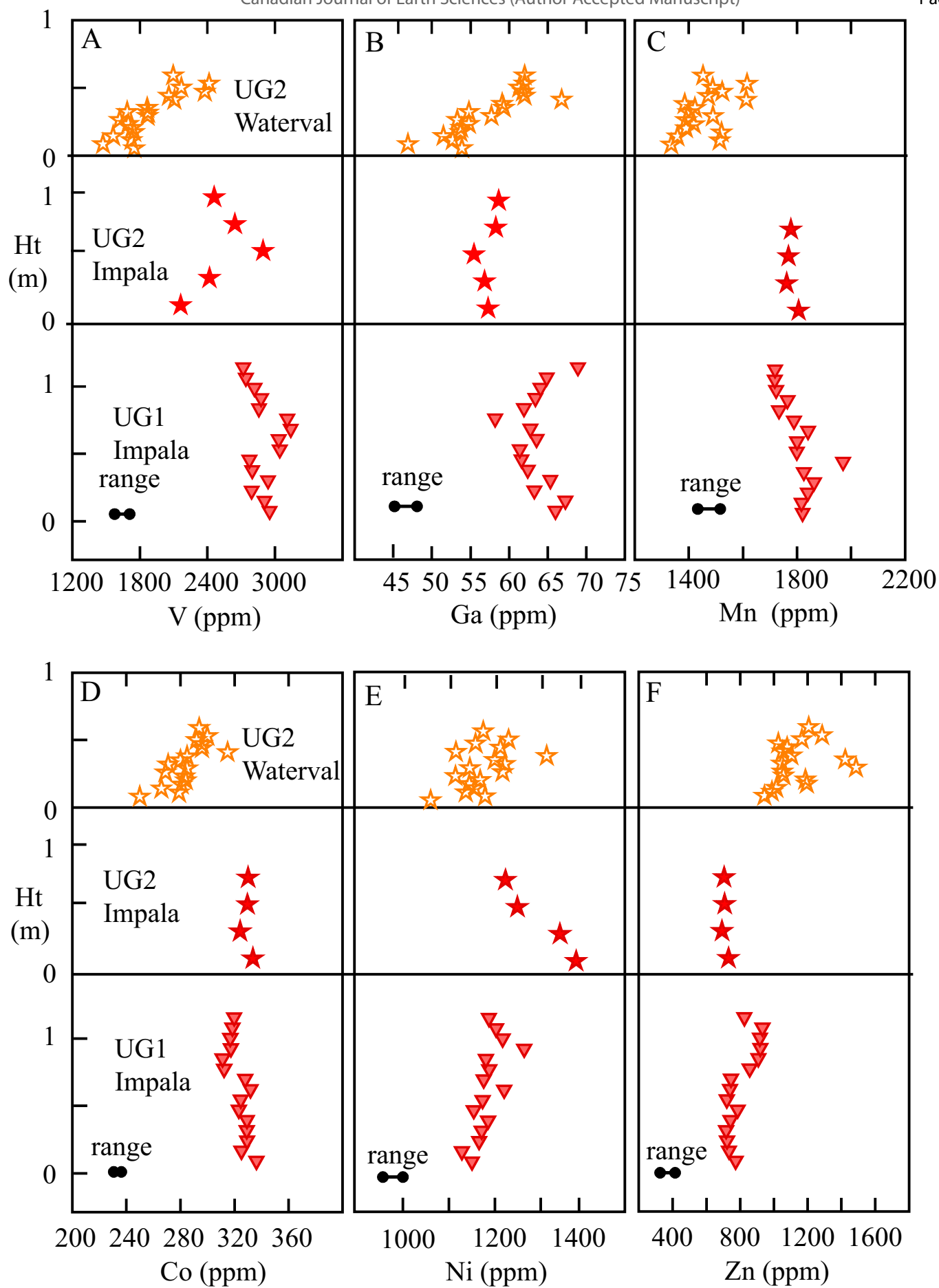


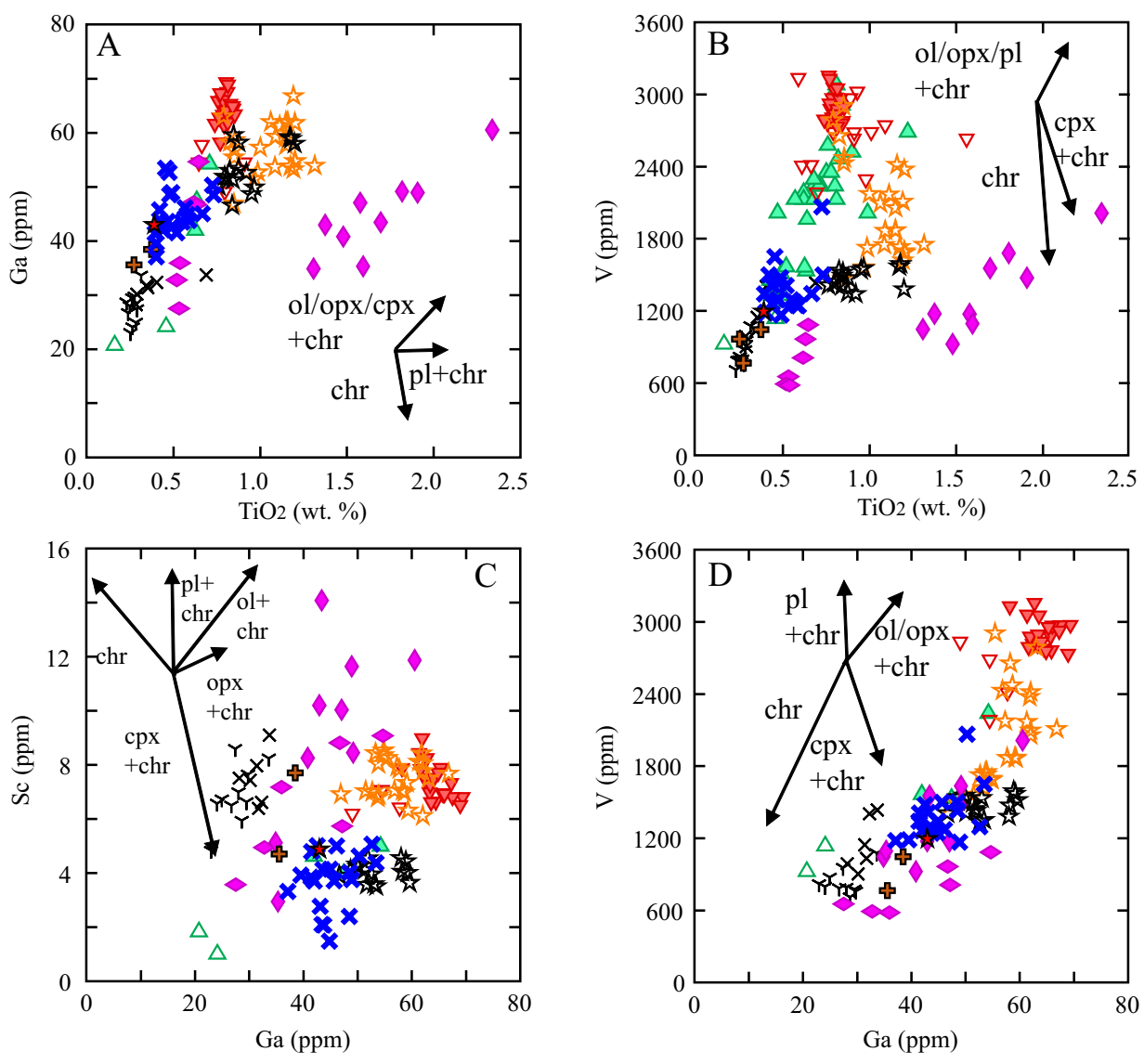


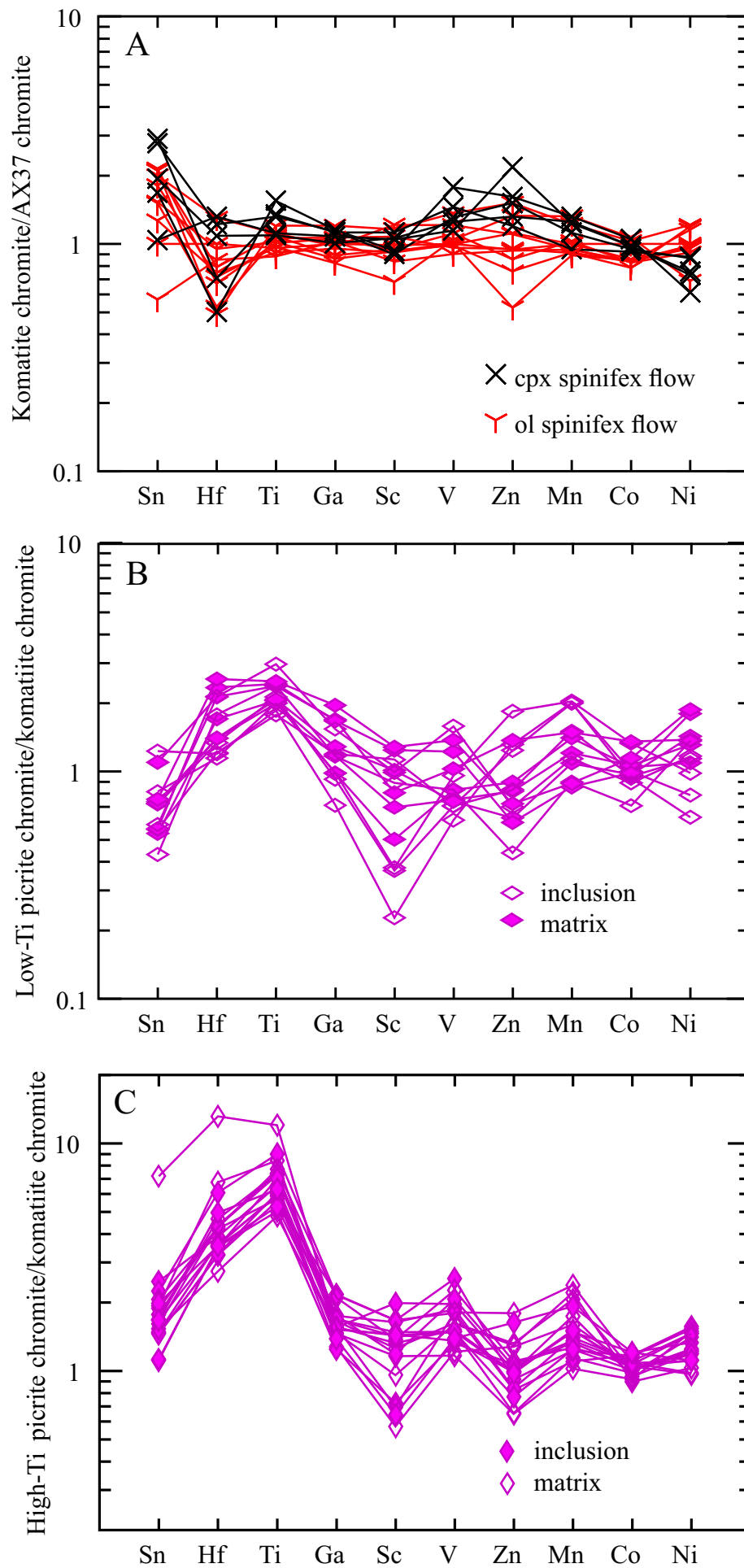


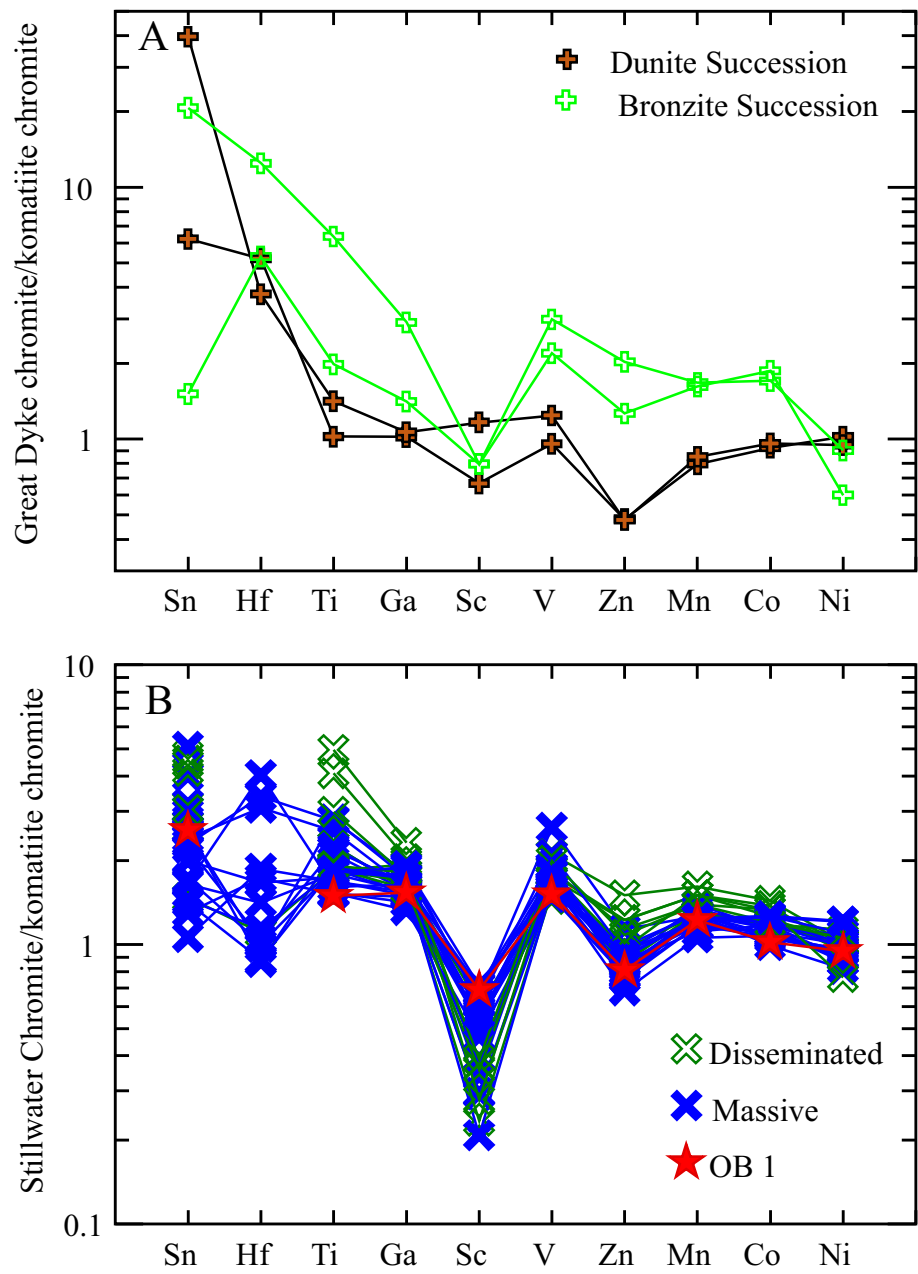


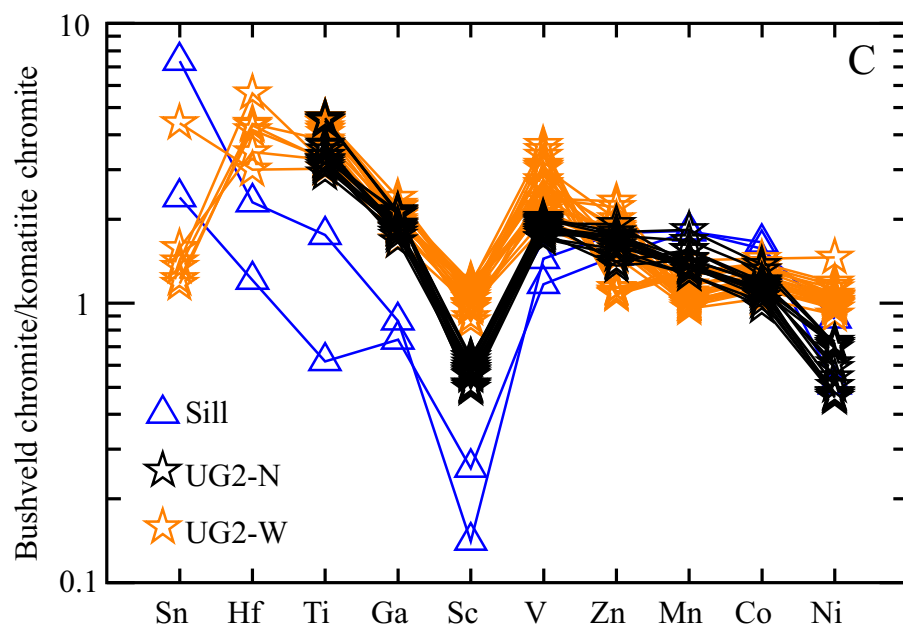
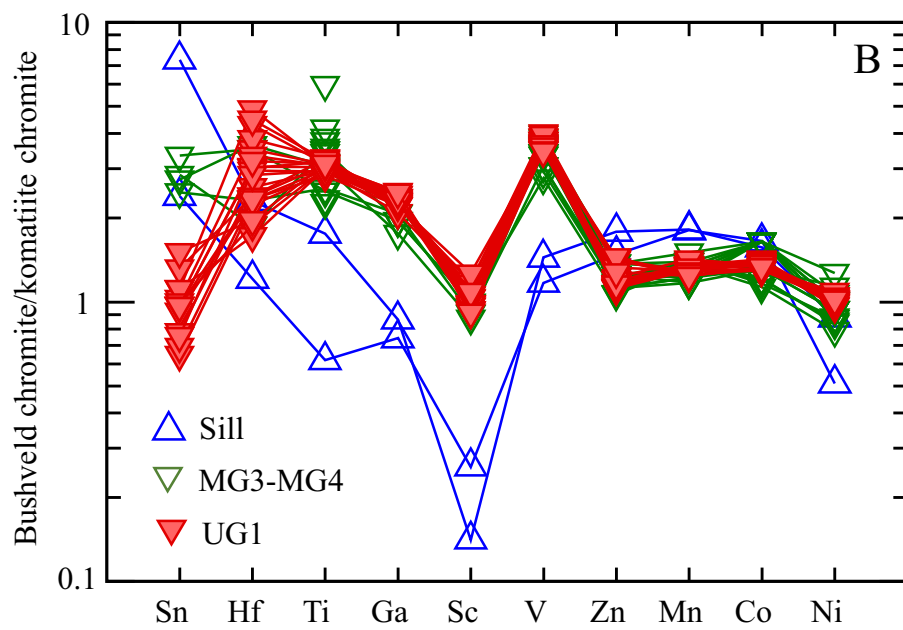
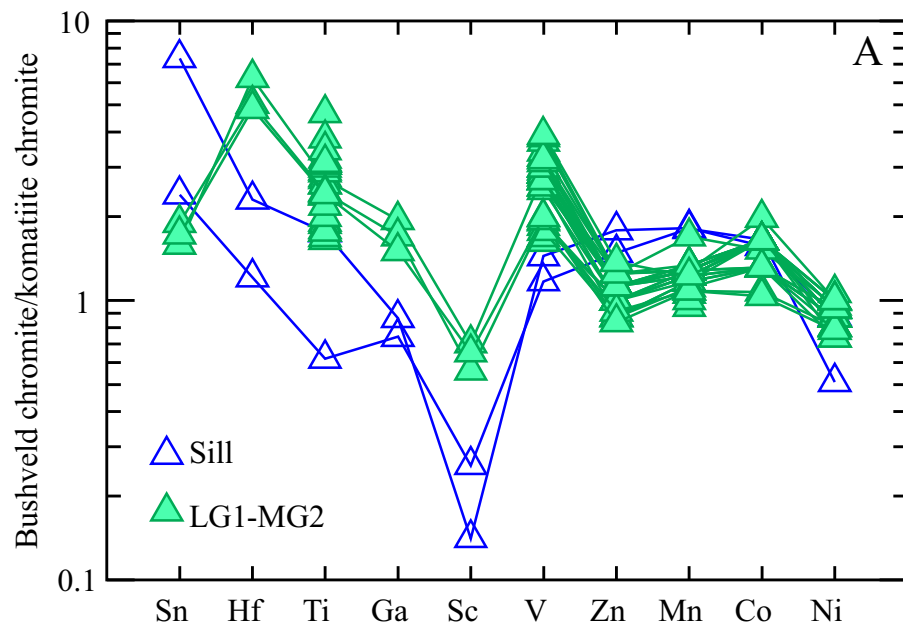












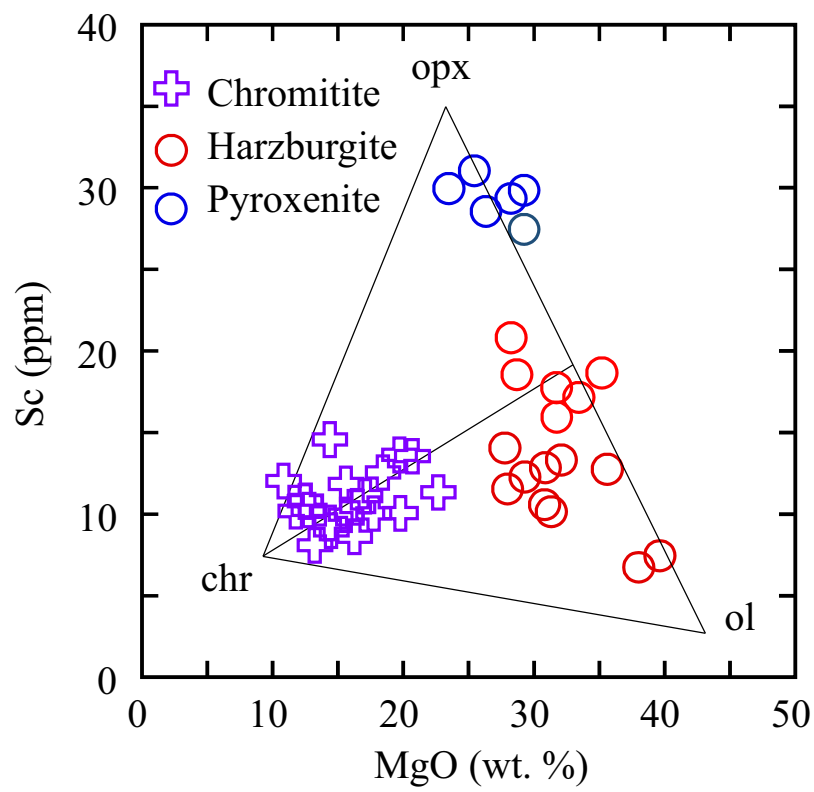


Table 1 Reference Materials used for Calibration During Laser Ablation and Results for Monitors

Isotope	Mg	Al	Si	P	Sr	Ti	V	Cr	Mn	Fe	Co	Ni	Cu	Zn	Ga	Ge	As	Y	Zr	Nb	Mo	Ru	Rh	Pd	Cd	In	Sb	Hf	Ta	W	Re	Os	Ir	Pt	Au	Bi
Isotope used	24	27	29	31	45	49	51	52	55	57	59	60	63	66	71	74	75	89	90	93	95	101	103	108	111	115	118	178	181	182	185	189	193	195	197	209
Reference material used for calibration	GSE-1g	GSE-1g	GSE-1g	GSE-1g	GSE-1g	GSE-1g	GSE-1g	GSE-1g	SE-1-Pb727	GSE-1g	GSE-1g	GSE-1g	GSE-1g	GSE-1g	GSE-1g	GSE-1g	GSE-1g	GSE-1g	GSE-1g	Pb-727	Pb-727	Pb-727	GSE-1g	GSE-1g	GSE-1g	GSE-1g	GSE-1g	GSE-1g	GSE-1g	GSE-1g	Pb-727	Pb-727	Pb-727	Pb-727	GSE-1g	
Concentration used ppm	21106	68004	259994	70	530	450	440	400	590	98700	380	440	380	440	490	320	200	410	410.036	420	390	36.5	41.4	43.4	160	370	280	395	390	430	120	46.7	48	35.5	45.4	320
Standard deviation	181	2117	701	20	20	42	20	80	20	610700	20	80	40	30	80	80	90	30	40	30	0.1	0.1	0.1	30	40	30	1	40	50	2.4	2.4	1.2	0.8	2.4	30	
Detection limits kHz	0.18	0.14	263.67	6.17	0.09	0.58	0.07	1.23	0.89	0.068	0.23	0.21	0.29	0.017	0.30	0.22	0.005	0.006	0.035	0.040	0.006	0.017	0.045	0.012	0.040	0.009	0.003	0.014	0.015	0.026	0.007	0.017	0.012	0.009		
Source of values Geochem for GSE-1g, continue for Pb-727																																				
Monitors																																				
AX-37	kositite chemist (in-house reference material)																																			
Working values	78384	71253	<1000		7.1	1539	790	36471	1359	136512	208	1176	6.6	608.0	27.7	0.457	<3	<0.012	0.649	<0.1	<0.04	0.303	0.014	<0.02	<0.1	0.018	0.105	0.020	<0.004	<0.002	nd	0.015	0.020	<0.02	<0.012	<0.01
Method	Probe	Probe	Probe	Laser	Laser	Laser	Laser	Probe	Laser	Probe	Laser	Laser	Laser	Laser	Laser	Laser	Laser	Laser	Laser	Laser	Laser	Laser	Laser	Laser	Laser	Laser	Laser	Laser	Laser	Laser	Laser	Laser	Laser	Laser	Laser	Laser
Standard deviation	n=62 laser	n=18 probe		0.5	93	60	2278	28	12388	7	134	1.2	59.0	3.5	0.090					Laser	Laser	Laser	Laser	Laser	Laser	Laser	Laser	Laser	Laser	Laser	Laser	Laser	Laser	Laser	Laser	
Method	nd by laser																																			
Run 1 Emeishan and Great Dyke	54186	60222	2153	<10	7.8	985	931	341596	1505	136512	242	1174	1.4	584.0	32.5	<0.3	<0.2	<0.005	nd	<0.01	0.040	0.445	0.006	<0.018	0.173	<0.012	0.154	0.060	0.066		0.018	<0.03	0.018	<0.017	0.014	<0.018
Standard deviation n=8	3631	2922	1126		0.6	122	74	16528	100	85	61	74	0.5	156.0	7.4					0.094	0.005	0.030				0.228	0.022	0.032		0.000	0.013		0.010			
Run 2 Stillwater and MG	77554	68245	1862	<10	6.5	1578	790	373737	1434	136900	238	1342	11.6	396.1	28.1	2.060	<0.2	0.026	nd	0.021	<0.04	0.315	0.023	<0.017	<0.05	0.016	0.179	0.022	<0.003	0.213	0.019	<0.03	0.012	<0.02	<0.02	0.018
Slates (n=5)	21511	10505	480		1.5	117	98	52026	5	85	19	225	4.7	11.4	2.1	0.090	0.030	0.000	0.000	0.080	0.012					0.064	0.000	0.000	0.149	0.000	0.000	0.004	0.000	0.000	0.004	
Run 3 1/2 UG1	58681	56857	812	17	5.9	1303	712	319151	1312	136900	202	1124	6.4	401.1	28.6	0.771	0.518	0.006	nd	0.171	<0.04	0.218	0.010	<0.017	<0.05	0.017	0.057	0.017	<0.003	0.009	nd	<0.03	0.009	<0.017	<0.012	<0.01
Slates (n=5)	11138	6377	339		0.6	126	55	30155	57	85	7	239	1.0	101.3	2.1	0.278	0.006	0.008	0.016	0.019	0.006					0.003	0.015	0.016								
Run 4 UG2 and 1/2 UG1	62621	59724	1102	18	7.0	1424	708	355878	1415	136900	226	1145	9.6	363.3	26.2	0.425	<0.0	<0.005	0.360	0.137	<0.04	nd	nd	nd	<0.05	<0.01	<0.05	0.014	<0.003	<0.014	<0.015	nd	nd	nd	nd	nd
Slates (n=5)	9557	6126	386		0.6	119	60	27252	34	85	9	156	0.5	5.7	1.9	0.196			0.030	0.019						0.008										
Run 0 Komatiites	71278	66900	2250	<10	6.51	1443	784	325189	1377	136900	206	1130	7.37	718	26.7	0.477	<2	<0.014	0.608	nd	<0.4	0.336	0.016	<0.03	nd	0.022	0.127	0.015	<0.006	nd	nd	0.019	0.019	<0.17	nd	nd
Slates (n=3)	10763	5724			1	186	106	24505	62	85	10	185	2	70	1.4	0.101			0.191			0.020	0.004			0.007	0.043	0.005	0.003		0.009	0.007				
Geph-6 basalalt glass working values (AG)	51318	92145	224259	611	36.8	7012	238	300	1255	72600	47	146	89.5	70.8	16.0	1.260	2.300	19.330		4.160					0.170	0.050	1.330	1.520	0.280	0.400					0.066	
Slates	4955	12538	3418	131	2.6	1192	27	22	93	85	4	19	20.3	16.6	2.0	0.410	1.780	0.410		0.018	0.005	0.013				0.710	0.155	0.030								
Run 1	49730	89100	223460	940	40.5	7017	260	329	1291	72600	48	157	87.0	80.1	14.7	2.000	2.000	18.420	nd	3.835	0.793	0.223	<0.006	<0.02	0.065	0.055	1.162	1.414	0.239	0.278	nd	nd	0.046	0.499	0.145	0.012
Slates (n=9)	551	1200	1209	35	0.9	96	3	1	12	85	0	3	3.5	10.3	0.2	0.153	0.173	0.414		0.018	0.005	0.013				0.012	0.002	0.107	0.015	0.005	0.020	0.014	0.102	0.024	0.002	
Run 3	49480	86877	216961	1297	38.2	6911	251	326	1274	72600	48	152	84.0	72.0	13.8	1.232	2.470	17.840		2.631	0.410	0.207	<0.006	<0.02	0.085	0.051	0.955	1.393	0.219	0.230	nd	<0.03	0.034	0.380	0.114	0.013
Slates (n=5)	2335	4521	1777	93	0.7	47	3	35	11	85	0	1	1.0	1.1	0.2	0.074	0.478	0.449		0.083	0.011	0.025	0.002	0.007	0.019	0.007	0.007	0.041	0.011	0.026			0.007	0.073	0.020	0.003
Run 4	49023	89516	228548		38.8	6840	264	345	1260	72600	50	156	88.5	78.8	15.2	1.255	<2	18.018	52.390	3.857	0.389					0.088	0.053	1.062	1.393	0.231	0.275	<0.015				
Slates (n=4)	389	1402	1832	13	1.0	88	4	4	3	85	0	3	0.2	1.8	0.2	0.106		0.578	2.257	0.029	0.014				0.007	0.003	0.050	0.063	0.011	0.012						

Mason Aung, et al., 1996. The petrology and geochemistry of the lower granulite succession of the Great Dyke in the Matigaharan area, Unpublished MSc. Rhodes University.

Nelson, R.F., LeFavre, D.J., 2018. In situ U–Pb zircon (UHS) and medium (SHRIMP) ion beam analysis from the Kapuskasing thrust zone, east of Lake Huron, Ontario: An audit diagnostic pour l'interprétation des données géologiques. In: Sc.: Université du Québec à Chicoutimi.

Hudson, A.L., Kincaid, J., Wilson (2002). A., Hudobubsky, M., McQuade, S., Chumet, G., and Stanley, C. (2000). Chromium composition and PGE content of baritized chromites: Part 1—the Lower and Middle Groups, Applied Earth Sciences Transactions of the Institutions of Mining and Metallurgy: Section B 118(3-4): 123–165.

Nelson, A.W., 1982. The geology of the Great Dyke, Zimbabwe: the ultramafic rocks. Journal of Tectonic Geology 2:240–262.